Virtual Histology with Photoacoustic Remote Sensing

by

Saad Rasheed Abbasi

A thesis
presented to the University of Waterloo
in fulfillment of the
thesis requirement for the degree of
Master of Applied Science
in
Systems Design Engineering

Waterloo, Ontario, Canada, 2020

Author's Decleration

This thesis consists of material all of which I either authored or co-authored: see included Statement of Contributions. This is a true copy of the thesis, pending revisions from readers.

I understand that my thesis may be made electronically available to the public.

Statement of Contributions

Saad R. Abbasi was the sole author for Chapter 1,2 and 7. These chapters were authored under the supervision of Dr. Parsin Haji Reza and are not intended for publication. Chapters 3, 5 and 6 of this thesis consist of previously published co-authored manuscripts. Chapter 4 is composed of a co-authored manuscript that has been submitted for publication.

Chapter	Citation	Author's Contributions
3	**Abbasi, Saad**, Kevan Bell, and Parsin Haji Reza. "Rapid High-Resolution Mosaic Acquisition for Photoacoustic Remote Sensing." Sensors 20, no. 4 (2020): 1027.	Drafted the manuscript, developed the software for mosaic acquisition and reconstruction, conducted experiments and revised text based on edits by co-authors.
4	Submitted to Quantitative Imaging in Medicine and Surgery Coauthors: Kevan Bell, Benjamin Ecclestone and Parsin Haji Reza	Assisted in the optical setup, developed the software for real time and 3D imaging, conducted experiments and drafted the manuscript.
5	**Abbasi, Saad**, Martin Le, Bazil Sonier, Deepak Dinakaran, Gilbert Bigras, Kevan Bell, John R. Mackey, and Parsin Haji Reza. "All-optical Reflection-mode Microscopic Histology of Unstained Human Tissues." Scientific reports 9, no. 1 (2019): 1-11.	Developed the software for acquisition, reconstruction and the mechanical stages, performed data analysis, carried out experiments and contributed to the manuscript
6	**Abbasi, Saad**, Martin Le, Bazil Sonier, Kevan Bell, Deepak Dinakaran, Gilbert Bigras, John R. Mackey, and Parsin Haji Reza. "Chromophore selective multi-wavelength photoacoustic remote sensing of unstained human tissues." Biomedical Optics Express 10, no. 11 (2019): 5461-5469.	Assisted in the optical setup, developed the software for image acquisition and reconstruction, conducted experiments and contributed to the manuscript.

Abstract

Histopathology plays a central role in cancer screening, surgical margin analysis, cancer classification, and understanding disease progression. The vast majority of biopsies or surgical excisions are examined via transmission-mode bright-field microscopy. However, bright-field microscopy requires thin stained tissue samples as it is unable to visualize contrast on thick tissues. Consequently, biopsies and surgically excised specimens undergo extensive tissue processing to prepare histology slides. This tissue processing can take up to two weeks for complex cases before a diagnosis can be presented, potentially resulting in poorer patient outcomes. Surgical margins are commonly analyzed intraoperatively using frozen sectional analysis. While this technique has improved patient outcomes, the quality of frozen sections is often lower than post-operative histologic analysis. This lower quality leads to significant variability in diagnosis. Ultimately, both frozen section analysis and standard histologic analysis are limiting because of the need to process tissues to cater to bright-field microscopy. It would be desirable to forego creating thin tissue sections and instead visualize tissue morphology directly on biopsies and surgical specimens or even directly on the patient's body (*in-situ*).

Photoacoustic remote sensing (PARS™) is an emerging non-contact imaging technique. PARS microscopy is an all-optical photoacoustic imaging modality that takes advantage of endogenous optical absorption present within tissues to provide contrast to enable non-contact label-free imaging. PARS has demonstrated excellent resolution and contrast in various applications, such as *in-vivo* imaging, functional imaging, and deep imaging, while operating in a reflection-mode architecture. This non-contact label-free reflection-mode design lends itself well to imaging unprocessed tissue specimens or *in-situ* morphological assessment.

Using PARS microscopy, this thesis takes preliminary steps towards an *in-situ* surgical microscope. These steps take the form of developing a PARS system that can recover contrast from DNA and visualize the resulting nuclear morphology in real-time and on arbitrarily sized specimens. Later, this system was expanded to image additional contrasts from hemoglobin to approach the diagnostic information provided by standard histopathology. This research imaged a variety of human tissue types, including breast, gastrointestinal, and skin. These specimens were in the form of thin unstained slides and thick tissue blocks. The tissue blocks serve as an analog to visualization of contrast fresh tissues and *in-situ* imaging. Adjacent sections of each tissue type were prepared using standard histopathology and compared against the PARS images for experimental validation. These results represent the first reports of imaging human tissues with a non-contact label-free

reflection-mode modality. The author believes this research takes vital steps towards an imaging technique that may one day reveal cancer *in-situ*.

Acknowledgements

I want to begin by expressing my sincere gratitude to my graduate supervisor, Professor Parsin Haji Reza, for his endless support, guidance, mentorship, encouragement, and always pushing me to do better. His mentorship has lead me to be a better scientist and engineer. His guidance and patience in reading my manuscripts made me a better writer. And his encouragement led me to overcome my fears and become a better presenter. This research would not have been possible without his enthusiasm, insights, and suggestions.

This research relied upon several clinicians in Alberta who were a source of continued support. I want to thank Professor John Mackey for his continued encouragement, mentorship, endless enthusiasm for our work, clinical insight, and for leading the ethics review in Edmonton, without which imaging human tissue specimens would not have been possible. This research would not be of the same caliber without his contributions. Additionally, I would like to express my sincere gratitude to Professor Gilbert Bigras for his infinite patience in answering my questions about histology and for undertaking the enormous effort of preparing tissue samples of every variety studied in this thesis. I would also like to thank Dr. Deepak Dinakaran for his help in procuring samples, providing clinical insight, and continued encouragement.

I want to thank my thesis readers, Professor Paul Fieguth and Professor Kostadinka Bizheva, for their careful reading of the manuscript, feedback, and suggestions.

I want to thank my friends and colleagues at PhotoMedicine Labs. In particular, a big thank you to my colleague Dr. Kevan Bell for his mentorship, patience in answering my technical questions throughout my program, allowing me to collaborate with him on many exciting projects and discussions around PARS and many other topics! Also, I am thankful to Benjamin Ecclestone for helping me with experiments and continued encouragement. I want to thank Martin Le for leading the ethics review at the University of Waterloo and helping me with experiments. Last, but certainly not least, I would also like to thank Dr. Shahid Haider for his helpful comments on this manuscript.

Dedication

This work is dedicated to my father.

Table of Contents

List of Figures

List of Tables

List of Abbreviations

ANSI American National Standards Institute

FD-OCT fourier-domain OCT

FFPE formalin-fixed paraffin-embedded

FWHM full width at half maximum

H&E hematoxylin and eosin

LSM light-sheet microscopy

MEMS microelectromechanical systems

MPE maximum exposure limit

MUSE microscopy with ultraviolet surface excitation

NA numerical-aperture

OCT optical coherence tomography

OR-PAM optical-resolution photoacoustic microscopy

PARS photoacoustic remote sensing

SD-OCT spectral-domain OCT

SNR signal to noise ratio

SRS stimulated Raman spectroscopy

SS-OCT swept-source OCT

TD-OCT time-domain OCT

UV-PAM ultraviolet photoacoustic microscopy

List of Symbols

$\mathbf{C_A}$ correction factor for maximum exposure calculations

$\langle \rangle$ Mean

$\mathbf{R}$ reflectivity

$\Delta R_{DNA,\lambda}$ Reflectivity change for DNA

$\Delta R_{RBC,\lambda}$ Reflectivity change for red blood cell (RBC)

$\mathbf{n}$ refractive index

$\mathbf{s}$ image signal intensity

λ Wavelength of Light

Chapter 1

Introduction

1.1 Motivation

A 2019 study by the Canadian Cancer Society reported that nearly half of Canadians are expected to be diagnosed with cancer in their lifetime [1]. Despite improvements in cancer screening and treatment, cancer remains the leading cause of mortality in Canada, accounting for nearly 30% of all deaths [1, 2]. Cancer represents a diverse group of diseases with a variety of causes and treatments, but all of which exhibit abnormal cell growth. Being a disease that directly affects cells, it is no surprise microscopic assessment of tissue plays a central role in cancer patient management and care. Tissue resected from biopsies is microscopically assessed to determine the initial diagnosis, cancer classification, disease progression, and even the fundamental biology of the disease, all of which are necessary to formulate a complete treatment plan. Surgery is the preferred treatment method for many solid cancers due to its longstanding history for providing the best patient outcomes. The primary goal of cancer resection surgery is to remove all cancerous cells from the body along with a minimal margin of healthy tissue. Following cancer surgery, patients with positive surgical margins have an increased risk of disease recurrence and are routinely required to undergo follow-up surgery or adjuvant treatment [3, 4, 5, 6]. The gold standard for margin analysis remains post-operative histopathological analysis. This method examines resected tissue at a cellular scale to ensure that no cancerous cells are near the edge of the tissue.

While histopathology remains the benchmark for microscopic assessment of tissue, the preparation of histology slides is a laborious, time consuming, and resource-intensive process. The purpose of the histopathological workflow is to process freshly excised tissue specimens into thin stained sections that can be examined with a conventional light mi-

croscope. An extensive background on the histopathology workflow is provided in section 2.1. The laborious nature of histopathology can potentially lead to prolonged turnaround time for large and complex cases. For example, for radical cancer resections, about 10% of the cases take longer than ten days to diagnose [7]. Frozen sectioning is a commonly used method to assess surgical margins rapidly in an intraoperative setting. However, the process requires rapid freezing of the tissue, which can potentially introduce artifacts into the tissue architecture, deteriorating the cellular morphology. The inferior quality of the frozen sections can lead to challenging interpretation of the sample and makes diagnosis challenging [8]. Ultimately, both frozen section analysis and standard histopathology are limited because they need to process tissue into thin stained sections for bright-field microscopy. Thus, it would be desirable to move away from transmission-mode bright-field microscopy towards a reflection-mode method. A reflection-mode method could forego the extensive tissue processing and visualize contrast on unprocessed tissue specimens or directly on the patient's body (i.e. *in-situ* imaging). Such a method would result in a dramatic speed-up of the morphological assessment of excised tissues and potentially lead to improved patient outcomes.

Photoacoustic remote sensing (PARS)™ is an emerging non-contact label-free biomedical imaging modality [9, 10, 11, 12]. PARS has demonstrated excellent contrast and sub-micron resolution in imaging mouse-ear microvasculature structures *in-vivo* while operating in a reflection-mode architecture. PARS is a uniquely promising solution for fresh tissue and *in-situ* imaging due to its non-contact label-free reflection-mode architecture.

1.2 Thesis Objectives and Contributions

The objective of this thesis was to develop a PARS microscope that enables microscopic assessment of thin and thick tissue specimens. This objective serves as a preliminary step towards a surgical microscope that may one day visualize cancer margins *in-situ*. The thick tissue acts as an analog to fresh tissue or *in-situ* imaging and serves to validate the efficacy of label-free reflection-mode contrast with PARS. This thesis makes four distinct contributions towards the development of this overarching goal:

- An image acquisition method for rapid gross assessment of tissue specimens.

- A high-resolution real-time and 3D imaging system to provide live feedback to clinicians. This approach demonstrated a resolution of 1.2 µm, the highest reported with a real-time photoacoustic imaging system, and reported the first 3D results with PARS.

- A PARS microscope to image unstained nuclear morphology in a variety of thin and thick human tissue specimens. These results represented the first non-contact label-free reflection-mode images of human cellular morphology.

- A novel multi-wavelength chromophore selective PARS microscope to incorporate hemoglobin contrast in addition to nucleic contrast.

1.3   Organization of Thesis

This thesis is organized as follows:

- **Chapter 2** presents a background of PARS and a literature review of related methods that aim to address the limitations of histopathology.

- **Chapter 3** discusses the development of data acquisition methods to acquire wide field of views with high spatial sampling via mosaics. Image reconstruction methods are also discussed. The method is demonstrated with large mosaics of carbon fiber networks and unstained human breast images.

- **Chapter 4** discusses a live feedback system for PARS, including the development of a simple image interpolation technique for real-time image reconstruction. By employing optical sectioning, we also demonstrate the first 3D imaging results with a non-contact reflection-mode label-free imaging modality. The method's effectiveness is demonstrated with carbon fiber networks and *in-vivo* imaging of a mouse ear's microvasculature structure.

- **Chapter 5** investigates a PARS system for imaging the nuclear morphology in thin and thick tissue specimens. Multiple types of samples are imaged and compared with images from a conventional light microscope. Types of tissues investigated include human breast, gastrointestinal, and skin.

- **Chapter 6** extends PARS for selective chromophore imaging. In addition to accentuating the nuclear morphology, this study highlights hemoglobin contrast in human breast and tonsil tissue.

- **Chapter 7** discusses future work to extend PARS and concludes this thesis.

Chapter 2

Background and Literature Review

In recent decades, a variety of techniques have aimed to address the limitations of standard histopathology. In this chapter, we begin by discussing standard histopathology and provide an overview of how biopsies or surgical specimens are processed into thin tissue slices. This discussion is followed by a literature review of five techniques that have made significant contributions to virtual histopathology. We discuss the contrast mechanism, architectures, recent results, and the limitations for histology-like imaging for each method. We conclude this chapter by providing a background on PARS, including a discussion on how it addresses the limitations of previous approaches.

2.1 Histopathology

The vast majority of histopathological analysis is performed using conventional bright-field microscopes. Bright-field microscopes illuminate tissue specimens from underneath such that the light is transmitted through the sample. This type of illumination is known as transmission-mode and requires the specimens to be sufficiently thin such that light passes through the sample [13]. Bright-field illumination provides contrast through the absorption of transmitted light in dense tissue regions. However, most biological tissue is only weakly absorbing and does not provide sufficient contrast with just bright-field illumination [14]. This limitation of thin tissue sections and weak contrast is catered for by the standard histopathological process by processing thick excised surgical specimens into thin stained sections.

Preparing histology slides is a laborious multi-step process [15, 16]. Figure 2.1 illustrates the major steps in the workflow with the intermediate products. The process begins
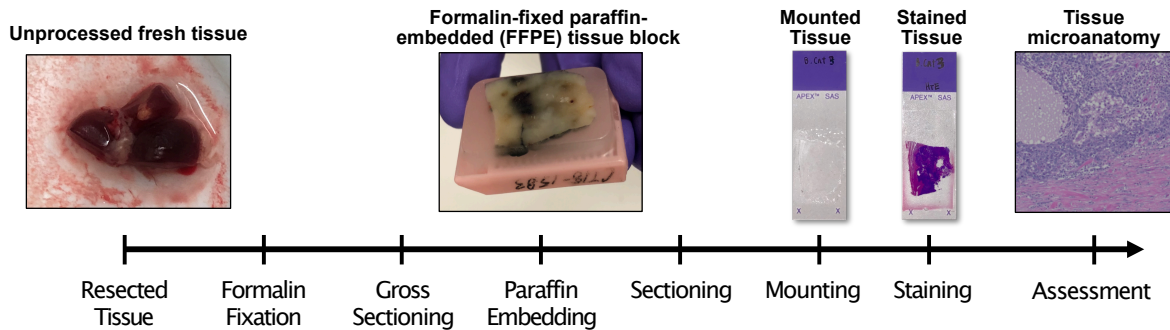
Figure 2.1: Standard histopathological workflow of processing fresh tissue into thin stained sections.

with fixing resected tissue in formalin (typically for 24 hours) to avoid putrefaction. Following fixation, selected areas of the specimen are dissected for examination to limit the amount of tissue processing. Since raw tissue is soft and compressible and therefore not suitable for sectioning directly, one of the major steps of this process is to transform tissues into hard incompressible rectangular specimens that can be sectioned easily.

To this end, the formalin-fixed specimens are embedded in hot paraffin wax to form rectangular formalin-fixed paraffin-embedded (FFPE) tissue blocks. These FFPE tissue blocks are then sectioned into thin ribbons (usually around 4-8 µm in thickness) and mounted onto glass microscope slides. As most cells are transparent and exhibit little contrast with bright-field illumination, the mounted tissue sections are stained with chromogenic dyes such as hematoxylin and eosin (H&E) before being protected by a coverslip. The staining protocol, in and of itself, is a multi-step process and depends on dyes being employed. Since staining is a chemical process, it is potentially susceptible to variability due to cross-contamination between dyes, changes in pH level due to prolonged storage, and the staining time. This variability manifests itself as a difference in contrast in prepared histology samples [17].

The exhaustive nature of the tissue processing workflow potentially leads to clinical practices that may not be ideal. For example, in the case of biopsies, any delay in morphological assessment would delay the initial diagnosis and the formulation of a treatment plan. Similarly, post-operative surgical margin analysis frequently requires patients to return for a second surgery or adjuvant treatment, resulting in significant stress on the patient and the healthcare system [18]. Additionally, the standard histopathological workflow limits the amount of resected tissue that can be assessed. Typically, tissues from biopsies or surgeries are sampled by a pathologist and then processed. However, these small samples may not be fully representative of the disease and may result in a diagnosis that does not entirely describe the disease. Several imaging techniques have attempted to address these

limitations, for example, microscopy with ultraviolet surface excitation [19, 20], light-sheet microscopy [21, 22], stimulated Raman spectroscopy [23, 24], and ultraviolet photoacoustic microscopy [25, 26, 27]. We discuss these methods next.

2.2   Microscopy with ultraviolet surface excitation

Microscopy with ultraviolet surface excitation (MUSE) is a recently introduced imaging modality for histology-like imaging [19, 20]. In conjunction with diffused ultraviolet (typically shorter than 300 nm) light, MUSE employs specific fluorescence dyes to elicit bright light emission from the tissue morphology. The fluorescence dyes tend to have similar specificity as the conventional H&E staining leading to images that resemble conventional histopathology.

MUSE has demonstrated histology-like imaging in fresh and fixed tissues [19, 20]. However, the requirement of fluorescence dyes can be undesirable for a variety of reasons. For example, the staining process can be variable, which may lead to inconsistency in contrasts between tissues. Additionally, to apply fluorescence stains, FFPE tissue blocks must be deparaffinized before imaging. Finally, some of the fluorescence dyes used by MUSE, such as Propidium Iodine and Hoechst, can be toxic, mutagenic, or carcinogenic, which makes them impractical intraoperatively and infeasible *in-situ* [20].

2.3   Light-sheet microscopy

Light-sheet microscopy (LSM) relies on producing a sheet of light that illuminates a single plane within an optically transparent sample [28, 29, 30, 31]. The tissue sample is stained with fluorescence dyes, and the emitted fluorescence is collected with an objective lens placed perpendicular to the light sheet. The objective lens serves to focus the fluorescence light onto a camera. The sample can then be moved within the light sheet to selectively illuminate different sections. Alternatively, the light sheet and the focal plane of the detection objective can be moved synchronously. In effect, the method acts as an optical microtome as it selectively sections planes within the specimen during the scan. This technique has been applied for imaging single molecules, living cells, and entire organs [32, 33, 34].

The first report of histology-like imaging with LSM came in 2017, where an open-top design was demonstrated to scan arbitrarily sized specimens [21]. The key advantage of

this design is that it makes optical clearing an optional step if only surface imaging is to be performed. The study investigated imaging of fixed and fresh human tissue specimens and compared them to standard histopathology. This system employed two fluoresce stains to emulate H&E-like contrast. However, one of the stains employed bonded poorly to fresh tissue and slowly leaked during imaging, resulting in inconsistent contrast. Later, this limitation was improved upon by employing more strongly binding stains in conjunction with dual-wavelength illumination [22].

LSM has demonstrated excellent resolution and contrast for histology-like imaging with relatively good agreement with H&E stained histology. Despite the advantages in the rate of imaging, optical sectioning, and 3D imaging capabilities, LSM faces several challenges [35]. As the light sheet transverses the specimen, it is partially scattered, producing a cloud of diffused light around the target [35]. This diffused light tends to blur the image. Similarly, if the light sheet is positioned deep within the tissue, the emitted fluorescence is more likely to be scattered, lowering the contrast and resolution [35]. Since LSM employs orthogonal illumination, any optically absorbing structures prevent the excitation of fluorophores behind the structure. This effect appears as attenuated stripes or shadows in the final image, lowering the image quality [36].

Finally, this method faces similar challenges for intraoperative applications as MUSE or other fluorescence-based techniques. The fluorescence stains can potentially be toxic and may mandate additional control measures at hospitals. Moreover, for 3D volumetric imaging, LSM requires optically clear samples. However, this tissue clearing typically requires considerable time, to the order of hours to days, and additional stand-alone equipment, making it impractical in an intraoperative environment [21, 37].

2.4   Stimulated Raman Spectroscopy

Stimulated Raman spectroscopy (SRS) is an imaging technique that takes advantage of vibrational resonance of molecular bonds to provide contrast [38, 39, 40, 41]. The technique typically uses two femtosecond pulsed lasers to stimulate the emission of photons from specific molecular structures. The two lasers, referred to as the pump laser and stokes laser, are temporally and spatially coincident on the sample but differ in their wavelength. If the frequency difference between the stokes and pump lasers matches the vibrational frequency of a molecular bond, stimulated emission of photons occurs. This emission of photons is a weak effect and results as an intensity loss in the pump beam and as a gain in the stokes beam [39].

These intensity changes are small (on the order of 10^{-5} and 10^{-7}) and can be challenging to measure [42]. This limitation is further exacerbated in a reflection-mode configuration as multiple backscattering of photons lowers the collection efficiency with the objective lens, leading to low SNR. The low sensitivity is typically overcome by increasing the incident pulse energy, incorporating lock-in amplifiers, or employing custom photodiodes with a central aperture. The custom photodiodes are placed in front of the focusing objective and allow the excitation lasers to pass through the central opening [43]. The large detection area ensures the collection of a large amount of multiple backscattered photons.

In recent years, SRS has demonstrated histology-like imaging of brain and gastrointestinal tissue using a transmission-mode architecture [23, 24]. These reports imaged human brain tissue and compared the results against H&E stained images. The studies investigated both thin and thick fresh tissue specimens. However, since the reported method operated in transmission-mode, the thick samples were squeezed down to 120 µm by sandwiching them between coverslips [23]. Squeezing the specimen may place considerable pressure on the sample and may change the delicate tissue morphology, potentially interfering with the accurate margin assessment. This process would also hinder the downstream assessment of tissue pathology using standard histopathological techniques. This squeezing would also not be practical when imaging directly within a resection bed.

2.5   Optical coherence tomography

Optical coherence tomography (OCT) is an imaging technique that takes advantage of optical backscattering to visualize tissue contrast [44, 45, 46, 47, 48, 49]. OCT is based on the principle of low-coherence interferometry, where the interference happens only for path length within the coherence length of the light source. The technology is similar to ultrasound imaging and is based on detecting light echoed from different layers of tissue. However, since the speed of light is much higher than sound, typical detectors cannot be used. Therefore interferometers are employed to detect the light coming from layers of tissue. Compared to a high coherence interferometer, a low coherence interferometer only exhibits interference within the coherence length of the illuminating light.

OCT has two major variants, time-domain OCT (TD-OCT) [44] and fourier-domain OCT (FD-OCT) [50, 51, 49, 52]. FD-OCT has two common architectures spectral-domain OCT (SD-OCT) [49, 52] and swept-source OCT (SS-OCT) [47, 53, 54]. Figure 2.2 depicts these variants. In a TD-OCT system (Figure 2.2a) [44], the laser light is coupled into an interferometer where it is split into a reference path and a sample path. The reference path directs the light towards a mirror, which reflects it back to the interference system.

8
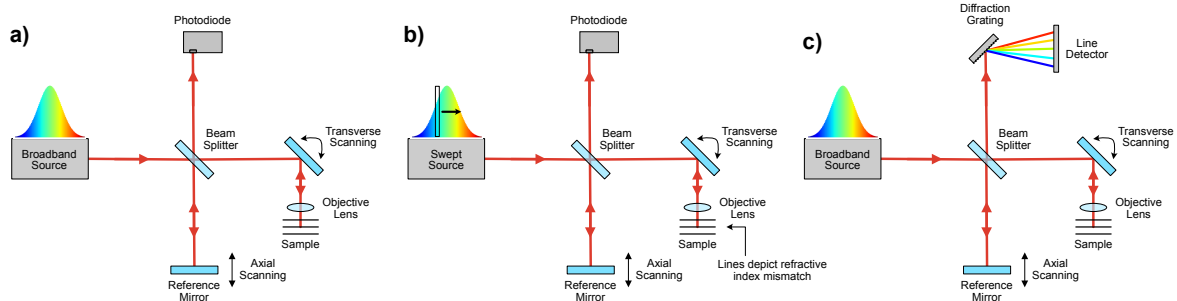
Figure 2.2: Optical coherence tomography **a)** Time-domain OCT **b)** Swept-Source OCT **c)** Spectral-Domain OCT.

Using an objective lens, the sample path focuses the beam into the specimen such that it travels some distance into the target. As light travels some distance within the sample, it is partially backscattered by each refractive index mismatch it encounters. These refractive index changes are due to different layers of tissue and structures within the sample. The backscattered light is collected with the objective lens and subsequently forms an interference pattern with the reference beam. The reference light only forms an interference pattern with light that travels the same optical distance. Thus, as the reference mirror is moved axially, interference patterns are collected along the depth of the sample form an A-scan using a photodiode. To form 2D or 3D cross-sectional images, a set of A-scans is collected as the sample beam is scanned over the sample in a raster-like pattern.

SS-OCT (Figure 2.2b) [53, 54] replaces the broadband laser with a swept-source (a laser that sweeps across wavelengths) and measures the interference as a function of wavelength. SD-OCT (Figure 2.2c) [49, 52] operates on the same principle but retains the broadband illumination of TD-OCT and instead replaces the photodiode with a spectrometer. Most modern OCT implementations are either SD-OCT or SS-OCT. This is because of significant enhancement in speed and sensitivity FD-OCT offers [55, 56, 53, 57].

Being a mature modality, OCT has been investigated a number of times for oncologic imaging [58, 59, 60, 61]. This has included surgical margin analysis, biopsy examination and direct imaging of tissue blocks [62, 63]. Although these studies have demonstrated promising results, the appearance of OCT images is dissimilar to conventional histology slides. This is because histological analysis relies on the specificity of staining to identify different structures in tissues. OCT, in comparison, highlights the shape and distribution of different structures but does not highlight tissue components, such as cell nuclei, red blood cells, or cytoplasm, with sufficient specificity. Many such studies, therefore, require retraining pathologists to interpret OCT histology images [64, 65, 66].

9

2.6 Ultraviolet photoacoustic microscopy

Ultraviolet photoacoustic microscopy (UV-PAM) [25, 26, 27] is a variant of a much broader modality known as optical-resolution photoacoustic microscopy (OR-PAM) [67, 68, 69, 70]. OR-PAM takes advantage of the intrinsic optical absorption of biological tissue to provide contrast [67, 68]. The optical absorption is measured via the photoacoustic effect [71, 72]. The photoacoustic effect refers to the generation of acoustic waves due to modulated or pulsed light being absorbed [70]. Figure 2.3 provided a simplified schematic of a UV-PAM system. The figure shows a pulsed ultraviolet laser being focused onto the tissue specimen. As this pulsed light is absorbed, there is a rapid change in temperature local to the targeted region. This change in temperature leads to transient thermoelastic expansion and generation of ultrasonic waves [73, 74]. These acoustic waves propagate through the tissue and can be detected at the surface of the target using an ultrasonic transducer.

The optical absorption of various biological chromophores varies as a function of wavelength and is highly specific [75]. This enables selective imaging of chromophores by choosing an excitation laser with appropriate wavelength. For example, as hemoglobin absorbs visible light strongly, 532 nm wavelength is a common choice for targeting blood vessels. Taking advantage of versatility, OR-PAM has demonstrated excellent contrast and resolution when imaging microvasculature [76], blood oxygenation levels [77], melanin [76, 78, 79] and lipids [76, 80, 81], among others [82]. Similarly, since DNA exhibits strong optical absorption in the ultraviolet range, UV-PAM commonly employs a 266 nm wavelength to highlight nuclear morphology. The major difference between OR-PAM and UV-PAM is simply the excitation laser employed.
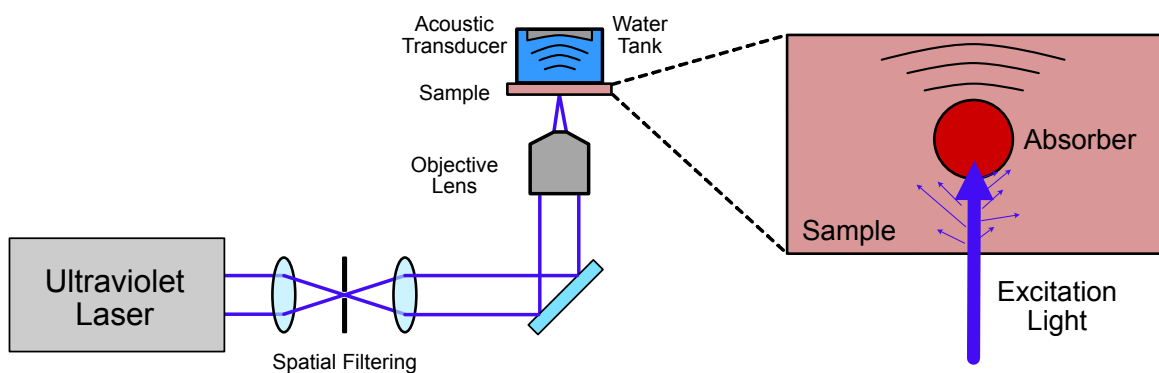
Figure 2.3: A simplified schematic of ultraviolet photoacoustic microscopy.

Yao *et al.* reported the first UV-PAM system and demonstrated the label-free recovery of cell nuclei with a reflection-mode configuration [25]. The system's effectiveness was illustrated with *ex-vivo* and *in-vivo* imaging of mouse tissues. However, to operate in reflection mode, this system required a custom-built transducer. Imaging tissue with an ultraviolet wavelength is similar to staining with hematoxylin as it would only highlight cell nuclei of the sample and not the surrounding cytoplasm. A later study used a tuneable 420 nm laser to target cytochromes in addition to nucleic contrast [27]. In 2017, UV-PAM was demonstrated with thin sections of human breast tissue and demonstrated close agreement with standard H&E stained samples [26].

Despite its efficacy, the ultrasonic transducer required by photoacoustic microscopy imposes two major constraints. First, UV-PAM (and OR-PAM) systems depend upon a strong confocal arrangement between the acoustic and optical beams [68, 69]. Otherwise, the resulting acoustic waves from the absorber may not be detected by the transducer. This optoacoustic geometry imposes also imposes limitations on employing high numerical-aperture (NA) objectives in a reflection-mode configuration [76]. In a reflection-mode configuration, the acoustic waves redirected towards the transducer using an optoacoustic beam splitter. The beam splitter is placed between the objective lens and the sample. This takes up valuable working distance of the focusing lens and precluding the use of high NA objective lenses. To overcome this, reflection mode UV-PAM systems employ complex devices such as ultrasonic transducers arranged in a ring array around the objective or transducers with a central opening such that the excitation laser is passed through [76, 25]. The second constraint is the requirement of effective acoustic coupling with the target. This is because acoustic waves are attenuated significantly if an impedance mismatch is found, such as when acoustic waves encounter the surface of biological tissue and attempt to transmit in air. To achieve effective acoustic coupling with the target, UV-PAM submerges the ultrasonic transducer and parts of the apparatus in a water tank. The water serves as an impedance matching medium between the tissue and the transducer. To date, all UV-PAM methods have submerged the apparatus in water to achieve effective coupling [25, 27, 26]. However, this makes it difficult to optically scan the excitation laser unless special water immersible microelectromechanical systems (MEMS) mirrors are used and imposes additional restrictions for real-time imaging. The water immersion also makes it unfeasible to deploy UV-PAM for *in-situ* imaging. This is discussed in significant detail in Chapter 4 for real-time imaging applications.

2.7   PARS microscopy

Considering the limitations posed by an ultrasonic transducer in conventional photoacoustic systems, a significant amount of research has sought an all-optical non-contact reflection-mode photoacoustic technique to image biological tissues [83, 84, 85, 86, 87, 88]. However, the majority of these approaches rely on interferometric methods to either measure sample surface oscillations or to observe photoacoustic stresses. While these methods provide optical detection of the ultrasonic pressures, they tend to offer poor sensitivity and are susceptible to undesired path changes in the interferometer.

PARS is an all-optical technique that replaces the acoustic detection of thermoelastic pressures with a second continuous-wave detection laser [9, 10]. Unlike previous efforts, this technique measures optical absorption contrast by monitoring changes in the intensity of this detection laser and is insensitive to phase modulations or path changes in the optical setup. This leads to a robust all-optical non-contact reflection-mode detection of photoacoustic pressures. Much of the work on PARS, including the discovery of the PARS imaging effect, design of the initial optical system, and the first two seminal reports, were lead by the author's supervisor, Parsin Haji Reza, at the University of Alberta.

A simplified system diagram of a PARS system is provided in figure 2.4. Similar to
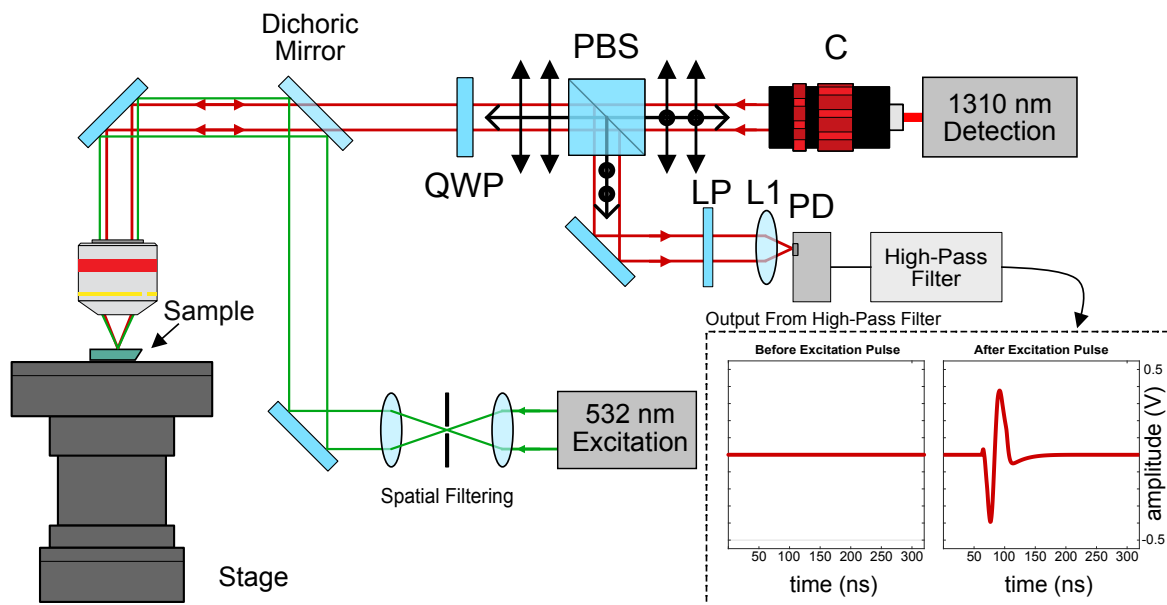
Figure 2.4: A simplified schematic of PARS microscopy. Component labels are photodiode (PD), long pass filter (LP), polarized beam splitter (PBS), quarter-wave plate (QWP), collimator (C).

12

conventional photoacoustics, PARS employs a nanosecond pulsed laser to excite ultrasonic pressures in biological tissues. A second detection laser, which operates in continuous mode and is co-focused with the excitation laser on the sample. These beams are reflected from the sample and directed towards a photodiode. A long-pass filter is typically placed before the photodiode to block any excitation light and to ensure the detector only measures the detection laser's intensity. Initially, before applying any excitation light, only the detection laser is incident on the sample. In this state, the reflected light from the sample would have a constant intensity (effectively a DC signal). This constant light is due to the backscattering from the sample. As an excitation pulse is applied, a small and rapid oscillation is found to be imposed on the back-reflected light. The photodiode voltage output is typically high-pass filtered to only extract the rapidly oscillating signal and reject the scattering signals.

This effect was first described by the initial report on PARS using a two-state model in Nature's *Light Science & Applications* [9]. As this is a novel mechanism, a brief discussion is provided here for the benefit of the reader as well as an illustration in figure 2.5. The
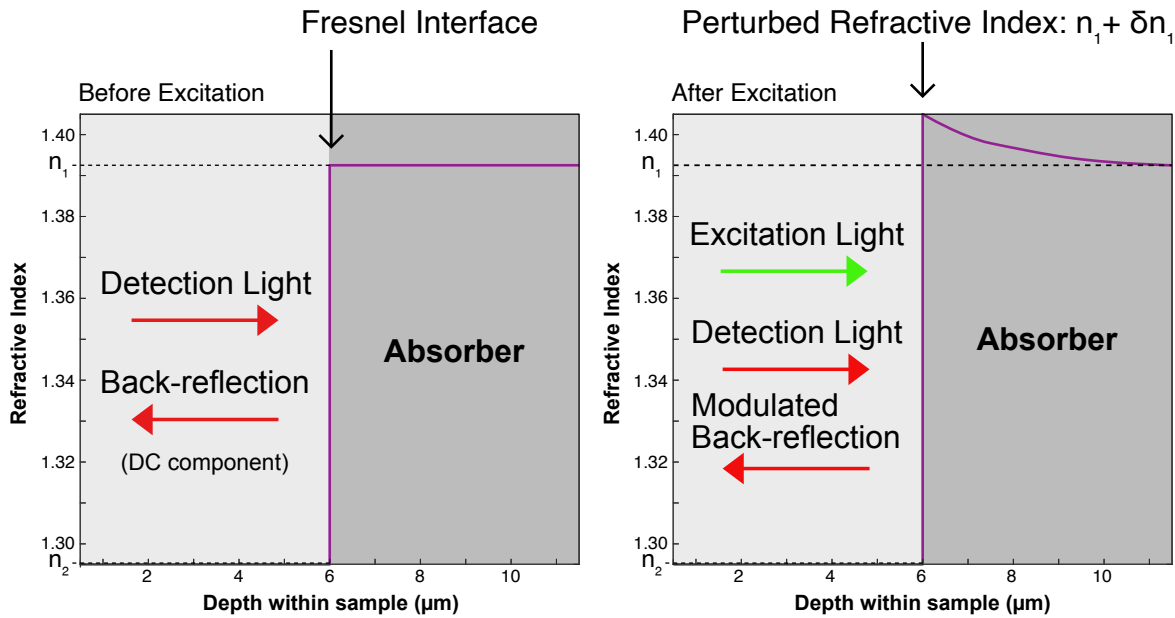
Figure 2.5: A qualitative illustration of the PARS mechanism via the two-state model. a) depicts a fresnel interface prior to excitation. Some of the detection is back-reflected while the other passes into the absorbing medium. b) depicts the fresnel interface after excitation. The refractive index is perturbed which modulates the reflectivity of the interface. The modulated reflectivity appears as a modulated back-reflection of the detection light.

13

thermoelastic pressures excited due to the excitation laser are linearly proportional to the optical absorption and the amount of fluence on the target. As these acoustic pressures propagate through the target, they modulate the refractive index of the medium due to the elasto-optic effect [89] (purple curve in the figure). The change in refractive index leads to a change in reflectivity of the sample. These reflectivity changes can be observed as fluctuations in the back-reflection intensity of the detection laser. For the case of normally incident light, the reflectivity $\mathbf{R}$, can be calculated using Fresnel equations as $R = |(n_1 - n_2)/(n_1 + n_2)|^2$ where $\mathbf{n}_1$ and $\mathbf{n}_2$ are refractive indices of two media within the tissue. Assuming the excitation laser is incident on $\mathbf{n}_1$, we can express a slight perturbation in its refractive index as $n_1 + \delta n_1$. The reflectivity can now be described as $R' = |(n_1 - \delta n_1 - n_2)/(n_1 + \delta n_1 + n_2)|^2$. As PARS only measures the resulting transient oscillations, we can express the change in reflectivity as $\Delta R = R - R'$. This can be shown to be $\Delta R = \propto \delta(n_1 - n_2)$. The key insight provided by Haji Reza $et\ al.$ is the fact that the PARS effect is amplified if there is an existing refractive step between the media [9]. Without this preexisting refractive index contrast, the reflectivity change is subtle. Though this may seem to be of little use in practice, scattering and optical absorption contrast exists prevalently throughout biological tissue. Subsequent works extended this model to include temporal and spatial dimensions [11, 12].

Through this effect, PARS has demonstrated high-resolution $in\text{-}vivo$ imaging of microvasculature structures [11], deep sensing capabilities [10], and functional imaging [90]. The intensity-modulated optical detection mechanism presents several benefits over previous approaches.

(i) PARS relies on an optical confocal geometry between the excitation and the detection laser. This confocal geometry is significantly simpler than the optoacoustic confocal geometry of OR-PAM and does not require additional components between the focusing objective and the target. Compared to optoacoustic confocal geometry, the optical confocal geometry yields a significantly simpler light delivery system and enables high-resolution real-time imaging in a reflection-mode architecture.

(ii) The optical confocal geometry also eliminates the requirement of acoustic coupling leading to non-contact detection of photoacoustic pressures. The non-contact detection minimizes the risk of infection in clinical settings and also does not require the apparatus to be submerged in water.

(iii) The PARS detection mechanism measures the initial pressures local to the targeted absorber and is primarily limited by stress confinement conditions. The initial pressures dissipate in a few hundred nanoseconds and lead to significantly faster imaging

14

rates, potentially in the range of tens of megahertz [11]. In contrast, conventional photoacoustic microscopy typically needs to wait for a minimum interval of time for the ultrasonic pressures to propagate through the tissue. The minimum interval is dependent on the speed of sound in tissue and the image depth. Assuming that the average speed of sound in biological tissue is 1540 mm/s [91], it will take the acoustic waves about 0.65 µs to propagate over an imaging depth of 1 mm. The maximum repetition rate is thus 1.5 MHz. If an excitation pulse is applied before this minimum interval, acoustic waves within the sample can potentially interfere with each other and lower the contrast and resolution.

(iv) PARS takes advantage of optical absorption to visualize contrast and does not require the use of exogenous dyes. The label-free approach yields a modality that can be deployed in clinical settings and may not require special control measures or precautions.

(v) The all-optical design enables PARS to be combined with other imaging modalities to capture additional contrasts and provide pertinent diagnostic information to the clinicians. For example, PARS can be combined with OCT to capture scattering contrast from deep within samples [92]. The optical design also lends itself to being miniaturized to an endoscope to visualize absorption contrast deep within the body.

The non-contact label-free reflection-mode capabilities position PARS to be a powerful microscope that may one day visualize surgical margins *in-situ* or immediately enable morphological assessment during biopsies, saving valuable time in the formulation of treatment plans and improving patient outcomes. Employing PARS, this thesis investigates the possibility of using PARS for visualizing nuclear morphology in thin and thick tissue specimens. This study approaches the limitations of standard histopathology by first demonstrating wide field of view imaging using mosaics followed by a method to provide live feedback to the clinicians. Nuclear morphology is then demonstrated in human breast, gastrointestinal, and skin in unstained tissue slides as well as FFPE tissue blocks which serve as an analog to fresh tissue or *in-situ* imaging. Finally, we expand upon the chromophores imaged by incorporating a 532 nm excitation laser to target hemoglobin contrast.

Chapter 3

Rapid High-Resolution Mosaic Acquisition for Photoacoustic Remote Sensing

3.1 Motivation

Standard histopathology typically does not assess entire tissue specimens. Instead, pathologists typically sample the specimen macroscopically and select areas of interest for further processing. These samples are no larger than a few centimeters [93]. This sampling works fairly well as long as there is a readily apparent or palpable abnormality in the specimen. In many cases, particularly after neoadjuvant chemotherapy, such abnormalities are not visible, and the tumor must be localized before further assessment. A potential solution is large-format histology where samples considerably larger than a few centimeters are assessed. However, processing large sections of tissues requires specialized equipment which may not be available widely [94]. Intraoperatively, frozen section analysis is similarly limiting. Frozen sectioning of surgical margins is usually limited to only a small part of the tissue, leaving a significant amount of the sample unexamined. This results in a higher positive surgical margin rate and, consequently, higher cancer recurrence rates [95].

Rapidly imaging large areas of tissue with cellular-scale resolution is typically nontrivial as it requires the specimen to sampled densely at a high scanning speed. Point by point microscopy typically uses mechanical stages to capture wide field of views. However, mechanical scanning moves the target underneath the targets which becomes unfeasible for larger heavier targets due to their momentum. Thus, mechanical stages are typically moved

16

at a slow speed leading to time-consuming acquisitions. An alternate is optical scanning where a pair of orthogonal mirrors steer the beam onto the target. Optical scanning is significantly faster than mechanical stages and is not limited by the momentum or weight of the target. A strong advantage of optical scanning is it allows for dense sampling of the target leading to high resolution images. Nonetheless, the field of view afforded by optical scanning is significantly smaller than mechanical stages.

Mosaics have been widely used in microscopy [96, 97, 98, 99] and combine rapid optical scanning with the wide field of views afforded by mechanical stages. Mosaics use optical scanning to image small field of views rapidly and a mechanical stage to move the target to an adjacent location to capture another localized patch or frame. Previously, works have reported mosaic acquisition methods for conventional photoacoustic systems [99, 98]. Shao *et al.* reported a mosaic acquisition method for optical-resolution photoacoustic microscopy with a step size of 1.2 µm [98]. The reported method can acquire a 6.45×5.8 mm^2 field of view in ninety seconds [98]. Despite the rapid acquisition reported in [98], the 1.2 µm step size limits the resolution of the system to approximately 2.4 µm. However, as PARS has demonstrated sub-micron resolution in a reflection-mode configuration, it necessitates a method that is capable of rapidly acquiring large field of views while maintaining a sub-micron step size and high-resolution [10]. In light of the limitations posed by the mechanical stages and optical scanning, the author implemented mosaic acquisition for PARS. This chapter describes the image acquisition, reconstruction and optical apparatus in detail for mosaic capture with PARS. A unique advantage of this method is that it minimizes the stage movement during scanning. This makes it possible to mount the optical components on top of the mechanical stages and therefore enable scanning of specimens too heavy or large to be moved. Using the technique described in this chapter, images of carbon fiber networks and unstained histology samples are presented to demonstrate the method's efficacy.

3.2   Methods

In this section we describe the optical apparatus, image acquisition and reconstruction. The mosaicking technique is validated with human tissue specimens prepared using standard histology techniques. More information on sample preparation is provided in section 5.1.3.

17
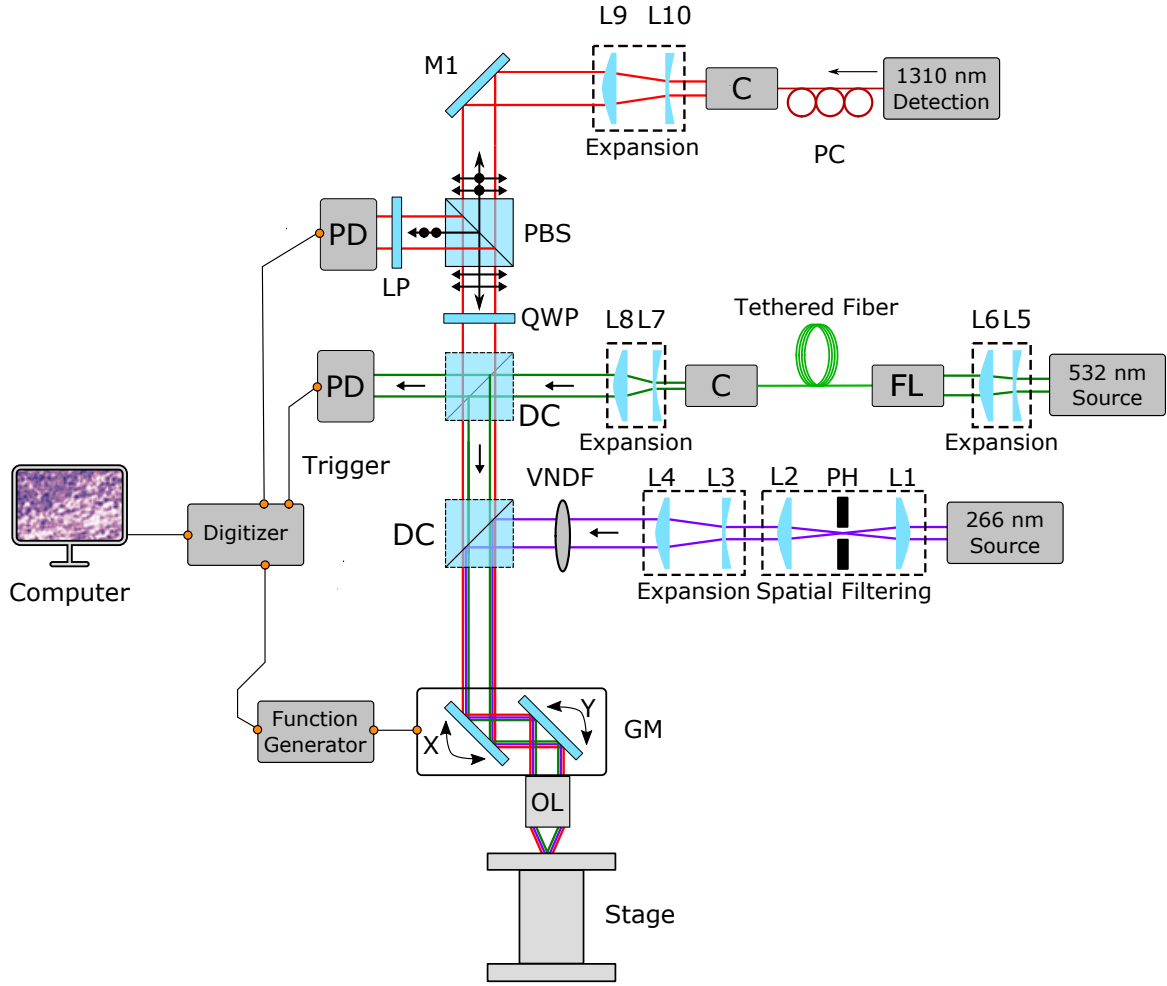
Figure 3.1: Schematic of the PARS microscope. Components labels are: pinhole (PH), variable neutral density filter (VNDF), collimator (C), polarized beam splitter (PBS), quarter waveplate (QWP), dichroic mirror (DC), photodiode (PD), fiber launch (FL), galvanometer mirrors (GM), lenses (L), mirrors (M).

3.2.1 Experimental Apparatus

The optical setup closely follows the conventional PARS setup shown in figure 2.4. The apparatus described in this chapter employs two excitation sources, as shown in figure 3.1, and was the first report of a multi-wavelength PARS system [100]. The 532 nm excitation source repeats at a rate of 600 kHz and is used to demonstrate rapid mosaic acquisitions. The 266 nm source is used to image histology specimens. A more detailed study of histology-like imaging is carried out in Chapter 5 and 6, with Chapter 6 using the setup

described in figure 3.1 for chromophore selective imaging. The incorporation of multi-wavelength excitation required the use of an additional dichroic mirror to combine the 266 nm light with the 532 nm excitation and 1310 nm detection light. It is important to note that presently the system does not operate with two excitation sources simultaneously.

The 266 nm beam is spatially filtered using a 25 m pinhole and collimated by two lenses. The collimated beam is expanded using a variable beam expander and combined with the 1310 nm and 532 nm beams using a dichroic mirror. The 532 nm beam is collimated and expanded to be coupled into an optical fiber. Then, a fiber-coupled collimator outputs the light, which is further expanded to fill the aperture of the objective lens and combined with the rest of the system with a dichroic mirror. The 1310 nm detection path operates identically to previous PARS reports and is described in section 2.7 [9, 10]. The co-aligned detection and excitation beams were then directed to a set of 2D scanning mirrors (GVS412, Thorlabs Inc.). The scanning mirrors were mounted at right angles to each other and were able to steer the beam to any given point in the field of view. The amount and rate of the swing are determined by the input waveform's amplitude and frequency, respectively. The co-scanned beam was targeted onto the tissue, which is held on top of a set of x-y linear scanning stages (XM-100S, Newport Inc.). The back-reflected circularly polarized light from the sample was sent back through the quarter-wave plate to be converted into vertically polarized light. The polarized beam splitter then reflects the vertically polarized light onto the photodiode (PDB425-C). A four-channel data acquisition card (CSE161G4, DynamicSignals LLC) is used to record the photoacoustic signal along with the fast and slow mirror positions. The excitation source is used as the trigger for the data acquisition card, which records the mirror signals for positional information and the PARS signals. The scanning mirrors are driven using a function generator and are not triggered or synchronized.

3.2.2 Mosaic Acquisition

Optical scanning forms the basis of mosaic acquisitions. A mosaic is formed by acquiring a sequence of frames constructed by optical scanning in a two-dimensional grid. A custom acquisition software was developed by the author in `C++` to interface with the data acquisition card and the mechanical stages. The software programs the data acquisition card with the desired frame point count, the length of time to record after each trigger, and the sampling rate. It also sets the speed of the mechanical stages and moves them in a two-dimensional grid to acquire mosaic frames. The software computes the grid's coordinates based on the grid size, the field of view of each frame, and the desired overlap between each frame. The distance between each adjacent frame's center depends on the required field

19

of view per frame and the desired overlap. The degree of tilt of the scanning mirrors and the objective lens determines the field of view. The mirrors are controlled using two ramp waveforms fed from a function generator. In contrast to sinusoidal waveforms, the use of ramp waveforms allows for a more consistent step size between each point acquisition. This is due to having a constant acceleration until the halfway point where the waveform flips and decreases again with a constant acceleration. In comparison, a sinusoidal waveform will have varying acceleration throughout its period. As a ramp waveform has a quick turnaround at the halfway point, it also results in less dwell time, limiting the heat dissipation on the sample. Typically sudden changes in a waveform lead to electronic ringing effects which can potentially deteriorate the image quality. However, such effects were not observed with this system. The amplitude and frequency of these mirrors along with the laser repetition rate, determine the step size between each point acquisition. For example, with a repetition rate of 40 kHz, mirror frequencies of 120 mHz and 60 Hz yield a step size of 570 nm when the field of view is $380 \times 380 \ \mu m^2$. Similarly, when the laser repeats at 600 kHz, mirror frequencies of 1.8 Hz and 960 Hz are used to yield a step size of 200 nm with a field of view of $121 \times 121 \ \mu m^2$. The 960 Hz swing rate is under the bandwidth of the mirrors, which are capable of a 1 kHz swing rate if mirror deflection is less than 0.2°.

As discussed in section 2.7, conventional photoacoustic microscopy usually waits till the acoustic pressures have propagated through the tissue before applying a subsequent excitation pulse [75]. During this interval, the acquisition process typically records the propagation of ultrasound through the tissue. A depth of 1 mm would correspond to a recording time of about 650 ns. In contrast, PARS measures the initial acoustic pressures near the absorber and a recording interval of approximately 300 ns is sufficient to record the back-reflected intensity modulations observed by the photodiode [9, 10]. The shorter recording intervals halve the amount of data that needs to be transferred and processed. The data acquisition card is set to a sampling rate of 200 MS/s, resulting in 64 element segments for each point acquisition and is used for all acquisitions presented. The 200 MS/s sampling rate is chosen to satisfy the 75 MHz bandwidth of the photodiode. The point acquisitions are streamed to the computer while the scan is in progress. Once the desired number of point acquisitions are acquired, the in-house developed software writes the mirror signals and the time-domain PARS signals to disk. As soon as the data have been written, the software moves the mechanical stages such that the next frame in the sequence can be acquired and enables the data acquisition card to begin the next scan. This movement is rapid and takes approximately 100 ms.

3.2.3   Mosaic Reconstruction

Figure 3.2 provides a visual overview of the reconstruction process. The acquisition process results in a collection of points spread over the field of view. Each point has an x and y coordinate and a PARS signal associated with it (Figure 3.2a). The Hilbert Transform is employed to compute the upper and lower envelopes of the signal, shown as the orange and green dashed curves in Figure 3.2a [101, 102, 103, 104]. The amplitude of these envelopes (blue lines) determines the intensity values of the scatter data (Figure 3.2b). To render an image, the scattered dataset is triangulated using Delaunay Triangulation (Figure 3.2c), which leads to an optimized triangulation of the data and minimizes interpolation artifacts due to elongated triangles [105, 10, 106]. Delaunay Triangulation has been widely used in literature for surface reconstruction from scattered datasets [107, 108, 109]. Since the scatter data must be rendered on a Cartesian grid to form an image, such a grid is imposed over the triangulation as an image as points to be interpolated (Figure 3.2d).

Using linear interpolation, the intensity at each Cartesian point is then computed from the resulting triangulation. This results in a rendered image, as shown in Figure 3.2f. The Grid/Stitching plugin in Fiji software is used to assemble all the mosaics presented in this study [110]. This plugin computes a correlation between the overlapping regions to calculate the best registration transformation. In addition, it applies a linear blend on the overlapping areas to smooth out any hard edges on adjacent patches within the mosaic.

21

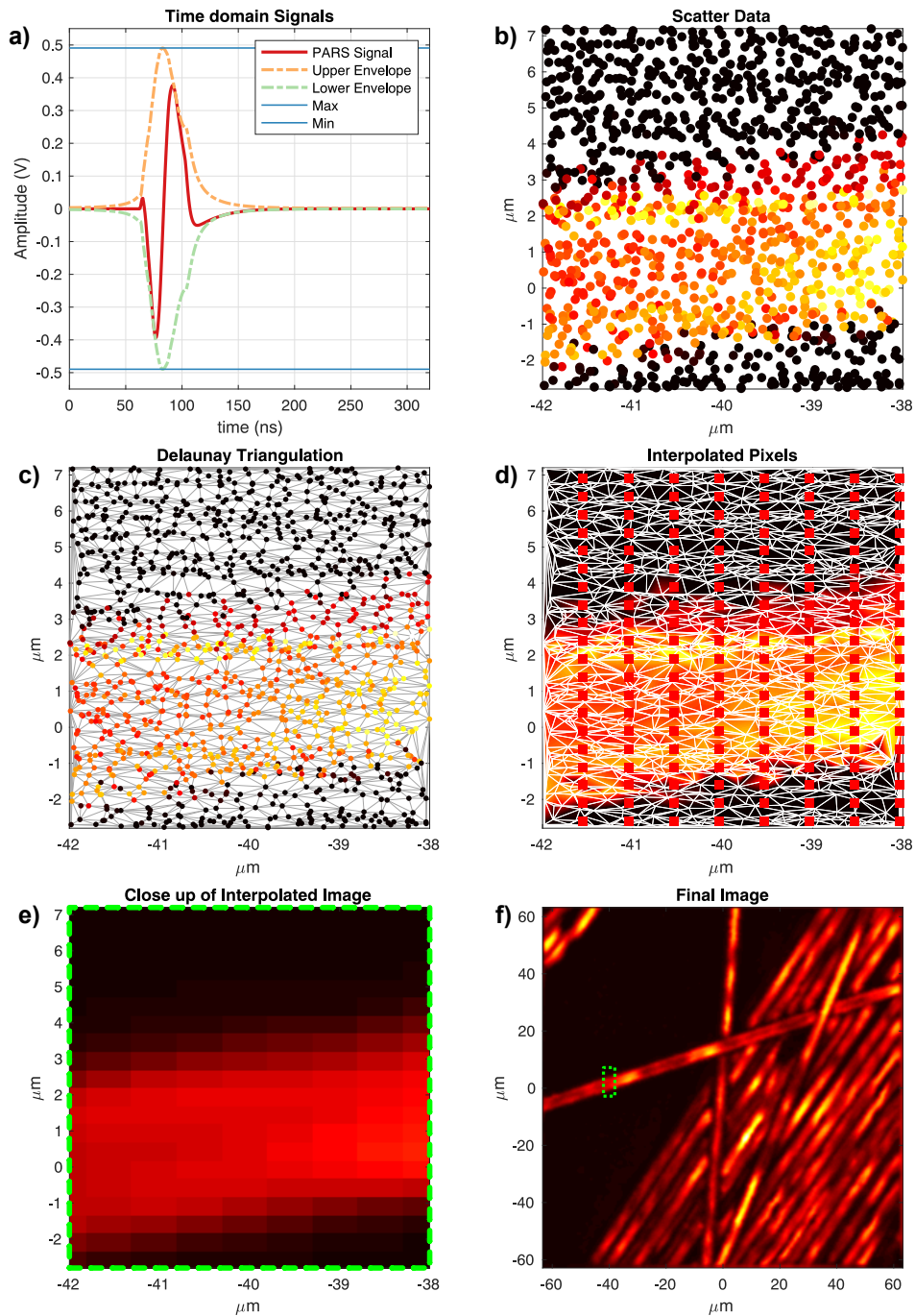**Figure 3.2:** **(a)** PARS time-domain signal with upper and lower envelopes **(b)** raw scatter data **(c)** Delaunay triangulation **(d)** cartesian grid imposed on Delaunay triangulation **(e)** close up of interpolated pixels **(f)** reconstructed image.

3.3   Results and Discussion

To illustrate how well the mosaicking approach works, we capture three mosaics. The first capture, a 0.8×0.8 mm^2 mosaic of carbon fiber networks composed of one hundred frames was acquired at a repetition rate of 600 kHz (Figure 3.3). Each frame covers an area of 121×121 µm^2 and consists of 400,000 raw point measurements. Operating at 600 kHz, the acquisition time for each frame takes 0.66 seconds, with the total acquisition time amounting to seventy seconds. At such repetition rates, the mirrors must be scanning at 1.8 and 960 Hz. This image demonstrates the rate at which wide field of views can be acquired while maintaining dense spatial sampling. Operating at 600 kHz, the acquisition time for each frame takes 0.66 seconds, with the total acquisition time amounting to seventy seconds. At such repetition rates, the mirrors must be scanning at 1.8 and 960 Hz. Operating at these frequencies poses two major limitations for acquisition in the current system. First, the scanning mirrors can only operate at low voltages and hence cover only a small field of view rapidly. Second, the high frequencies increase the heat generation of the control electronics significantly and do not allow for a sustained operation. This can be mitigated by actively cooling the electronics. A wider field of view can be achieved, while operating at low voltages, by using a wide-angle objective lens. A wide-angle would effectively 'see' more of the target and would allow the laser to be steered on a bigger area.

Figure 3.4 demonstrates the system's ability to acquire a large field of views with a high number of frames. Four hundred frames were acquired with a 35% overlap to ensure good image registration. Each frame has a field of view of 380×380 µm^2 and is composed of 400,000 raw data points. At a laser repetition rate of 40 kHz, each frame took 10 seconds to acquire, with the total time being 66 minutes for the entirety of the mosaic.

To further validate the technique on practical real-world specimens, we image a human breast tissue specimen with invasive ductal carcinoma (Figure 3.5). Two tissue slides are prepared using adjacent sections from the formalin-fixed paraffin block. One slide is stained with H&E dyes and imaged using a conventional bright-field microscope (Figure 3.5a). The other slide is left unstained and imaged using the PARS microscope (Figure 3.5b). The PARS microscope utilizes a 266 nm laser to provide DNA constant. The PARS image is a mosaic of one hundred frames, with each frame being 85×85 µm^2 and consisting of 100,000 points. The total field of view is approximately 1×1 mm^2 and took 470 seconds to acquire. The acquisition time, in this case, is limited by the 21 kHz repetition rate of the 266 nm laser. Figure 3.5b is effectively a map of the optical absorption of DNA present within the sample. The darker regions denote areas of high signal and thus abnormal growth of cells. The bottom half of the image is significantly sparser and shows healthy tissue. The boundary between the sparse area and the abnormal cell growth area is the cancer margin.

	Field of View	Step Size	Point Count	Rep. Rate	Acquisition Time
Proposed Method Figure 3	0.8 x 0.8 mm^2	200 nm	400,000	600 kHz	70 s
Proposed Method Figure 4	3.0 x 3.0 mm^2	600 nm	400,000	40 kHz	66 min
Proposed Method Figure 5	1.0 x 1.0 mm^2	260 nm	100,000	21 kHz	8 min

Table 3.1: Summary of results of the proposed system.

This boundary is visualized with similar fidelity as the standard H&E image in figure 3.5a. Additionally, two necrotic regions are also visualized in both the PARS image and the H&E image. More detail is shown in figure 3.5c and 3.5d where individual cell nuclei can be seen.

Previously, Hu *et al.* have reported an acquisition time of 70 minutes for an area of 7.8 × 10 mm^2 with mechanical stages [69]. However, the reported acquisition utilized a step size of only 2.5 µm. With a similar step size, the proposed method in this work would acquire a single frame with a field of view of 380 × 380 µm^2 in 0.5 s. To acquire a 10 × 10 mm^2 image, the total acquisition time would be 7 minutes at a 40 kHz repetition rate. With a 600 kHz repetition rate, the total acquisition time would reduce to approximately 26 s, yielding a significantly faster system which is vital for point by point scanning microscopes. The significant increase in speed seen in this work can be traded for a smaller step size resulting in higher sampling resolution. Similarly, other works on the subject have reported results with a limited repetition rate, step size, and resolution as compared to this work [98]. Employing a wide-angle lens, each frame is acquired in one second and covers a field of view of 930 × 930 µm^2 consisting of 160,000 measurements. The increased spot size allows for a step size of 1.2 µm between point acquisitions lowering the number of points required per frame at the cost of resolution. In contrast, here we are able to acquire a 400,000 point frame in 700 ms, including the acquisition and stage movement time at a resolution of 1.2 µm and a step size of 200 nm. The 600 kHz repetition rate halves the acquisition time while the transfer time is eliminated by streaming the data while the scan is in progress. Employing a similar wide-angle objective that results in a frame size of 930 × 930 µm^2, an area of 9 × 9 mm^2 can potentially be acquired in seventy seconds with the same point count per frame. A lower point count will further increase the rate of the acquisition.
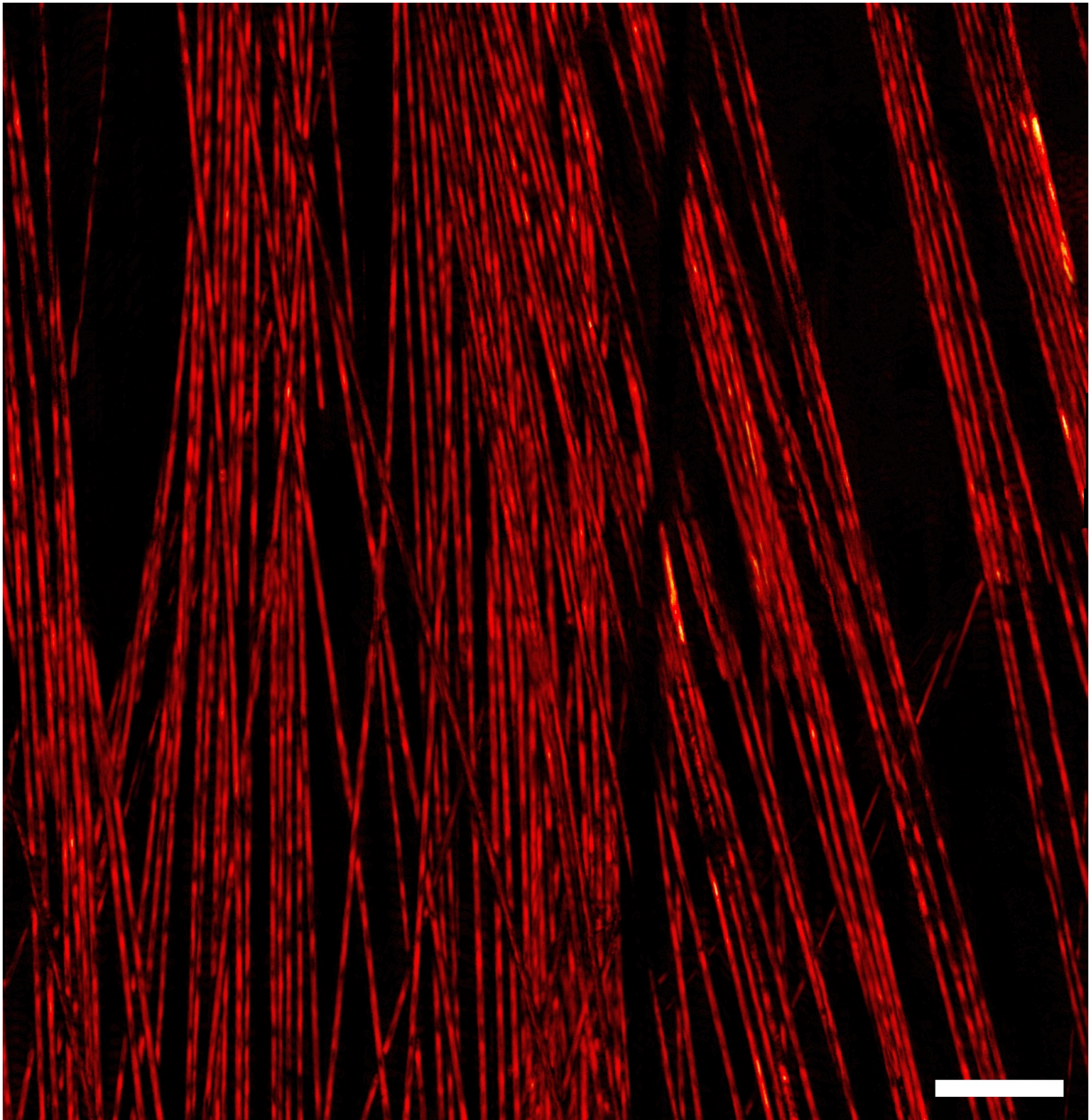
Figure 3.3: A 100-frame mosaic, arranged in a 10 × 10 grid. Each frame is 125 × 125 µm², whereas the total field of view is approximately 0.8 × 0.8 mm². The image was acquired with a 532 nm excitation source operating at 600 kHz. Despite the fast scanning frequencies, the resulting image is able to resolve carbon fiber networks as close as 1 µm throughout the field of view. This resolution is evident with in the top right corner with several distinct carbon fibers running in parallel. Scale bar 100 µm.
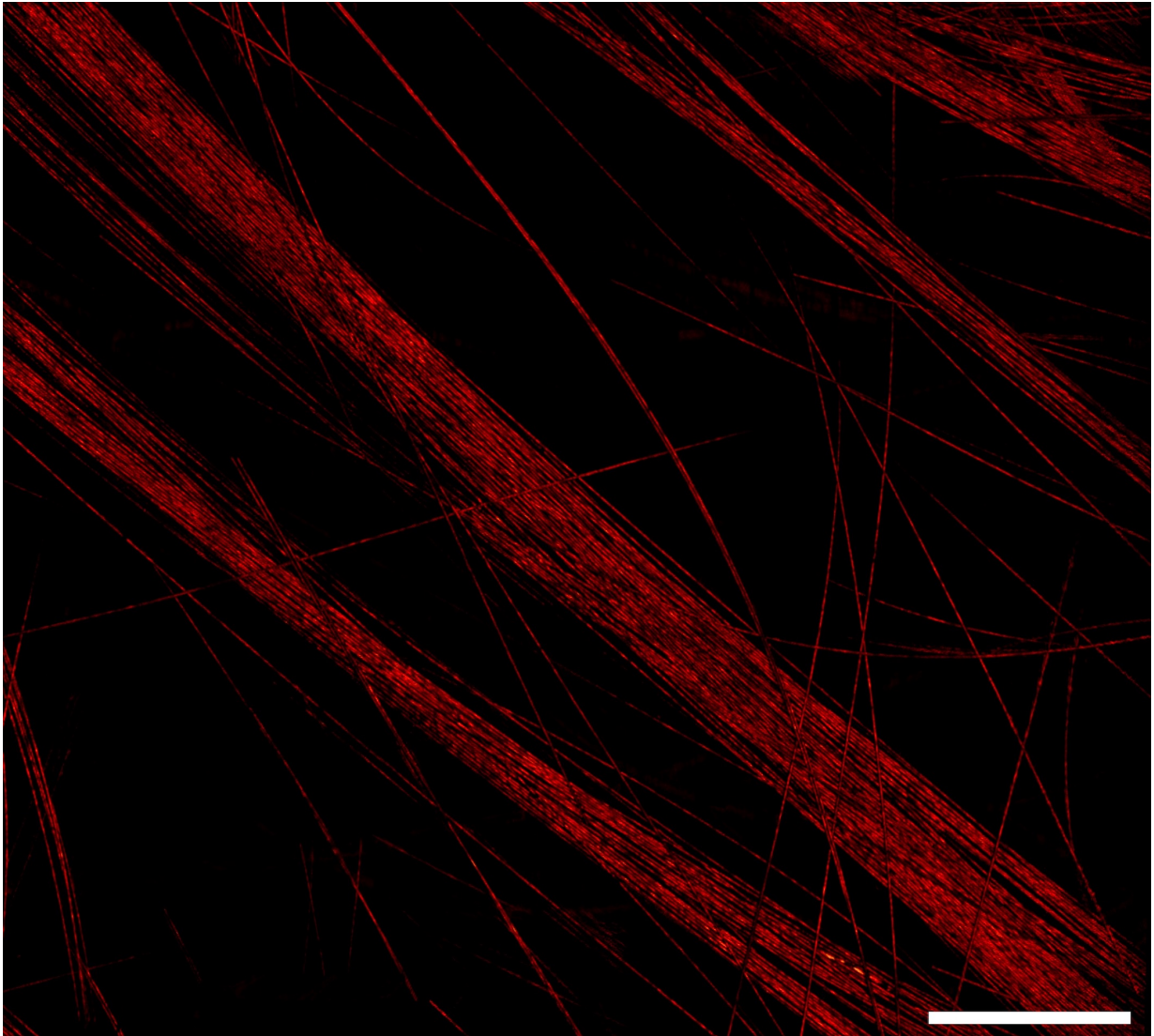
Figure 3.4: A 400-frame mosaic of carbon fiber networks, arranged in a 20×20 grid. Each frame has a field of view of 380×380 µm^2, whereas the total field of view is 3×3 mm^2. The image was acquired with a 532 nm excitation source operating at 40 kHz. The mosaic captures large swathes of carbon fibers with a relatively thick bundle running across the diagonal. The effects of depth of field are also visible as some carbon fibers disappear underneath other fibers (top right) while others run above the thick diagonal bundle (bottom right). Scale bar 500 µm.
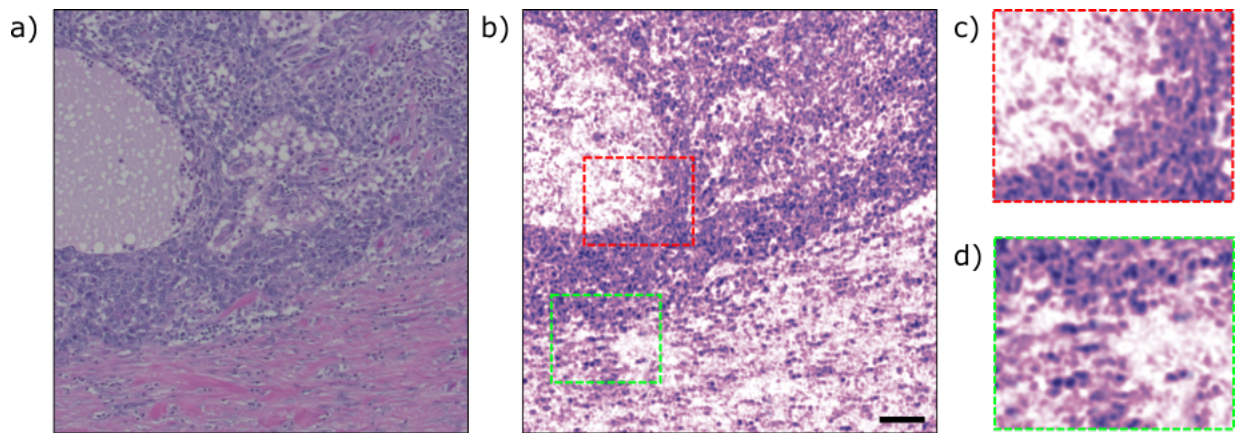
Figure 3.5: A comparison between a PARS image of unstained human breast tissue with conventional bright-field microscope. **(a)** a standard H&E stained image **(b)** a PARS mosaic of one hundred frames, total field of view of 1×1 mm^2 **(c,d)** zoomed in versions of **(b)** showing cell nuclei. The image was acquired with a 266 nm excitation source operating at 20 kHz. Scale bar 100 µm.

Chapter 4

Live feedback and 3D Photoacoustic Remote Sensing

Pathologists are accustomed to the instantaneous visual feedback provided by conventional light microscopes. This instantaneous visual feedback is often leveraged by rapidly panning and zooming in on histology slides to quickly assess tissue specimens. For successful clinical adoption, virtual histopathology techniques would need to mimic this visual feedback by providing a high-resolution live video to clinicians. One important example is *in-situ* imaging, where the video display can be used to guide the imaging head over the tumor to visualize the cancer margin in real-time. To this end, in this chapter, we discuss the development of a real-time imaging method. We begin by discussing the challenges faced by conventional photoacoustic methods and then explain why PARS is a promising solution for a video-rate *in-situ* surgical microscope.

As previously mentioned, conventional PA microscopy methods rely on a strong confocal geometry between the excitation beam and the resulting acoustic waves from the target [111]. This imposes several constraints in terms of component placement in the light delivery system and generally requires a trade-off between resolution, signal to noise ratio (SNR), the field of view, rate of imaging and the imaging depth. In preceding years, a variety of methods have been developed to increase the rate of acquisition. Xie *et al.* employed scanning mirrors to raster-scan the laser over the target while keeping the ultrasonic transducer stationary [112]. Despite significant increases in imaging speeds over mechanical scanning, this method suffers from low SNR due to an unfocused transducer, which results in a weak confocal arrangement between the optical and acoustic beams [112]. Hybrid scanning methods, where the fast axis is scanned optically and the slow axis is scanned using a mechanical stage, have demonstrated fast imaging rates with a

28

linearly focused transducer but result in non-portable systems due to bulky mechanical stages [113, 114]. Micro-lens arrays have been employed to increase the rate of imaging significantly, but require lasers with significant pulse energy. These systems may also result in an increased rate of heat deposition over the target, which may not be feasible for clinical settings [115, 116]. Water immersible two-axis micro-electromechanical system (MEMS) mirrors have been employed to maintain the confocal arrangement between the acoustic and the optical beam and enable rapid imaging for OR-PAM systems with a high SNR [117]. MEMS mirrors, nevertheless, suffer from a reduced field of view unless they are operated at their resonant frequencies. In recent years, water immersible hexagonal mirrors have also been employed to increase the rate and area of scanning while maintaining the strong confocal arrangement afforded by MEMS mirrors. However, this method reported a resolution of 10 µm due to the use of a low NA objective lens [118]. In these works, to maintain a confocal optoacoustic geometry, the scanning optics need to be placed between the objective lens and the target. However, this precludes the use of high NA objective lenses due to their small working distances and leads to low-resolution imaging systems. While hexagonal and MEMS mirrors have resulted in systems with improved sensitivity and scanning rates, the imaging speed for conventional PA microscopy is ultimately limited by the rate of acoustic propagation. This is because excitation pulses that have been fired in quick succession can lead to acoustic interference within the sample as the ultrasonic pressures propagate. To avoid this interference, there is typically a minimum interval between consecutive excitation pulses depending on the imaging depth, leading to a trade-off between imaging depth and speed. For example, when imaging a sample with a thickness of 1 mm, there must be a minimum interval of 0.65 µs between consecutive excitation pulses to avoid acoustic interference within the sample. This leads to a maximum laser repetition rate of 1.5 MHz [75].

In contrast, PARS relies on an all-optical confocal geometry between the excitation and detection laser. This all-optical confocal arrangement is considerably simpler and is free from constraints imposed by an optoacoustic confocal geometry, leading to a more versatile design that can offer high resolution and SNR simultaneously in a reflection-mode architecture. Unlike conventional PA microscopy, PARS relies on initial pressure measurements for contrast and is not limited by the rate of ultrasonic propagation. Instead, PARS is mainly limited by stress confinement conditions and usually requires short point acquisitions, typically in the range of hundreds of nanoseconds, which do not encode depth information [9, 11]. This can potentially lead to acquisition rates in the range of tens of megahertz. This rapid rate of imaging can potentially enable video-rate live feedback. Furthermore, this rate of imaging can be combined with adaptive optics to quickly acquire optical sections for the purposes of rapid 3D visualizations [119]. These advantages position

29

PARS to be a promising modality to achieve high-resolution reflection-mode video-rate live feedback as well as rapid 3D imaging for clinical applications.

To this end, taking advantage of the all-optical design, we present a system capable of live real-time imaging and 3D visualizations. Employing an integrated two-axis optical scanning head with a simple interpolation scheme based on nearest neighbors, we demonstrated a sustained frame rate of up to 2.5 Hz with a 600 kHz pulse repetition rate laser and a field of view of 167 µm × 167 µm. A resolution of 1.2 µm was measured from the live feed, which we believe is the highest reported for a live feedback reflection-mode architecture. The system's performance is demonstrated with carbon fiber phantoms as well as *in-vivo* imaging. The first results of 3D imaging with PARS are also shown. We benchmark the performance of 3D reconstruction with phantoms and demonstrate its efficacy by visualizing microvasculature structures in 3D *in-vivo*.

4.1 Methods

In this section we describe the experimental apparatus, acquisition and interpolation techniques for real-time imaging. The system resolution and SNR is also characterized. Lastly, the laser fluence levels are computed and compared against American National Standards Institute (ANSI)'s maximum permissible limits.

4.1.1 Optical System

Figure 4.1 illustrates the experimental apparatus. The optical system presented in this chapter is optimized for real-time imaging and includes a set of scanning mirrors. The inclusion of the scanning optics is the only major difference from a standard PARS setup as previously shown in figure 2.4. As PARS is a laser scanning microscopy, it mandates a fast pulse repetition rate laser. The ultraviolet laser introduced in Chapter 3 has a pulse repetition rate of 20 kHz and is thus not suitable for rapid acquisitions. Instead, the 532 nm 600 kHz pulse repetition rate laser is used to demonstrate real-time imaging. The image acquisition and reconstruction methods described in this chapter are independent of the laser type, allowing for real-time histology-like imaging when a significantly faster ultraviolet is available.

4.1.2 Image Acquisition

Microscopes that rely on point acquisitions require the desired field of view to be well sampled for effectual image reconstruction. To this end, the scanning mirrors are arranged orthogonally and allow the co-focused excitation and detection beam to be steered at any location in the field of view. The mirrors are driven using a ramp waveform from a function generator. The amplitude and frequency of the waveforms determine the field of view and the rate of the mirror swing. The ramp waveforms provide a constant velocity and allow a consistent step size between point acquisitions. The driving frequency of the mirror depends upon the laser repetition rate and the desired number of point acquisitions per frame. For example, when the excitation laser repeats at 600 kHz, the fast axis is driven at 900 Hz and the slow axis at 1.8 Hz. Additional details of the hardware and methods are provided in section 3.2.2. This acquisition method is used for real-time imaging as well as for capturing a set of 2D slices at different depths for 3D volumetric reconstruction. Between each 2D slice, the target is moved at a prescribed amount vertically using a mechanical stage.

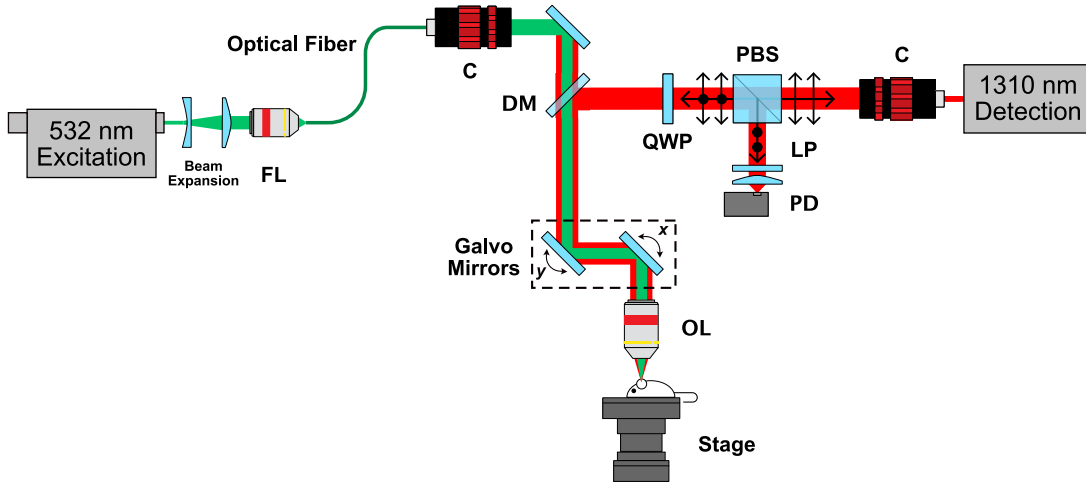
Figure 4.1: Experimental Setup. Component labels are defined as (FL) fiber launch, (C) collimator, (DM) dichroic mirror, (OL) objective-lens, (QWP) quarter wave-plate, (PBS) polarized beam splitter, (LP) long pass filter, (PD) photodiode.

31
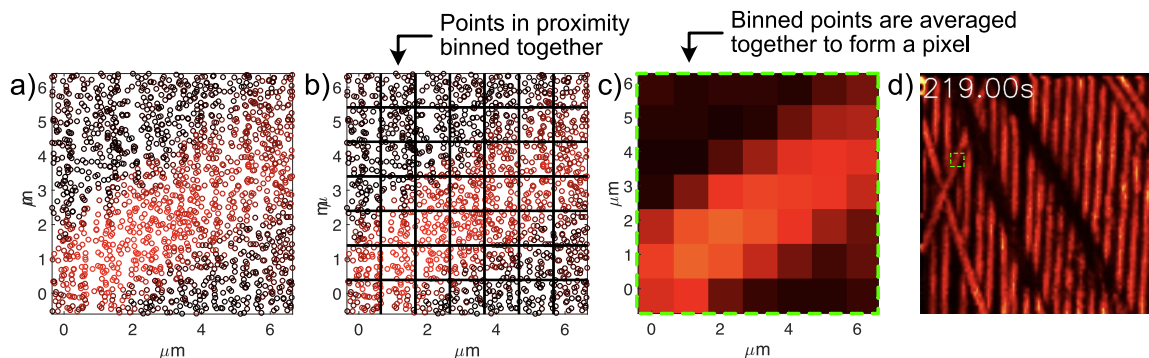
Figure 4.2: An illustration of the steps involved in the interpolation. **a)** Raw scatter data **b)** Grid illustrates binning size. Points inside a box are rounded off to its center **c)** Close up of an interpolated image. Corresponding pixel location is assigned the average amplitude of the binned points. **d)** Zoomed out final image.

4.1.3 Image Formation

Providing a live display requires transferring, processing and interpolating the streamed data in real-time. The digitizer streams the PA signal and the two mirror position signals in the form of a 16-bit interlaced array. This array is deinterlaced to separate the three individual signals into independent arrays. For each point acquisition, the mirror signals are averaged reducing the noise due to the digitizer or electrical interference. Assuming the noise is random and not correlated, the averaging reduces the noise by the square root of the number of array elements [120, 121]. For example, if the array length is 64, the noise is reduced by eight times. The resulting averaged arrays are stored as 64-bit floats to match the native architecture of the imaging computer. The PARS time-domain signals are converted to the frequency domain via the fast Fourier transform and passed through a low pass filter. This filter attenuates the noise from the digitizer, photodiode, or the detection source present in the signal. The resulting signal is then transformed back to the time domain. The amplitude of each filtered time-domain signal is then computed. This processing results in each point acquisition having an intensity and x,y spatial coordinate specifying where in field of view it was captured. These points lack a regular grid-like structure and must be interpolated to form an image. Figure 4.2a shows the scatter data over a small field of view. The electronic noise floor of the system was measured using the digitizer by blocking the optical inputs of the photodiode. The noise floor was measured to be approximately 20 mV peak to peak. The digitizer provides 14-bit analog to digital conversion for each analog input. With a 5V input waveform, the least significant bit equates to approximately 300 µV, which is far lower than the measured noise floor of 20

32

mV. This implies that the mirror positional signals likely do not represent 14-bits precision. Although the mirror positions are averaged, the noise reduction is not sufficient to represent 14-bits of precision. For example, if a recording segment had a length of 128 segments, the noise would be reduced by approximately eleven times [120, 121]. However, the noise floor is approximately sixty times higher than the least significant bit. Recognizing this, the averaged mirror positions are converted to integers from 64-bit floats. This conversion has the effect of binning points that are close together, as illustrated in Figure 4.2b.

For example, coordinates such as (34.3,10.5) and (34.7,10.2) are rounded to (34,10). This method, therefore, does not require a computationally expensive search to determine a given point's nearest neighbors, saving considerable execution time. The interpolation begins by declaring a zeroed out 2D array for the final interpolated image. Subsequently, for each coordinate, the corresponding single strength is looked up from the internal amplitude array and added to the appropriate pixel in the final image. The coordinate values from the discretized positional arrays are used as the indices for the interpolated image. Since the discretization process results in multiple points being binned together, multiple amplitudes are added together in the final image and averaged together to enhance the SNR (Figure 4.2c and 4.2d). Nonetheless, this interpolation method assumes that each pixel is large enough that it would contain multiple samples. If a pixel does not contain samples, the pixel value remains at zero and appear as black pixels in the interpolated image. As a final step, the image is iterated over and pixels which have a value of zero are assigned the average of the surrounding neighbors towards the left, right, top, and bottom of the pixel in question. The same algorithm is utilized for reconstructing each slice in a 3D volume. Once all the levels in a 3D volume have been reconstructed, we render the final 3D volume using ImageJ's ClearVolume plugin [122].

4.1.4   System Characterization

A point spread function is described as the response of an optical system to a point source [123, 124, 125, 126]. It is effectively how an imaging system views (or blurs) a point. The point spread response encodes the spatial resolution of an imaging system in horizontal and vertical dimensions [124, 125]. Experimental measurement of the point spread function requires imaging targets with a size less than the diffraction limited spot size (approximately 880 nm) [126, 124]. Such small targets will typically occupy only a few pixels in the final image and make it difficult to measure the point spread function reliably [126]. As an alternative, the resolution of an optical system can be characterized by measuring its response to a very thin line resulting in a line spread function. The line spread function effectively describes the resolution of a system in one dimension [124]. This response is called the line
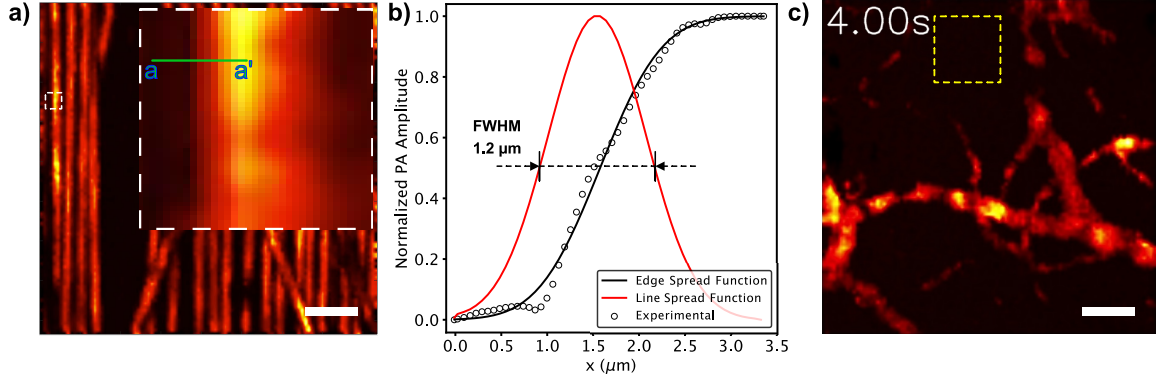
Figure 4.3: Images for resolution and SNR characterization. **a)** Carbon fibers used to measure resolution. Scale bar 25 µm **b)** resolution measurement with line spread function **c)** *in-vivo* image of microvasculature structure in mouse ear used for SNR measurement. Yellow box is region where noise was measured. Scale bar 25 µm.

spread function. Unfortunately, finding targets that resemble a line and have a sufficiently thin width (less the diameter of the focal spot size) is also not trivial. However, the line spread function is the first derivative of an edge spread function [124]. The edge spread function measures how the imaging system blurs an edge. By first measuring the edge spread function and subsequently computing the first difference, we can arrive at the line spread function which reliably describes the resolution of the system in one direction [125]. If we further assume that the laser spot size has a Gaussian shape, the line spread function effectively describes the resolution in both dimensions [124].

Here, the edges of carbon fibers were imaged to characterize the lateral resolution of the imaging system (Fig 4.3a). The edge profile was measured across the green a – a' line and an edge spread function was fitted. The first derivative of this edge spread function is computed, resulting in a line spread function. The full width at half maximum (FWHM) of this line spread function is considered as the lateral resolution. This revealed a resolution of 1.2 µm, more than sufficient to resolve capillaries and even cell nuclei. Figure 4.3c shows an image of a microvasculature structure captured in a mouse ear used to characterize the SNR. Next, the system's peak and mean SNR is measured as follows:

$$SNR_{peak} = \frac{max\{|s_{ij}|\}}{\sigma_n}$$

$$SNR_{mean} = \frac{\langle|s_{ij}|\rangle > t}{\sigma_n}$$

34

where σ_n is the standard deviation of a region lacking signal (yellow box in Fig 4.3c), where s_{ij} is the signal in the image, $\langle\rangle$ represents a mean, and t is some threshold value used to denote signal level. In the cause of microvasculature images, t is chosen such that only signals comprising of blood vessels are considered. This yielded a peak SNR of 62 dB and a mean SNR of 44 dB *in-vivo*. The 14-bit precision offered by the digitizer translates to a theoretical dynamic range of 84 dB. However, the photodiode's noise equivalent power of $\frac{5.2pW}{\sqrt{Hz}}$ limits the overall dynamic range of the system to approximately 59 dB. Compared to the peak SNR of 62 dB, it becomes evident that the filtering and averaging improve the effective SNR of the system significantly.

4.1.5   Excitation beam Laser Safety

The mouse-ear has numerous blood vessels 70 – 100 µm below the skin [127]. Assuming a focal spot diameter of 1 µm and the optical focus depth to be 70 µm, the diameter of the laser spot at the surface of the mouse ear can be calculated to be 22 µm. The pulse energy of the excitation laser was measured to be 45 nJ. This yields a fluence of 10 mJ/cm^2, which is considerably below the skin exposure limit of 20 mJ/cm^2 set by ANSI. [128].

4.1.6   Detection beam Laser Safety

The detection laser was set to a power of 5 mW and areas as large as 500 µm $\times$ 500 µm are scanned in this work. This results in irradiance of 2.4 W/cm^2. For a continuous wave laser with a wavelength of 1310 nm and an exposure time between 100 ns and 10 s, the maximum exposure limit (MPE) on the skin is limited to an energy density of $MPE = 1.1C_A t^{0.25}$, where C_A is defined as the correction factor and is defined as 5 for a wavelength of 1310 nm (25). The demonstrated *in-vivo* imaging had an exposure time of 1 s. The average power limit set by ANSI is calculated as $MPE_{avg} = \frac{MPE}{t}$ and equates to 5.5 W/cm^2. The detection laser is, therefore, operating at half the ANSI limit.

4.1.7   Animal preparation for *in-vivo* imaging

All animal experiments were approved by the University of Waterloo Animal Care Facility and were carried out in accordance with the University of Waterloo ethics committee. A nude SKH1-Elite Charles River mouse was anesthetized with 5% isoflurane. The anesthesia was maintained with 1% isoflurane during the *in-vivo* imaging. A heating pad was placed under the mouse to maintain body temperature.

4.2 Results

Carbon fibers were used as phantom targets to benchmark the proposed method's performance. Multiple layers of carbon fibers were placed on top of a glass slide and placed underneath the microscope's objective. Figure 4.4a shows select frames from a live video where the fibers are panned and optically sectioned. The scanning mirrors were driven at 1.8 Hz and 900 Hz. A total of 200,000 A-scans were captured in a field of view of 167 µm × 167 µm resulting in an average step size of 400 nm. The mechanical stages are used to translate the carbon fibers underneath the objective, as shown in the first two frames. The depth stage is then moved to focus onto a second layer of carbon-fibers underneath. With an A-scan count of 200,000 and a pulse repetition rate of 600 kHz, the acquisition time was approximately 300 ms per frame. The image reconstruction takes approximately 100 ms on a 2.7 GHz Intel Core i7 processor resulting in a real-time visualization frame rate of nearly 2.5 Hz.
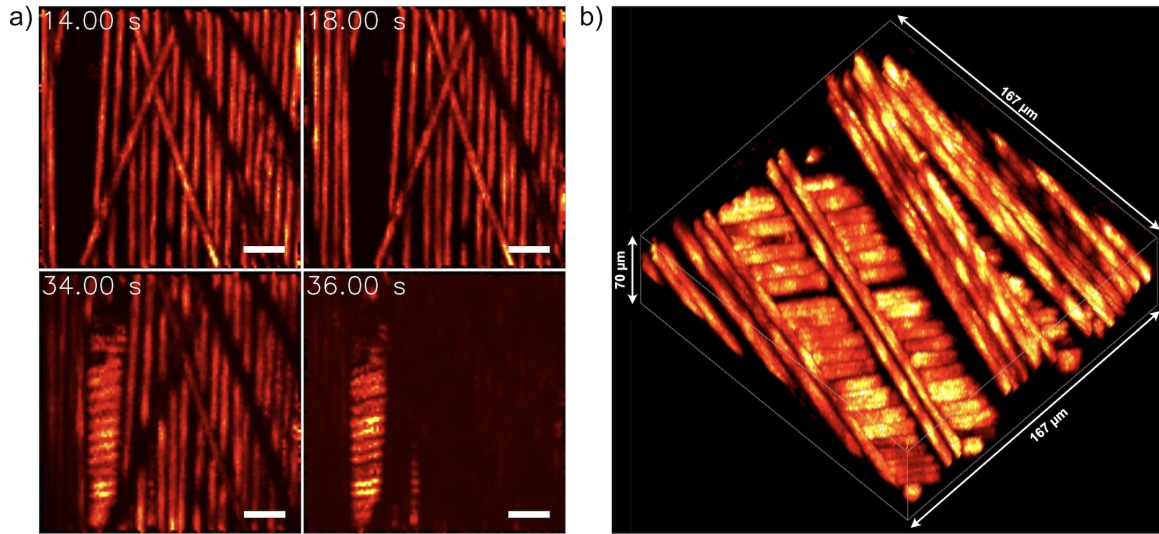
Figure 4.4: a) Live display of carbon fibre networks Individual frames extracted from a screen capture of the live display. Time stamp is annotated in the top left corner of each frame. Scale bar: 25 µm **b)** 3D reconstruction using the same method. Field of view is 167 × 167 µm^2, total depth 70 µm.

Figure 4.4b shows the 3D capabilities of the system. The depth stage was utilized to move the sample perpendicularly after a 2D acquisition was completed. A total of 14 2D frames were captured with a vertical step size of 5 µm between them. The 3D view shows the multiple layers of carbon fibers in high fidelity. The field of view was set to 167 µm × 167 µm with a total depth of 70 µm.
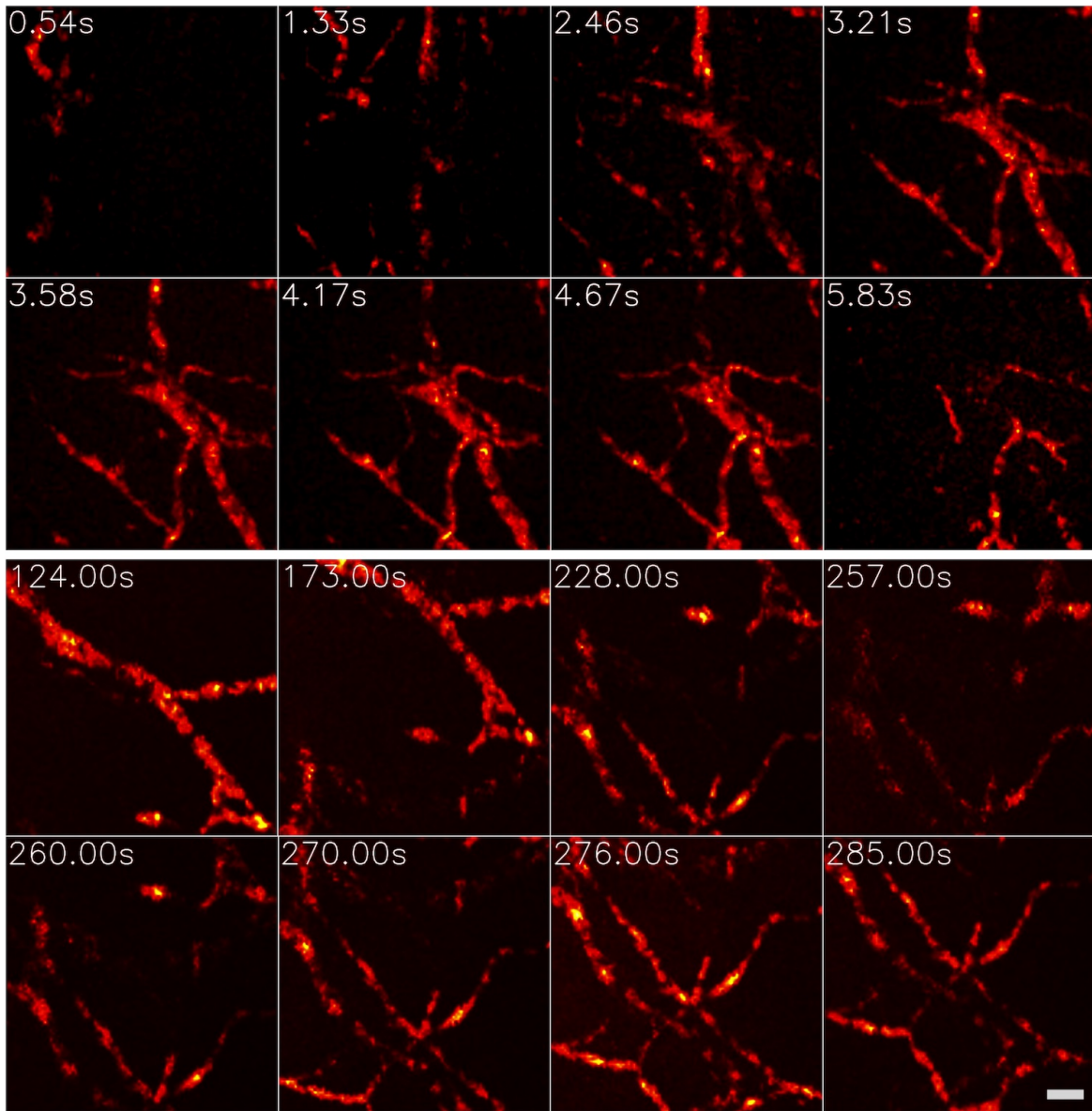
Figure 4.5: *in-vivo* live stream of microvasculature structure in a mouse ear. Multiple layers are visualized by first changing the depth of the mouse ear. Subsequently, different locations are visualized by panning the mouse using a pair of mechanical stages. Field of view 183×183 µm². The timestamp can be seen in the top left corner. Scale bar 25 µm.

The proposed method's efficacy is demonstrated with *in-vivo* imaging of mouse ears.

Figure 4.5 shows select snapshots from a live video of microvasculature structure within a mouse ear. The figure illustrates the microvasculature coming into focus as different planes within the ear are visualized. The field of view is then panned using the 2D mechanical stages to visualize different regions in the mouse ear. To limit the heat deposition on the mouse ear, we reduced the laser repetition rate to 50 KHz and acquired 50,000 A-scans per frame to achieve a real-time visualization frame of approximately 1 Hz. We emphasize that these results are from a live video and not from a post-acquisition reconstruction. The field of view was set to 183 µm × 183 µm and the average step size was 800 nm.
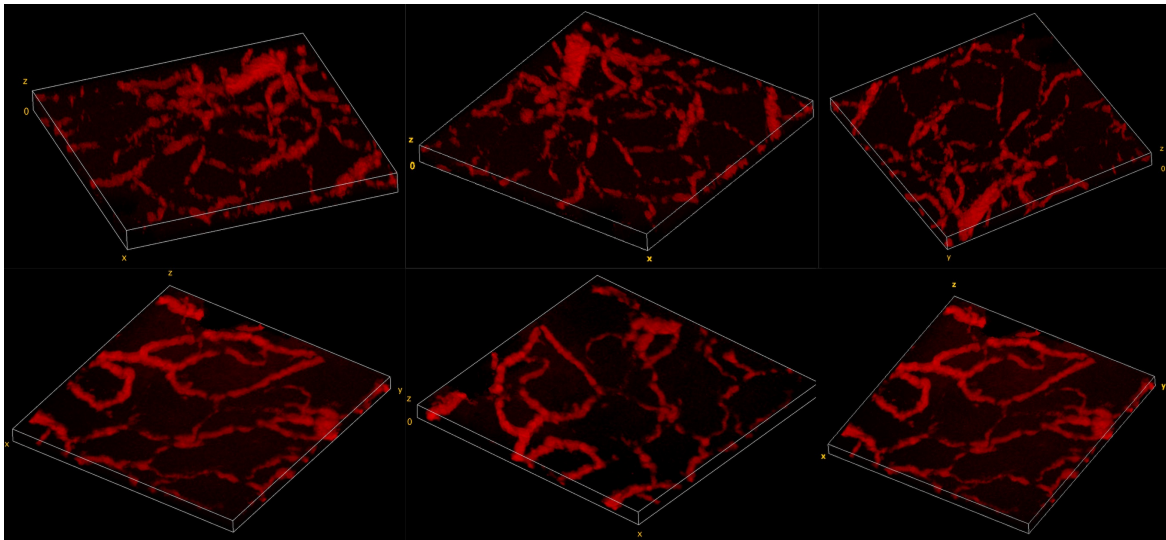
Figure 4.6: 3D visualization of microvasculature structure in mouse ear. Field of view of 500 µm × 500 µm.

Figure 4.6 demonstrates PARS's ability to capture 3D volumes. Two different locations on a mouse ear were captured *in-vivo*. These results represent the first 3D images captured with a non-contact label-free reflection-mode method. Similar to the 3D phantom image, the depth stage was utilized to move the mouse in a perpendicular direction. A total of 17 frames were acquired with an axial step size of 3.5 µm. This captured a total depth of 60 µm. The total field of view was set to 500 µm × 500 µm for both 3D volumes.

4.2.1 Comparison with Delaunay triangulation

In this section we compare the quality and speed between the nearest neighbor interpolation to the Delaunay triangulation based interpolation initially discussed in section 3.2.3. A

custom MATLAB script was written to compare the execution time of the two techniques with the same parameters. The number of samples was 100,000 spread over 160 μm × 160 μm and the pixel size was set to approximately 2 μm. All post-processing was turned off. The benchmarking computer had 16 GB of memory and a 2.7 GHz Intel Core i7.

As we previously discussed in section 3.2.3, Delaunay triangulation can be divided into two major steps, the triangulation and the interpolation. MATLAB's built-in implementation allows the user to access both functions independently and repeatedly interpolate from an initial triangulation, saving considerable execution. This is extremely useful if the exact same set of points is acquired for each acquisition. Unfortunately, this is not the case for our setup and perhaps most real-world point by point microscopes. The noise ensures the target is sampled at different locations for each capture, effectively mandating triangulation for every set of point acquisitions captured. The MATLAB script was therefore written to triangulate the point acquisitions during each of the hundred benchmarking runs and subsequently interpolate. It is important to note only the execution time of the actual image formation (and relevant steps) was measured. File reading, display or other steps were not accounted for. All post-processing was turned off. For the nearest neighbor approach, post-reconstruction pixel filling was still performed (previously described in section 4.1.3). With this configuration, Delaunay triangulation required an average of 390 ms whereas nearest neighbor was significantly more efficient and required 2.3 ms to finish. The Delaunay triangulation is slow primarily due to the triangulation step. If we modify the script to triangulate only once and interpolate a hundred times, the average execution time drops to 66 ms. The 66 ms execution time is a significant improvement but still quite slow compared to the nearest neighbor approach introduced in this chapter.

Figure 4.7 shows the result from both techniques. The images are displayed in logarithmic scale to exaggerate the contrast. Both images are displayed on the same color axis (-5 to -45 dB). In the Delaunay interpolation a rougher background can be observed compared to the nearest neighbor interpolation. The mean SNR with Delaunay interpolation and nearest neighbor was found to be 22 dB and 35 dB, respectively. The proposed method reports a higher SNR due to the averaging of all the samples contained within a pixel. However, the nearest neighbor approach shows a number of 'dead' pixels. The dead locations in the image are due to pixels not containing any samples. Although, these locations are filled after the initial image reconstruction the deterioration in image quality is still visible in the image. The effect of pixel size on both interpolations is investigated in figure 4.8. As the pixel size becomes smaller, the nearest neighbor approach begins to break down due to the assumption of having samples within the pixel locations to effectively interpolate. Delaunay triangulation, in comparison, is able to interpolate even with pixel sizes as small as 200 nm.
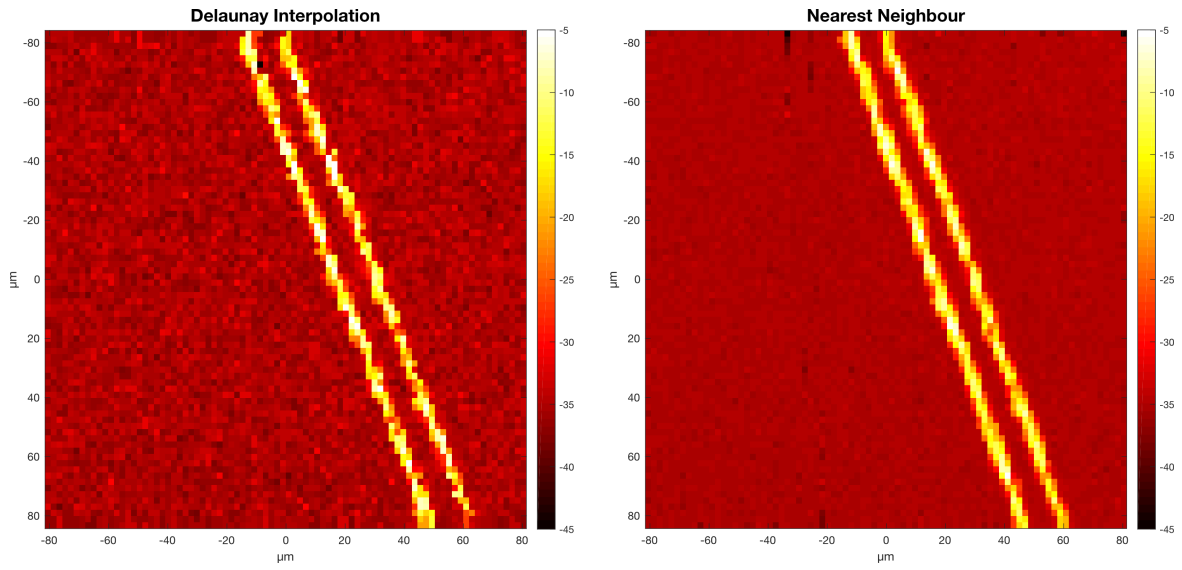
Figure 4.7: Comparison between Delaunay triangulation and proposed method. Images are displayed in logarithmic scale.
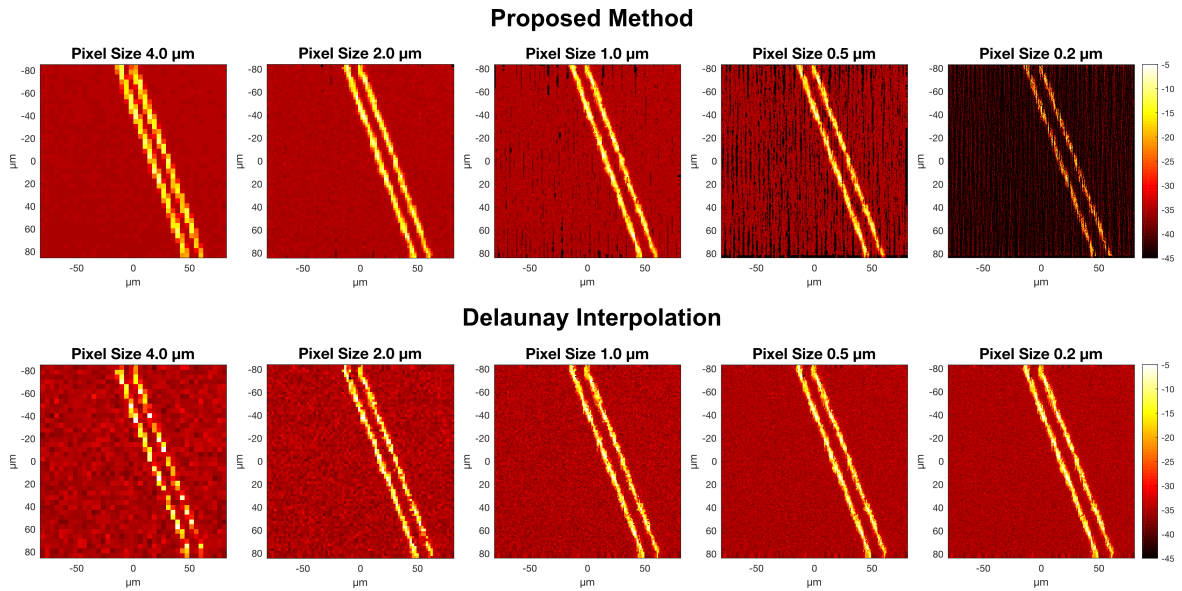
Figure 4.8: The effect of pixel size on the proposed method and Delaunay triangulation. Images are displayed in logarithmic scale.

Step	Execution Time (ms)	Percentage of Total Time
Mirror Waveform Averaging	10.9	13.1 %
Fast Fourier transform	17.3	20.7 %
Low Pass Filtering (in Fourier domain)	25.6	30.8 %
Inverse fast Fourier transform	18.7	22.5 %
Scale Signal Arrays from ADC Count to µm	0.8	1.0 %
Discretization	0.94	1.1 %
Interpolation	0.64	0.7 %
Total Time	83.3	100.0 %

Table 4.1: Execution times of all the major steps involved in the image reconstruction.

4.2.2 Performance Breakdown

In this section we provide a brief discussion on execution time for all the major steps in the image reconstruction process. The real-time reconstruction method is intended to be used in conjunction with a streaming data acquisition card. However, for the sake of testing consistency, these benchmarks were conducted by reading a raw image file. The time taken to read the image file was not measured. Table 4.1 lists the measured steps and the execution times. By far the most computational process is the fast Fourier transform, filtering and the inverse fast Fourier transform. These three steps take up to 74% of the total processing time. The Fourier transform is implemented via the *Fastest Fourier Transform In The West* library [129]. The interpolation by itself takes only 0.7%. The numbers below are a result of running the benchmarking program one hundred times and averaging the result for a 100,000 sample count image. Unlike section 4.2.1 where MATLAB was used to compare Delaunay triangulation with the proposed method, this section used the `C++` codebase to mimic an actual real-time imaging application as much possible.

4.3 Discussion

The proposed method demonstrates several benefits over previous reports of real-time PA imaging systems [111, 112, 113, 114, 115, 116, 117, 118]. (1) Analogous to OR-PAM's requirement of a confocal geometry between the excitation and the resulting acoustic waves, PARS is reliant on a strong confocal arrangement between the excitation and the detection beam. However, achieving a strong confocal arrangement between two optical beams is significantly simpler and does not require the use of any components between the target and the objective lens. This advantage allows PARS to employ high NA objective lenses to achieve a resolution of 1.2 µm, the highest reported by a real-time reflection-mode PA

imaging system. (2) A standard x-y galvanometer scanner steers the optical beams simultaneously and maintains a strong confocal geometry between the two leading to a system with appropriate sensitivity for recovering blood vessels in vivo. This allows real-time imaging with a mean and peak SNR of 44 dB and 62 dB, respectively, with a laser fluence of 10 mJ/cm^2. The SNR measurements exceed previous reports of PARS systems with comparable values for laser fluence [9, 10]. (3) Employing a computationally inexpensive reconstruction technique that bins points in proximity and averages the amplitudes, we demonstrate a live video feed that enhances the high SNR afforded by the optical system and sustains frame rates up to 2.5 Hz.

We also demonstrate PARS's ability to capture 3D volumes *in-vivo*. These results represent the first reports of 3D imaging with PARS. Presently, these volumes are captured by acquiring multiple 2D layers at various depths by moving the surface of the sample perpendicular to the optical axis using a mechanical stage. This process can be sped up considerably by using a laser with a faster repetition rate and employing adaptive optics to move the focal spot instead of moving the sample [119]. For example, it would take approximately 25 ms to acquire 50,000 A-scans per layer with a 2 MHz repetition rate laser. Assuming a total of 14 slices are required, the total acquisition time would be 350 ms. This can enable high-speed 3D visualizations, potentially in real-time. Alternatively, architectures like coherence-gated PARS can be explored to provide depth-resolved PA signals for potentially even faster 3D imaging [130].

To render live video, the proposed method relies on a computationally lightweight interpolation scheme. In most nearest neighbor based interpolation schemes, the process of searching for a given point's neighbors dominates the interpolation time [131, 132, 133]. To this end, several data structures have been explored to speed up a nearest neighbor search. The proposed method is able to find a given point's nearest neighbors by rounding off the positional arrays. This is effectual because the positional information of each A-scan likely does not have 14-bits of precision due to a small amount of measurement noise associated with each digitization. High-SNR interpolation is realized by averaging the binned scatter points. The key advantage of this approach is that allows the positional arrays to be treated as indexing arrays for the final image. This enables direct access of the pixel locations in constant time (time complexity of *O(1)*) [134] rather than a computationally expensive nearest neighbor search. This results in rapid image reconstruction from the scatter data with high SNR and contrast suitable for a high-quality live video stream. The most computationally expensive task in the image reconstruction is the low pass filtering which, typically, accounts for 30% of the total image reconstruction time (see section 4.2.2). However, in the future, this step, along with other parallelizable code, can be executed on a graphics processing unit which can potentially reduce the execution time even further.

The overall rendering time for the live video is a sum of the acquisition time and the image reconstruction time. Since the digitizer is configured to stream the acquisitions directly to system memory, the time taken to transfer the data is effectively zero. This makes the acquisition time entirely dependent on the laser repetition rate and the number of A-scans desired per frame. The image reconstruction takes approximately 100 ms per 100,000 A-scans to fully render a scene and is usually not the limiting factor in terms of frame rate. Instead, it was found that the primary limiting factor for the frame rate and the field of view were the scanning mirrors. The mirrors have a maximum swing rate of 1 kHz for angles smaller than 0.2°. This angle translates to approximately 120 µm × 120 µm in terms of field of view with the current objective lens. As mentioned, the phantom studies captured 200,000 A-scans per frame with a repetition rate of 600 kHz. The mirrors were driven at 1.8 and 900 Hz, which is close to their maximum specification. Although the shorter acquisition and reconstruction times can be realized by reducing the point count per frame, the mirror swing rate would need to be increased as well. For example, from our *in-vivo* results, it can be observed that even 50,000 A-scans per frame provide remarkable contrast and resolution, resolving capillaries as small as 6 µm. However, capturing 50,000 A-scans per frame at a repetition rate of 600 kHz would require the fast axis to swing at a rate of 3.6 kHz, which is far higher than their specification. Future work can aim to increase the imaging frame rate by using faster scanning optics, optimizing scanning patterns, and employing higher pulse repetition rate lasers.

Chapter 5

All-optical Reflection-mode Microscopic Histology of Unstained Human Tissues

Building upon chapters 2, 3, and 4, we arrive at discussing a PARS system designed for histology-like imaging. The system is designed with an ultraviolet excitation laser to target the optical absorption peak of DNA. With this, the endogenous contrast of cell nuclei and bulk tissue structure can be recovered. Through the PARS effect, we present the first non-contact label-free reflection-mode histology-like images in a variety of human tissues. This particular study investigated imaging in the human breast, gastrointestinal, and skin in unstained FFPE slides as well as FFPE tissue blocks. FFPE tissue blocks serve as an analog to *in-situ* imaging due to their thickness. These images are qualitatively compared against adjacent H&E slides prepared through standard tissue processing. To evaluate the diagnostic potential of the approach, we also present a quantitative comparison with several nuclear morphology metrics to conventional H&E prepared slides.

5.1   Methods

In this section we provide a description of the optical system for imaging tissue morphology and sample preparation method for FFPE tissue blocks, unstained slides as well as standard H&E slides. The system resolution and SNR with the 266 nm excitation is also characterized. The image formation method employs mosaics to image large field of

views. A description of mosaic acquisition and reconstruction was provided was previously provided in section 3.2.2 and 3.2.3.

5.1.1 Experimental Apparatus

The optical system used in this chapter is similar to the one introduced in Chapter 3 (section 3.2.1). This chapter investigates the possibility of recovering nuclear morphology of the tissue samples. The 266 nm wavelength of the pulsed excitation primarily targets a DNA optical absorption peak. The 532 nm excitation path and the corresponding dichroic mirror is thus removed from the optical system. The elimination of the dichroic mirror results in improved light transmission of the 1310 nm detection light. This simplified system is shown in figure 5.1.

Upon absorption of a 266 nm pulse, thermoelastic expansion within the cell nuclei creates large initial photoacoustic pressures. These pressures can modulate the local optical properties through the elasto-optic effect. This creates a perturbed optical scattering profile seen by the detection beam. If the cell nuclei are considered to be an optically scattering particle with the cytoplasm of the cell, then these elasto-optic modulations modify these scattering properties. This scattering perturbation can then be observed with the probe beam as a rapidly changing back-scattered intensity coincident with the excitation spot. Although the elasto-optic effect itself produces a relatively small change in the optical properties (such as the permeability and permittivity) this effect is amplified by the pre-existing scattering profile which exists between the cell nuclei and cytoplasm. Additional background is provided in section 2.7.
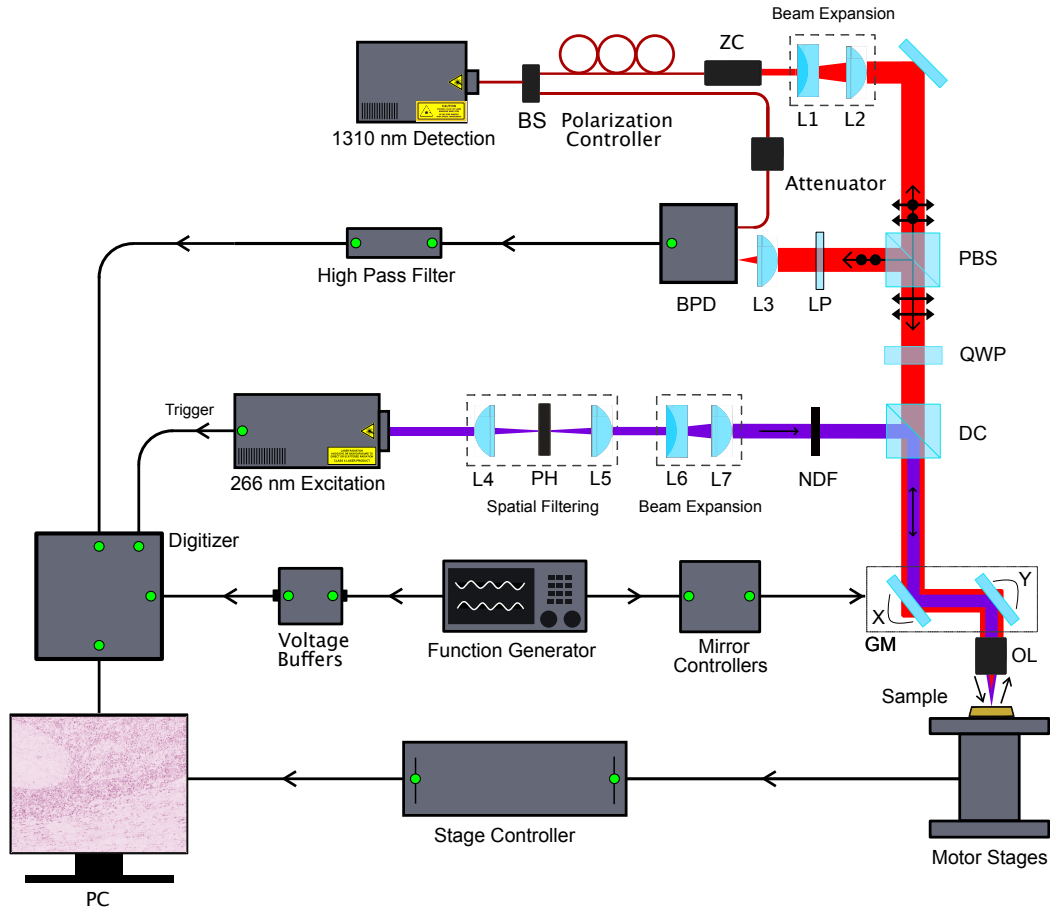
Figure 5.1: Schematic of the PARS apparatus. Component labels are defined as: beam splitter (BS), zoom collimator (ZC) long-pass filter (LP), polarizing beam splitter (PBS), quarter-wave plate (QWP), dichroic mirror (DC), balanced photodiode (BPD), pinhole (PH), neutral density filter (NDF), galvanometer mirrors (GM), objective lens (OL). The 266 nm laser (SNU-20F-10x, Teem Photonics) was spatially filtered by two lenses (LA4052-UV and LA4380-UV, Thorlabs Inc.) and a 25 μm pinhole (P25C, Thorlabs Inc.). The beam was then expanded using a fixed magnification beam expander (BE05-266, Thorlabs Inc.). This was combined with the detection path which uses a 1310 nm continuous-wave superluminescent diode (S5FC1018P. Thorlabs Inc.) as a source. The 1310 nm beam was passed through a fiber polarization controller (FPC562, Thorlabs Inc.) and then collimated (RC04APC-P01, Thorlabs Inc.). The collimated interrogation beam was then expanded using a variable beam expander (BE02-05-C, Thorlabs Inc.). The polarizing beam splitter (CCM1-PBS254, Thorlabs Inc.) splits the beam based on its polarization state. The horizontally polarized light is converted to circularly polarized light using a zero-order quarter-wave plate (WPQ10M-1310, Thorlabs Inc.). A dichroic mirror (HBSY234, Thorlabs Inc.) is used to combine the detection beam and the excitation beam. The excitation and detection beams were co-aligned into a 2D galvanometer scanning mirror system (GVS412, Thorlabs Inc.). The beams were then co-focused using a 0.3 numerical-aperture reflective objective lens (LMM-15X-UVV, Thorlabs Inc.). The back-reflected interrogation beam was converted from circular to horizontal polarization by the quarter waveplate and then passes back through the polarizing beam splitter where it is directed to a 75-MHz bandwidth InGaS balanced photodiode (PDB425C-AC, Thorlabs Inc.) for detection. The long-pass filter is chosen to block any back-reflected excitation light.
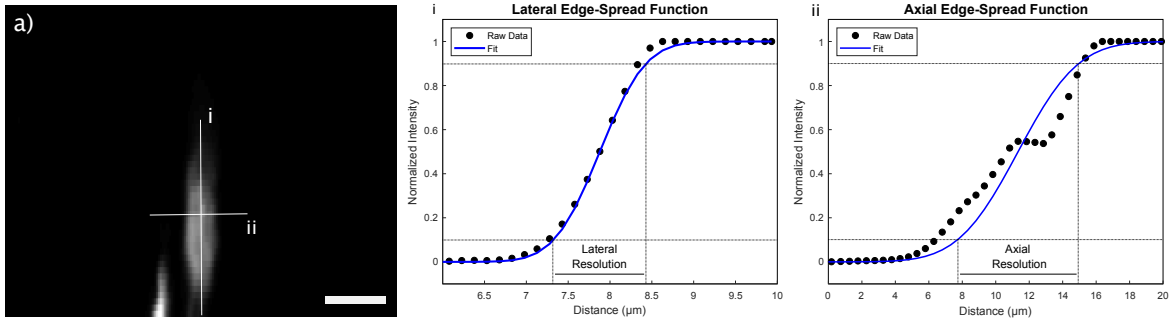
Figure 5.2: Resolution study from a 7 µm diameter carbon fiber in water. **(a)** A B-Scan of the carbon fiber is shown. The two right graphs show how the lateral and axial resolutions are extracted from edge spread functions of the carbon fiber **(i)** and **(ii)** respectively. Scale bar 10 µm.

5.1.2 Resolutions study

The system resolution was characterized against a B-scan of a carbon fiber. The lateral and axial resolution is measured by fitting raw data of the B-scan to edge spread functions. The resolution is defined as the width from 10% to 90% of this function as illustrated in Fig. 5.2. The lateral resolution of the system is found to be 1.2 µm whereas the axial resolution is measured at 7.3 µm. This resolution can be compared to commercial bright-field microscopes used in pathology which generally operate with objectives providing 5x to 40x magnifications yielding submicron resolutions.

5.1.3 Sample preparation

Human breast, tonsil, gastrointestinal and pancreatic tissue samples were obtained under a protocol approved by Research Ethics Board of Alberta (Protocol ID: HREBA.CC-18-0277) and University of Waterloo Health Research Ethics Committee (Humans: #40275 Photoacoustic Remote Sensing (PARS) Microscopy of Surgical Resection, Needle Biopsy, and Pathology Specimens). All experiments were performed in accordance with the relevant guidelines and regulations. Tissue specimens were attained from anonymous patient donors with the help of clinical collaborators in the Cross Cancer Institute (Edmonton, Alberta, Canada). The ethics committees waived the requirement for patient consent on the condition that samples were archival tissue no longer required for diagnostic purposes, and that no patient identifiers were provided to the researchers. The breast tissue specimens were obtained from fresh mastectomy resections and immediately placed in formaldehyde to allow for proper tissue fixation. The pancreatic tissue and tonsil resection tissue were obtained from stored samples that were prepared in a similar fashion.

To enable comparisons between PARS images and H&E stained images, adjacent sections were cut from the same FFPE tissue block. As they are not the same exact tissue sample, some minor differences in appearance do exist. The method of preparation for the tissue blocks, unstained slides, and H&E slides follows.

5.1.4 Tissue blocks

After remaining submersed in formaldehyde for at least 48 hours, the tissues were then processed as usual: dehydration, cleared with xylene, and infiltrated with hot paraffin wax. Thereafter the tissue was embedded in paraffin wax and mounted on cassettes. Once cooled to room temperature, the FFPE blocks were finally created. This FFPE block could then be cut using a microtome. It was shaved down until the desired target tissue region was exposed. The gastrointestinal tissue was obtained from stored FFPE block samples that were initially prepared in a similar fashion.

5.1.5 Unstained slide preparation

4 µm thick tissue slices from the FFPE blocks were acquired and the resulting ribbons were placed in a warm water bath. The ribbons were then transferred to glass slides and baked at a temperature of 60°C for one hour in order to remove the excess paraffin and to ensure the specimen is affixed to the glass slide. The slides were not covered with coverslips or any other media.

5.1.6 H&E slide preparation

4 µm thick tissue slices from the FFPE blocks were acquired and the resulting ribbons were placed in a warm water bath. The ribbons were then transferred to glass slides and baked at a temperature of 60°C for 30 minutes. The baking ensures that the sample adheres to the glass slide. The slides were then stained with hematoxylin and eosin staining media before covering with mounting media and a coverslip. Once the mounting media was dry, the slides were considered ready to use.

5.2 Results

5.2.1 System Characterization

Results are acquired using the apparatus detailed in Fig. 5.1. In brief, a 266 nm nanosecond excitation pulse is used to excite photoacoustic pressures within the sample providing DNA contrast. These pressures are detected by monitoring the back-reflected intensity of a co-focused 1310 nm continuous-wave interrogation source. Targets include 7 µm diameter carbon fiber networks (Fig. 5.3a) and breast cancer tissue (invasive ductal carcinoma) (Fig. 5.3b). All images are acquired with endogenous contrast and without additional labels. All PARS images presented were acquired with a large working distance from the objective (24 mm) facilitating implementation both as a table-top device and as an *in-situ* tool where the working space is limited. With the current pulsed repetition rate of 20 kHz, small field of view (high resolution) acquisitions are acquired at a point density of 2 pixel/µm and at a rate of 1250/s. Resolution metrics are pulled from structural images by using edge spread functions across B-scans of 7 µm carbon fibers. The lateral resolution is found to be 1.2 µm while the axial resolution is measured at 7.3 µm. SNR values are computed using the method described in section 4.1.4. This yields a peak and mean SNR of $SNR_p = 58.5$ dB and $SNR_m = 42$ dB respectively in unstained tissue slides (Fig. 5.3b).
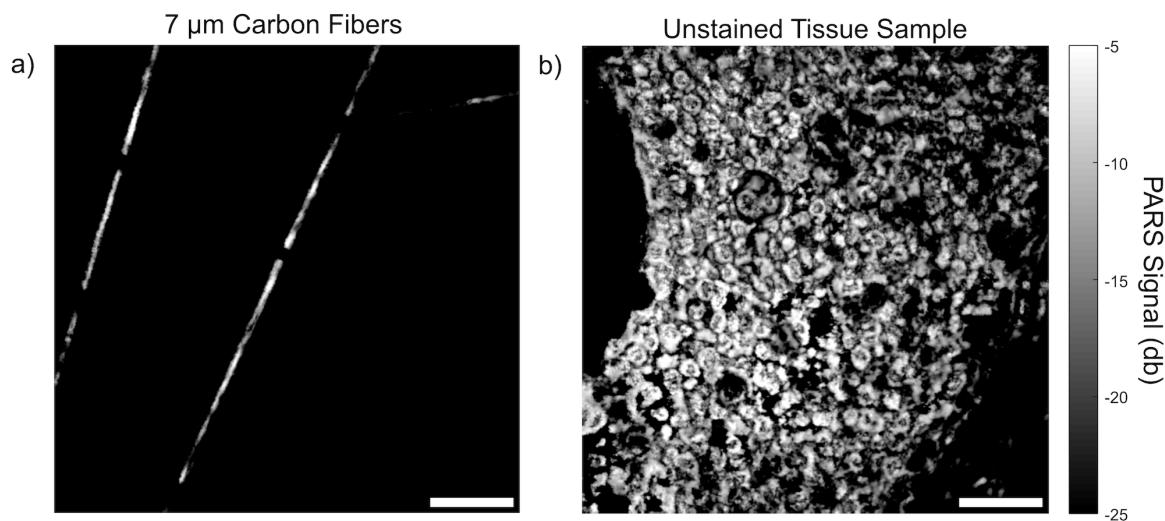

Figure 5.3: **(a)** PARS image of 7 µm carbon fibers. **(b)** PARS images of an unstained slide-mounted breast tissue sample. Scale bars for **(a,b)** are 50 µm.

5.2.2 Assessment of Human Tissue

Figure 5.4 compares the three samples types examined in this study. Two preparations are used for the PARS samples including unstained glass slide-mounted sections and FFPE blocks. Consecutive tissue sections of breast tissue were prepared as unstained FFPE blocks and unstained slide-mounted sections along with a conventional H&E preparation. To approximate the surface of bulk unprocessed tissue, the unstained slide-mounted samples are not protected by a coverslip. These tissue samples provide a uniform control target to avoid out-of-focus artifacts from optical sectioning. The FFPE blocks more closely approach *in-situ* targets in that they contain tissue which can only be captured en-face with a reflection-mode modality and provide a multilayered structure for volumetric acquisitions. These tissue samples are roughly 5 mm thick, are embedded in paraffin, and mounted on an opaque embedding cassette. In addition, the FFPE blocks have micron-scale surface irregularities similar to fresh tissue. The unstained samples are imaged using the PARS apparatus detailed in Fig. 5.1 whereas the H&E images are acquired using a standard conventional bright-field pathology microscope (Zeiss Axioscope 2 with Zeiss Axiocam HR). The performance of PARS in visualizing cellular-scale structures is compared to conventional H&E bright field microscopy using breast (Fig. 5.5), gastrointestinal (Fig. 5.6) and tonsil tissues (Fig. 5.7). Similar regions are imaged across all three sample types for direct comparison.

Figure 5.5a is a standard H&E stained image taken with a conventional bright-field microscope at a magnification of 5x. The unstained tissue slides were also imaged with a bright-field microscope for comparison (Fig. 5.5b). PARS images with false H&E colour map (Fig. 5.5c,e) is used to approximate a hematoxylin-like stain as seen in the H&E stained bright field images, and a greyscale logarithmic colour map (Fig. 5.5d,f) is used to highlight the PARS signal. In the false H&E colour map, darker pinks represent stronger PARS signals which are primarily attributed to higher DNA concentrations in these locations where the white indicates minimal PARS signal and a lack of DNA contrast. In the greyscale colour, map white represents stronger PARS signals where black is associated with weaker PARS signal. However, as the primary contrast mechanism is the DNA absorption peak, direct visualization of eosin-stained regions is not achieved.

Other examples of human tissue samples are shown in Figs 5.6 and 5.7 where the pancreas and tonsil tissues are presented. The brightfield images (Figs 5.6a, 5.7c) are captured at a magnification of 10x and 20x, respectively. Each is compared with a conventional H&E image of the consecutive layer. As well, Fig. 5.7a highlights the wide field of view (1 cm by 1 cm) imaging capabilities of the system. Additional acquisition details are provided in section 3.2.2.
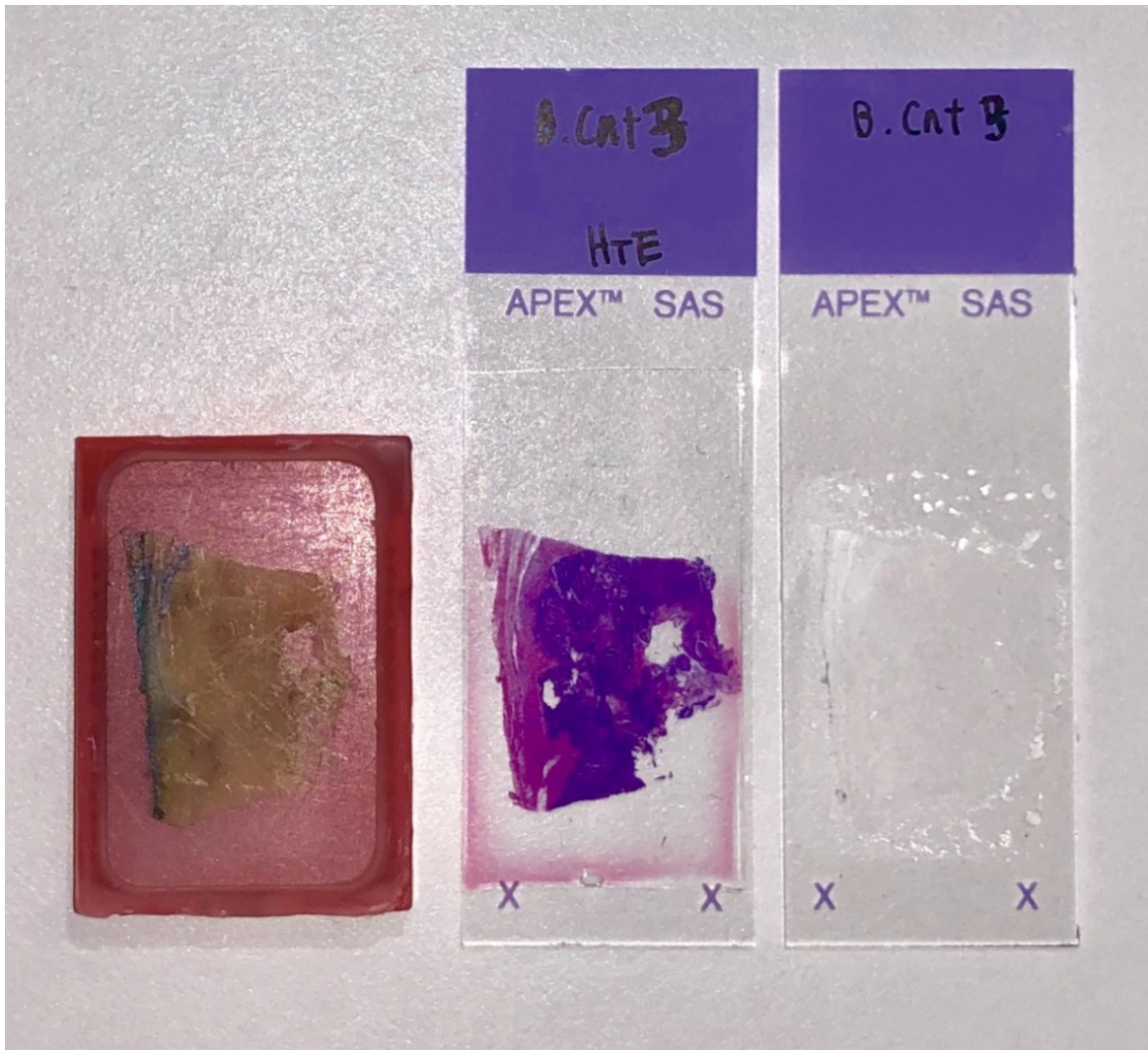
Figure 5.4: A comparison of the three sample types discussed in this work: **(left)** a formalin-fixed paraffin-embedded tissue block; **(middle)** a conventional H&E prepared slide and; **(right)** an unstained tissue slide.

5.2.3 Tissue volumes

Volumetric scans were performed on the FFPE blocks to image multiple cell layers (Fig. 5.8). Volumes are acquired by taking PARS images at 100 depth levels in the sample at 500 nm steps. For the volume shown in Fig. 5.8 the total scan time was around 33 minutes giving an acquisition rate of about 360 m^3/s. Several distinct cellular layers are recovered at
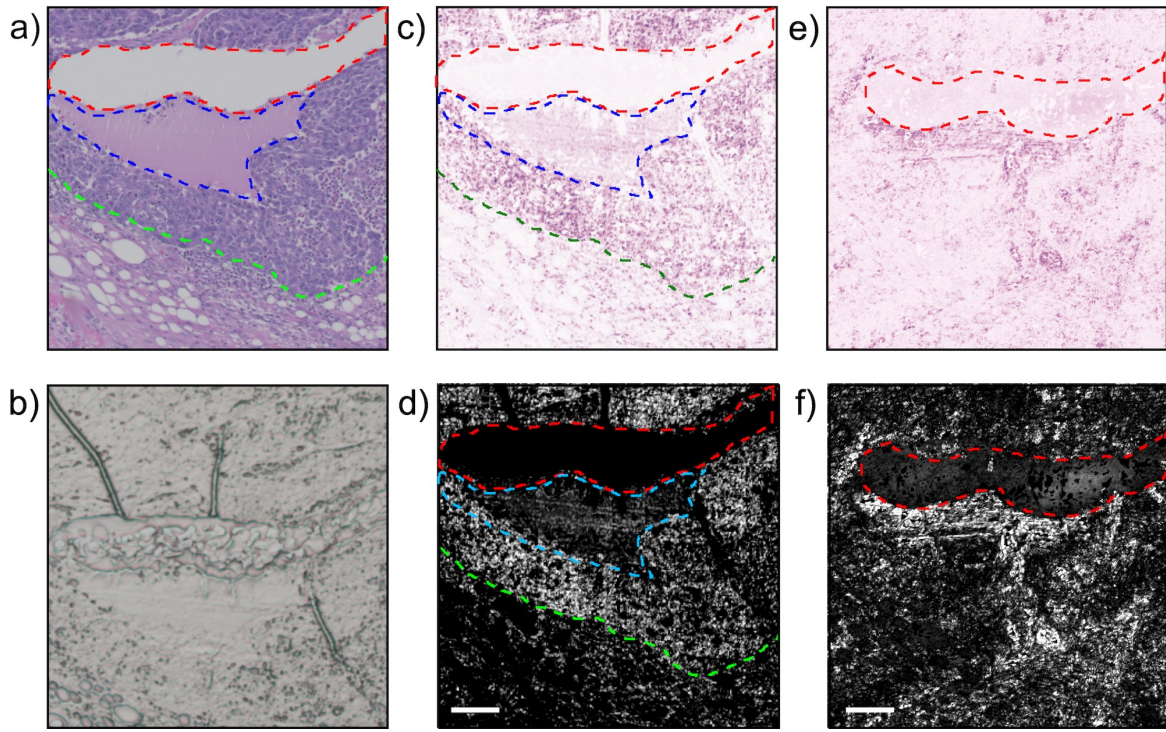
Figure 5.5: A comparison between a PARS images and **(a)** a bright-field image at the of the same breast tissue sample with invasive ductal carcinoma. **(b)** an unstained slide imaged with a conventional bright field microscope. A PARS acquisition of the regions is shown for the unstained tissue slide with **(c)** a false H&E colour map applied and a **(d)** logarithmic greyscale colour map applied. A PARS acquisition of a FFPE block with **(e)** a false H&E colour map applied and **(f)** a logarithmic greyscale colour map applied. Green outline highlights a sharp delineation between a hypercellular region of tissue and healthy tissue, blue outline represents a high-grade malignancy with serosity and necrotic cells, the red outline represents an artifact present in the slides. Scale bar 100 µm.

various depths and cellular resolution is maintained 50 µm down into the sample. The image formation method for each depth level is identical to image reconstruction for each mosaic frame and is described in more detail in section 3.2.3.

5.2.4 Internuclear distance and cross-sectional area comparison

H&E image (Fig. 5.9a) were compared to the adjacent PARS acquisitions (Fig. 5.9b) with several quantitative metrics. The cross-sectional area of the cell nuclei (Fig. 5.9c), the internuclear distance (Fig. 5.9d), and a circularity ratio of the cell nuclei (Fig. 5.9e) are shown with results summarized in Table 5.1. Three quantitative metrics are used
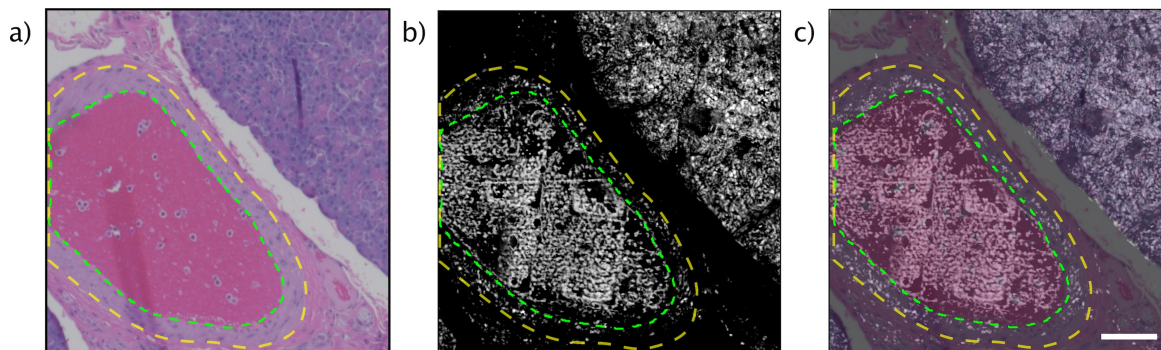
Figure 5.6: **(a)** A standard H&E prepared slide imaged with a standard pathology microscope of a blood vessel (within green outline) located in pancreatic tissue, surrounded by muscular layer (between green and yellow outline) with smooth muscle cells. **(b)** An unstained tissue slide of the adjacent section imaged with PARS. **(c)** A direct overlay of the images **(a,b)**. Scale bar 100 µm.
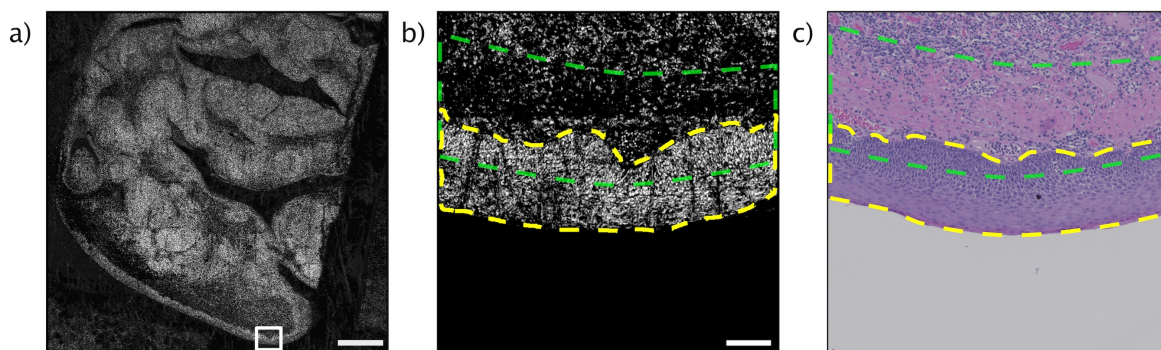
Figure 5.7: **(a)** A large field-of-view scan of a tonsil tissue specimen using PARS microscopy. Scale bar 1 mm. **(b)** A high resolution zoomed-in scan of the skin margin its superficial hypercellular stratified squamous epithelium (yellow outline) and the sharp delineation with the underneath hypocellular stroma (green outline) using PARS microscopy. Scale bar 100 µm. **(c)** an H&E prepared tissue slice of the adjacent section of tonsil tissue.

to compare the bright-field H&E images with PARS acquisitions. These metrics include internuclear spacing, nuclear cross-section, and the circularity of the nuclei. Internuclear spacing and nuclear cross-section are first pulled from images by thresholding nuclear structures from the background. The center of mass of each nucleus is determined by the arithmetic mean along each dimension. Then, the minimum calculated distance between each centre of mass is determined to be the reported internuclear spacing. The nuclear cross-section is found for each nucleus by summing the total number of constituent pixels and multiplying by the area of each pixel. The circularity ratio is defined as $CR = \frac{C^2}{4\pi A}$
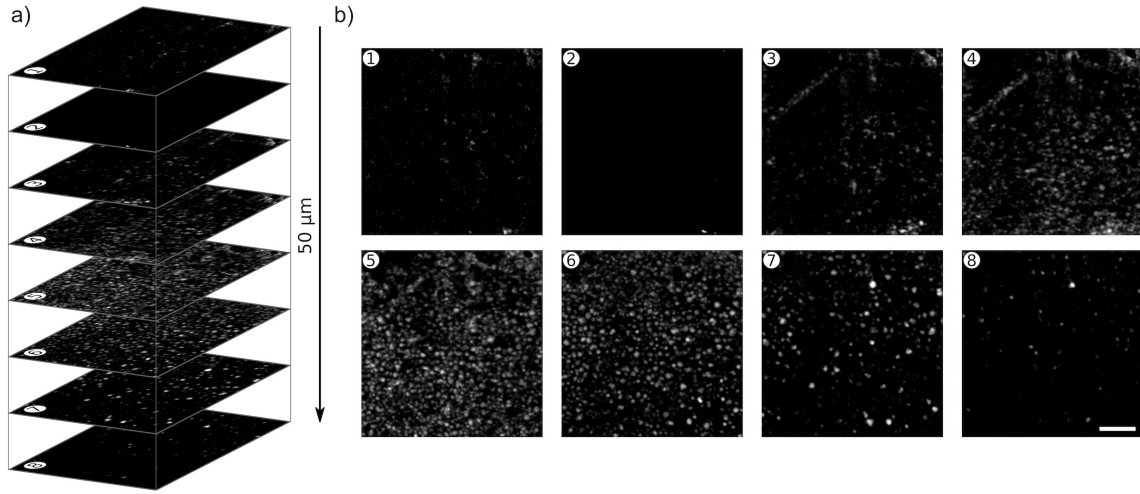
Figure 5.8: A volumetric scan of breast cancer tissue (invasive ductal carcinoma) **(a)** Consecutive slices are shown with separation of 7 μm. **(b)** The sections from **(a)** are shown. Scale bars 20 μm.

where C and A are the circumference and area of each cell nuclei, respectively. If the nuclei are perfectly circular, this ratio would be unity. Deviation from unity suggests a non-circular shape. The perimeter of each object is taken as the sum of perimeter pixels times the dimension of each pixel, and the area is as defined for the cross-section. Diagnostically relevant information on tissue types may be pulled from mean values, whereas cancerous tissues may exhibit larger variances.

Summary of Cell Morphology Metrics								
	Cross-Sectional Nuclear Area			**Internuclear Distance**			**Circularity Ratio**	
	Mean	**SD**	**Overlap**	**Mean**	**SD**	**Overlap**	**Mean**	**SD**	**Overlap**
H&E	13.3	7.7	0.79	10.3	6.5	0.89	1.42	0.77	0.87
PARS	17.5	9		9.21	4.7		1.54	1	

Table 5.1: The calculated mean, standard deviation (SD) and overlap coefficients for the 3 qualitative analysis techniques for the H&E and PARS images in Figs. 5.9a,b
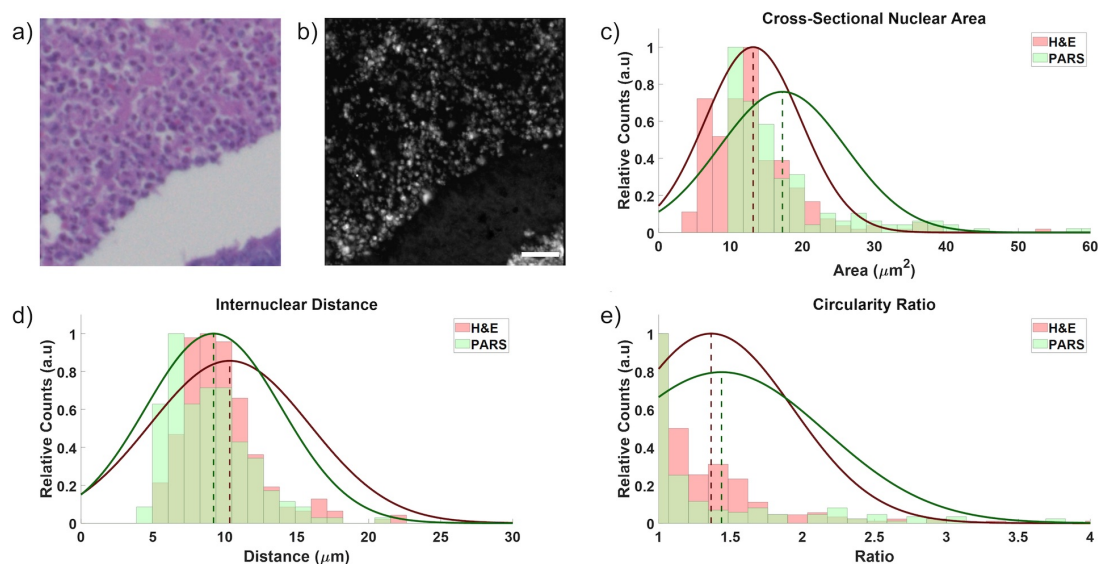
Figure 5.9: Quantitative study from **(a)** an image of a standard H&E prepared breast tissue sample captured by a commercial bright field microscope **(b)** a PARS image of the adjacent breast tissue section on the FFPE block. **(c)** A comparison of the cross-sectional nuclear area, **(d)** a comparison of the internuclear distance between cell nuclei, and **(e)** a comparison of the circularity ratio extracted from images **(a,b)**. See Table 5.1 for further details.

5.3   Discussion

The system presented here highlights several important capabilities necessary for histology-like imaging of tissues. PARS does not require additional contrast to be added to the sample. The unstained slides provide a reasonable contrast-free analog to the prepared and stained H&E samples. The contrast in the PARS images is provided by the 266 nm absorption peak of the sample, primarily highlighting DNA concentration. However, other surrounding species are likely to contribute signal to some degree, such as cytochrome, hemoglobin, and collagen30 to name a few as they exhibit non-zero absorption at 266 nm. The high concentration of DNA in cell nuclei facilitates visualization of nuclear morphology, nuclear density, and cellular distribution. This is due to the PARS signal being proportional to the optical absorption, which is in-turn proportional to the chromophore concentration. The contrast seen in H&E sections is from cell nuclei (purple) and the surrounding cytoplasm (pink) (Figs 5.5a, 5.6a, 5.7c). The hematoxylin dye is principally used as a nuclear stain whereas eosin visualizes the cytoplasm. The PARS images in this study provide contrast analogous to the hematoxylin stain as the 266 nm wavelength is strongly

absorbed by DNA within cell nuclei. This relationship is similar to the one that exists in H&E preparation, where the intensity of the hematoxylin stain is proportional to the negative ion concentration present in DNA and RNA. Since PARS operates in reflection-mode, the samples are not required to be thin, negating additional sectioning. Both capabilities are essential to achieve *in-situ* imaging capability and are demonstrated with the FFPE blocks.

The ability to image thick tissue combined with DNA's strong absorption at 266 nm may also permit the imaging of freshly resected tissue. Freshly resected tissue can potentially contain blood and other fluids. The extra blood and serosity can be removed with absorbing paper before inking the specimen. This is standard practice and is routinely done before staining the tissue. However, this extra step may not be required as the excess fluids would not interfere with the system's ability to visualize surgical margins. Although blood appears as an opaque fluid macroscopically, the majority of its contrast is exhibited by erythrocytes, which are discrete cells. Thus, under magnification, the extra contrast from hemoglobin does not disrupt histological imaging. With PARS, there is an added benefit that erythrocytes are anuclear and do not exhibit significant optical absorption as compared to DNA at 266 nm. Since DNA absorbs 266 nm wavelength significantly more than hemoglobin and other chromophores [135], the dominant contrast would still be from DNA facilitating the visualization of surgical margins and cellular morphology. Similarly, this work can also be applied to surgical cavities left behind by resections. Such resections can extend deep into the body and the surgeon must proceed with hemostasis. Presently, the surgeon must palpate the cavity to identify residual nodularity. This work may be applied to such cavities to visualize any residual cancer. The non-contact operation of this modality also minimizes the increased risk of infection posed by palpating deep cavities in the body.

PARS images of the unstained slides highlight salient features of the sample, including regions of hypercellularity and distinct boundaries between different tissue types. Figure 5.5 shows bright-field images of H&E stained (Fig. 5.5a), unstained tissue slides (Fig. 5.5b), PARS images of the same unstained tissue slide (Fig. 5.5c,d) and FFPE blocks (Fig. 5.5e,f). The tissue sample consists of human breast tissue presenting invasive ductal carcinoma. The H&E image (Fig. 5.5a) highlights a sharp delineation between cancerous and healthy cells (green outline). A high-grade tumor (blue outline) is also seen in the same figure, whereas the red outline accentuates a tissue processing artifact. In contrast, in the unstained bright-field image (Fig. 5.5b), the high-grade tumor and the sharp delineation between diseased and healthy tissue are not visible. The PARS images (Fig. 5.5c,d) of the unstained tissue demonstrates the visual differences and morphology of the breast gland duct from exocrine and cancerous cells (green outline) and adjacent adipose tissue

with comparable fidelity to the H&E image. The processing artifact and the high-grade tumor are also clearly visible in the PARS images of the unstained tissue slide. The PARS images of the FFPE blocks (Fig. 5.5e,f) are concordant with the co-localized unstained sectioned samples and the bright-field H&E images. Salient micron-scale structures such as hypercellularity, internuclear spacing, nuclear morphology, and intranuclear density are captured, along with larger-scale features such as ducts, adipose tissue, connective tissue, and blood vessels. Where the FFPE blocks provide a closer analog to *in-situ* tissues, the unstained sectioned slides yield a closer analog to the conventional H&E processed slides as the preparation procedure follows a similar process but lack the contrast dyes. Figure 5.6 cellular morphology in human pancreatic tissue with H&E stained and PARS images. Figure 5.6a is a standard H&E image that of a medium-sized blood vessel that is surrounded by a muscular layer. Bulk tissue and cellular morphology are visualized in the PARS image (Fig. 5.6b) and found to be comparable to the H&E image. Due to the presence of nucleated cells (smooth muscle cells) present in the muscular layer surrounding the blood vessel (between yellow and green outline). Figure 5.6c is an overlay of the H&E image and PARS image demonstrating the agreement between the two modalities. Figure 5.7 compares H&E images and PARS images of human tonsil tissue. Figure 5.7b demonstrates the difference between the hypercellular stratified squamous epithelium and the sharp delineation (yellow outline) with the underneath hypocellular stroma.

In the future, a method is required to provide images with eosin-like cytoplasmic staining patterns, where co-imaging would provide the dual contrast signal analogous to H&E staining. PARS is capable of incorporating additional excitation wavelengths which could be added to provide contrast for additional chromophores, targeting various components of the tissue structure. To achieve eosin-like contrast, a roughly 400 nm excitation wavelength has previously shown to reveal cytochromes in the cytoplasm [27]. An infrared excitation source such as 1210 nm or 1720 nm can also be added to extract contrast provided by adipocytes, which is otherwise unavailable in standard H&E preparation due to the dissolution of lipid by ethanol and xylene during tissue processing [136]. This additional contrast may reduce ambiguity of the PARS chromophore recovery at any given wavelength. Nonetheless, nuclear features and other tissue features such as blood vessels (Fig. 5.6), duct morphology, hypercellularity, and connective tissue structures are readily evident in the PARS images of excised tissues. Future iterations can multiplex different excitation wavelengths targeting specific chromophores in the same acquisition session, which allows for large amounts of diagnostic information to be extracted quickly, label-free, and *in-situ*.

Volumetric imaging experiments (Fig. 5.8) highlight the performance of the apparatus in thick tissue samples. Here, imaging was performed across a depth range of 50 μm showing

several cellular layers. This appears to be the penetration limit for the current system in these FFPE blocks and is similar to the depth reported in previous transmission-mode UV-PAM works [26]. Since the transport mean free path of the 266 nm ultraviolet light is on the order of 100 µm in human tissue, this range may be expected for an optical system which operates at these wavelengths. PARS has previously demonstrated the ability to exceed the transport mean free path of the excitation wavelength in tissue using a deeper penetrating detection beam [10]. This may suggest appreciable interaction between the 1310 nm detection source and the FFPE blocks' paraffin media. Future efforts may need to investigate other detection wavelengths for imaging such prepared samples.

The qualitative analysis techniques used may provide additional metrics for PARS-based computer-aided diagnostics which is essential for approaching the gold-standard of human pattern recognition. This is critical for tissue identification and initial tissue diagnostics. For instance, the variance in the cross-sectional area and circularity of cell nuclei is indicative of nuclear aberrancy and the internuclear distance can indicate hypercellularity, which could suggest the presence of cancerous tissue. The extracted values show good correspondence between the two datasets suggesting PARS is capable of accurate visualization of nuclear structure. This highlights the potential for PARS microscopy in computational diagnostics and especially surgical margin assessment.

The imaging characteristic demonstrated reasonably fast frame acquisition times and sub-cellular resolution. However, the current system would be incapable of delivering full-quality frames as shown at real-time rates (greater than a frame per second). Imaging speeds can be improved by increasing the pulse repetition rate of the laser, potentially achieving real-time imaging speeds. PARS microscopy has demonstrated higher imaging rates in comparison to contact-based photoacoustic imaging methods due to the optical detection. The rate of optical detection with PARS is limited by the local stress confinement rather than acoustic propagation. The method has previously demonstrated acquisition rates up to 5 MHz [137] suggesting if an appropriately fast repetition rate excitation is implemented, real-time feedback to clinicians is likely feasible.

Chapter 6

Chromophore selective multi-wavelength photoacoustic remote sensing of unstained human tissues

In the previous chapter, we demonstrated imaging of nuclear morphology in a variety of unstained human tissues. However, standard H&E staining typically highlights several chromophores in addition to DNA. While hematoxylin targets DNA, eosin targets cytoplasm, collagen, and hemoglobin. Thus, to approach the diagnostic information provided H&E, it is necessary to recover contrast from additional chromophores. In this chapter, in addition to the nuclear contrast, we target hemoglobin by taking advantage of its optical absorption peak near green wavelengths. By incorporating an additional green excitation laser, the first results of multi-wavelength imaging in human pancreatic and tonsil tissues are reported. These images are compared against standard H&E prepared slides.

6.1 Materials and methods

This chapter employs the system described in section 3.2.1 to image cell nuclei and red blood cells. The 266 nm source is used to target cell nuclei (akin to staining with hematoxylin only) whereas the 532 nm source is used to visualize the hemoglobin present with the tissue specimens. The sample preparation method is previously described in section 5.1.3.

In this section, we describe an analysis discussing the relative reflectivity of DNA and red blood cells.

6.1.1   Imaging mechanism

PARS utilizes both a pulsed excitation laser and a continuous-wave detection laser in order to generate and detect initial PA pressures. In brief, an excitation pulse incident on an optically absorbing region produces thermo-elastic expansion through the photoacoustic effect generating large initial pressures. These initial pressures modulate the local refractive index via the elasto-optic effect, modulating the scattering properties of this region [89, 11]. Meanwhile, a continuous-wave detection beam is co-focused with the excitation spot. The modulating scattering profile induces intensity variations in the back-scattered detection beam. Photoacoustic signals are measured as variations of this back-scattered intensity. The magnitude of these signals is proportional to the optical absorption of the absorber at the excitation wavelength [9, 11, 12].

Following the analytical methods described in [9, 12], and using values for optical absorption of biomolecules presented by Soltani *et al.* we calculate the PARS reflectivity changes for cell nuclei to compare against red blood cells (RBC) [135, 138]. Cells are modeled using refractive indices of 1.358 and 1.377 for cell nuclei and cytoplasm respectively [139]. Red blood cells are modeled using refractive indices of 1.413 for the cell, and 1.33 for the blood plasma [140, 141]. The radius of a diffraction-limited focal spot size can be computed using the expression $R = \frac{0.5\lambda}{NA}$ where λ is the wavelength and NA is the numerical aperture of the objective [142, 143]. With a 0.3 NA objective, this expression yields a radius of 440 nm for 266 nm excitation and approximately 880 nm for 532 nm excitation. In comparison, red blood cells have a diameter between 6.8 and 7.5 µm [144]. The mammalian cell nucleus has an average size of 6 µm [145]. Since both the cell nuclei and the red blood cells are much larger than the detection wavelength and the focal spot size, a simple planar interface is assumed. The PARS signal will then be a result of comparing the unperturbed reflection from this structure, assuming a Fresnel interface, and the perturbed reflection following photoacoustic excitation and elasto-optic modulation of the absorbing medium. This signal is then characterized as the reflectivity difference ΔR between the two reflections. This yields reflectivity changes of $\Delta R_{DNA,266} = 1.43 \times 10^{-4}$, $\Delta R_{DNA,532} = 1.88 \times 10^{-7}$, $\Delta R_{RBC,266} = 7.88 \times 10^{-6}$, and $\Delta R_{RBC,532} = 1.78 \times 10^{-5}$ where $\Delta R_{DNA,\lambda}$ is the reflectivity change for DNA in cell nuclei at λ and $\Delta R_{RBC,\lambda}$ is the reflectivity change for RBC at λ. For these calculations excitation fluences are assumed to be at ANSI limits of 3 mJ/cm2 for 266 nm and 20 mJ/cm2 for 532 nm. This yields predicted fractional signals of $\frac{\Delta R_{DNA,266}}{\Delta R_{RBC,266}} = 18.1$ at 266 nm and $\frac{\Delta R_{RBC,532}}{\Delta R_{DNA,532}} = 94.5$ at 532 nm.

6.1.2 Image formation

The image formation method for a multi-wavelength setup is similar to the one described in section 3.2.2. For each multi-wavelength acquisition, the 266 nm excitation was first employed to recover the nuclear contrast. The 266 nm acquisition was followed by the 532 nm excitation to capture hemoglobin contrast. The nuclear and hemoglobin contrasts were then provided a colormap and superimposed to emulate an H%E-stained histology-like image.

6.1.3 Resolution characterization

To characterize the lateral resolution of the system, carbon fibers were imaged at 266 nm (Fig. 6.1(a)) and 532 nm (Fig. 6.1(c)) wavelengths. The resolution is characterized by fitting an edge spread function to a carbon fiber's edge pixel values. The lateral resolution is then defined as the width between 10% and 90% of the maximum amplitude of the edge spread function. The resolution for the 266 nm beam was found to be 1.2 µm and for 532 nm was found to be 1.5 µm.
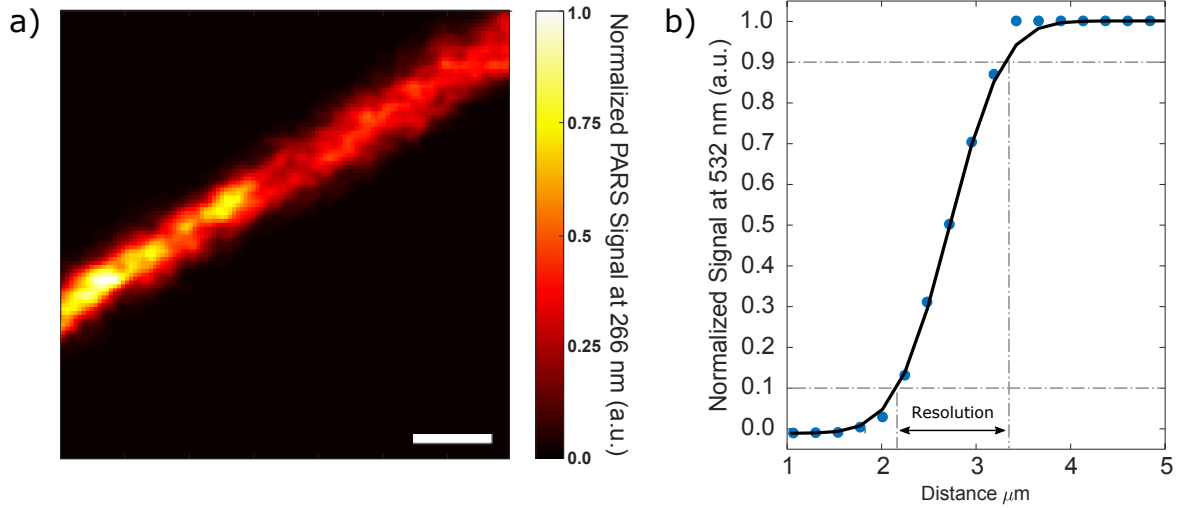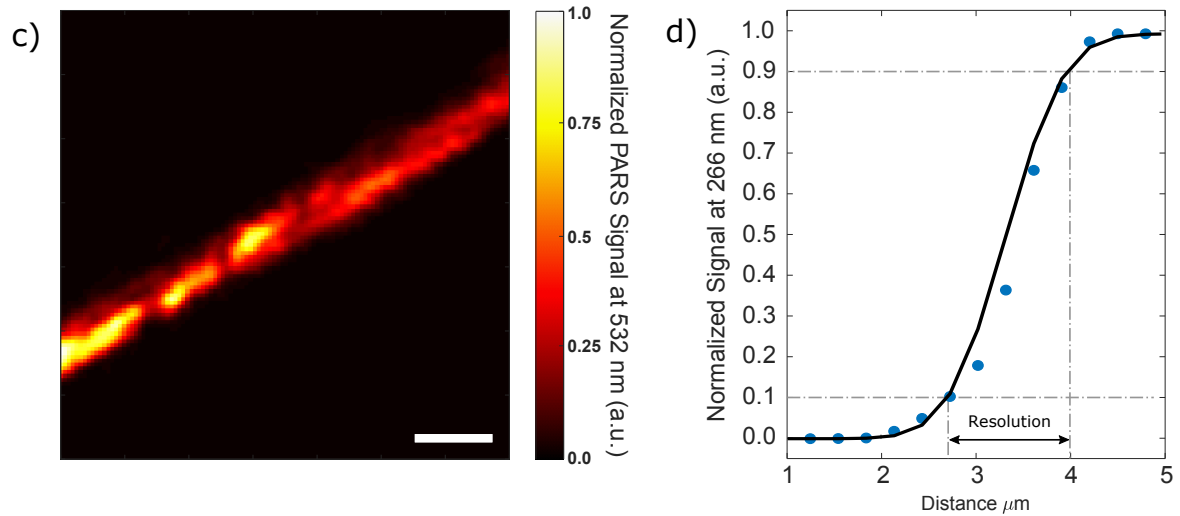
Figure 6.1: Resolution characterization of the multi-wavelength PARS system **(a)** carbon fibers imaged with the 266 nm excitation **(b)** corresponding edge-spread function measuring a resolution of 1.2 µm **(c)** carbon fibers imaged with the 532 nm excitation **(d)** corresponding edge spread function measuring a resolution of 1.5 µm. Scale bar 10 µm.

6.2 Results and discussion

Figure 6.2 compares a high-resolution H&E image (Fig. 6.2(a)) of human epidermal tissue with a PARS image (Fig. 6.2(b)) of an unstained adjacent section. The PARS image is able to resolve cell nuclei similar to the H&E section. As the images are of adjacent sections and not of the same tissue sample, the cell nuclei do not appear at the same locations in both images.

Using the apparatus described in Fig. 3.1, we imaged and compared unstained human pancreatic (Fig. 6.3) and tonsil tissue (Fig. 6.4) sections to adjacent H&E stained sections (Fig. 6.3(a) and Fig. 6.4(a)). The tissue sections were first imaged with a 266 nm excitation wavelength (Fig. 6.3(b) and Fig. 6.4(b)) followed by a 532 nm excitation wavelength (Fig. 6.3(c) and Fig. 6.4(c)). The 266 nm and 532 nm images were then superimposed as shown in Fig. 6.3(d) and Fig. 6.4(d) emulating contrast from an H&E colour map.

The contrast provided in Fig. 6.3(b) and Fig. 6.4(b) image highlights the optical absorption of DNA at 266 nm. As a result, cellular morphology and bulk tissue structure are distinguishable in reference to the H&E prepared section. The areas corresponding to hemoglobin (blue outlines in Fig. 6.3 and Fig. 6.4) lack signal in the cells presumed to be
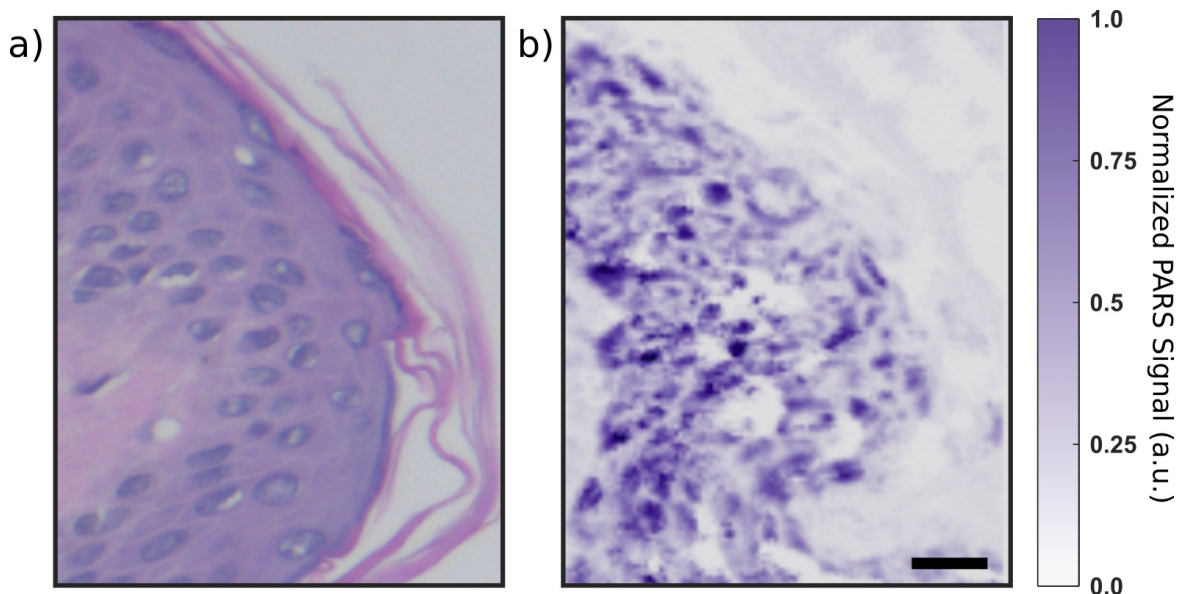
Figure 6.2: **(a)** high-resolution H&E image of human epidermal tissue **(b)** high-resolution PARS image with a 266 nm excitation of an adjacent section. Color bar represents normalized PARS signal. Scale bar 10 μm.
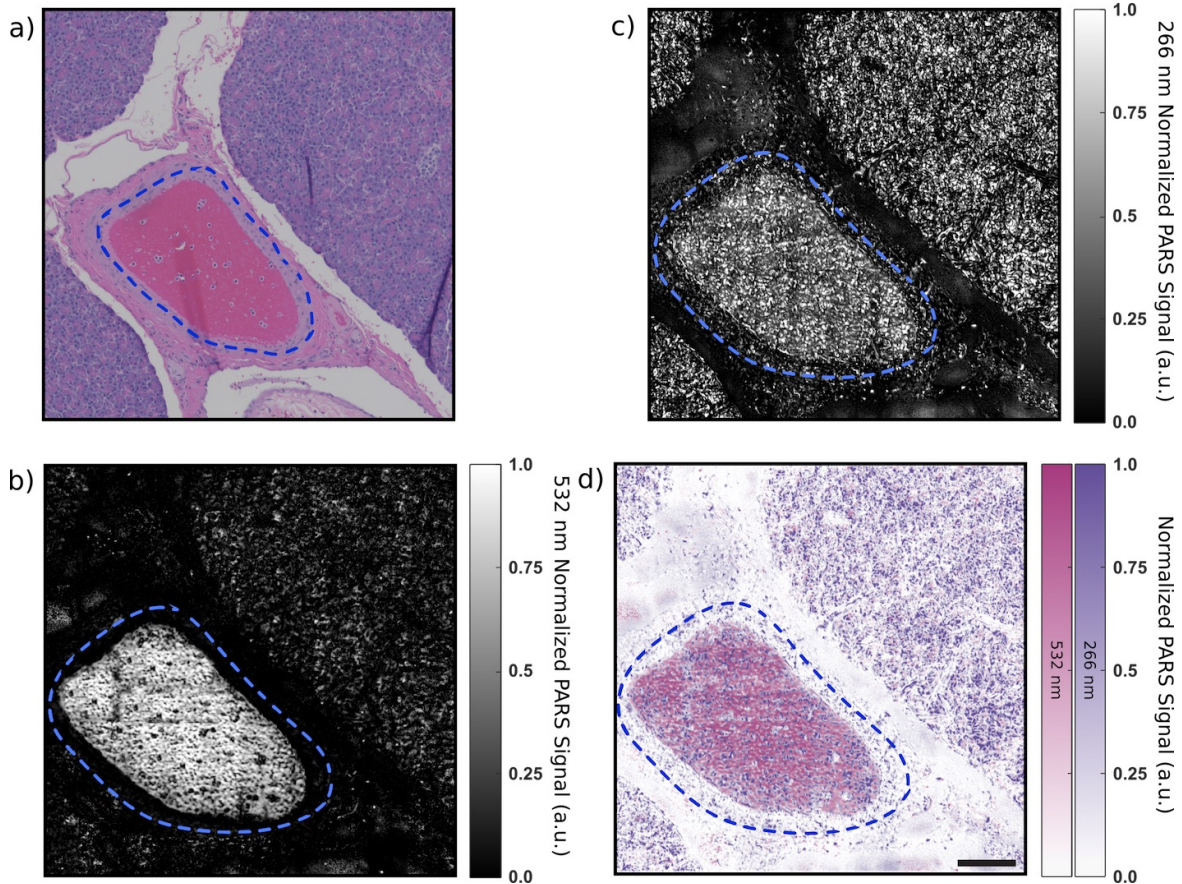
Figure 6.3: **(a)** A standard H&E stained slide of a blood vessel (blue outline) within human pancreatic tissue imaged with a conventional brightfield microscope. **(b)** An adjacent unstained slide of the same specimen imaged with 266 nm excitation and **(c)** with 532 nm excitation. **(d)** A superimposed image of **(b)** and **(c)** with a histology-like colormap, DNA is colored purple, hemoglobin is colored red. Scale bar 100 μm.

erythrocytes, since they are anuclear and do not have DNA to strongly absorb the 266 nm excitation. Similarly, 532 nm excitation images shown in Fig. 6.3(c) and Fig. 6.4(c) presents hemoglobin contrast as comparable to their corresponding H&E prepared section. The blood vessel as outlined in Fig. 6.3(d) can be identified in comparison to the H&E prepared section in Fig. 6.3(a). The 266 nm signal (Fig. 6.3(b)) also shows other nucleated cells of blood in the vessel lumen, such as leukocytes, that are clearly evident in the background of the 532 nm signal from erythrocytes (Fig. 6.3(c)). The PARS-imaged signals from erythrocytes and nucleated cells of blood correspond well with the H&E image
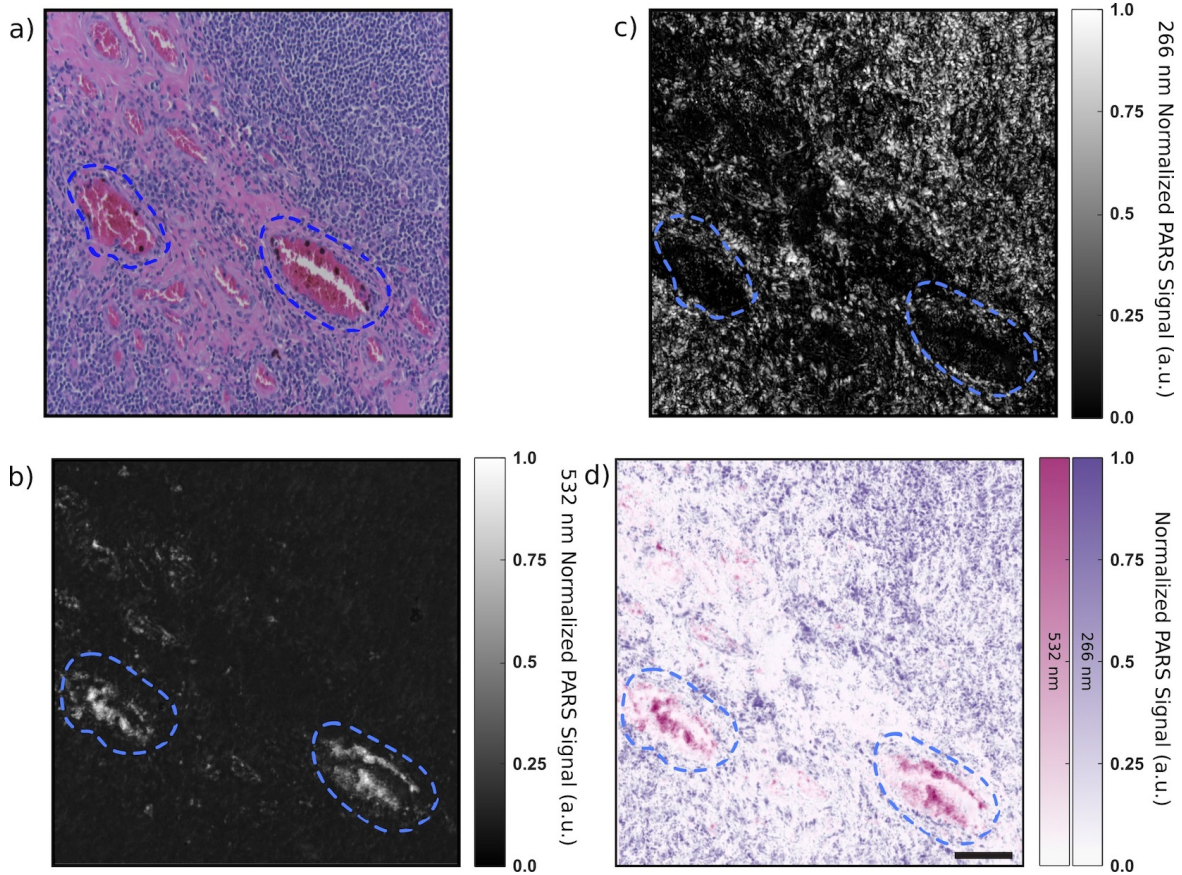
Figure 6.4: **(a)** A standard H&E stained slide of venules (blue outline) embedded within a human tonsil tissue imaged with a conventional brightfield microscope. **(b)** An adjacent unstained slide of the same specimen imaged with 266 nm excitation and **(c)** with 532 nm excitation. **(d)** A superimposed image of **(b)** and **(c)** with a histology-like colormap, DNA is colored purple, hemoglobin is colored red. Scale bar 100 µm.

(Fig. 6.3(a)), and (Fig. 6.3(d)) suggest an enhanced ability of PARS to identify these nucleated cells amongst the population of erythrocytes. Similarly, the hemoglobin highlighted by the 532 nm excitation (Fig. 6.4(c)) in the tonsil tissue is comparable to the location of erythrocytes in Fig. 6.4(a). Although hemoglobin and DNA are assumed to be the primary absorbers at the excitation wavelengths, other chromophores such as cytochrome and collagen will produce non-zero signals at these same wavelengths. However, their contributions are considered to be negligible.

Nuclear density, morphology, and organization are critical identifiers which are com-

monly used to diagnose tissue samples. For example, the nucleus is the best cellular subunit to identify a cell. Semi-quantitative measurements such as the "nucleus/cytoplasm" ratio (N/C) are used in order to identify malignant versus healthy cells, as malignant cells are biologically more aggressive and therefore tend to have a larger nucleus and smaller cytoplasm. As we demonstrate PARS is capable of imaging targeted chromophores in human tissues with a multi-wavelength excitation design, additional excitation wavelengths may be added to image additional chromophores. A 422 nm excitation wavelength has previously shown efficacious visualization of the cytoplasm, emulating an eosin-like stain [27]. Furthermore, an 1197 nm excitation wavelength has been previously used to image adipose tissue which is otherwise lost during the extensive H&E staining process [146]. These features can be useful in distinguishing among different tissue types and are some of the important histopathologic features that distinguish normal tissue from cancerous tissue. The contrast delivered by multi-wavelength excitation PARS permits regions of cancer to be identified even if they are macroscopically indistinguishable from benign tissue, which can guide more accurate surgical resection.

Chapter 7

Conclusion

This research sought to take preliminary steps towards an *in-situ* imaging technique. These preliminary steps involved imaging a variety of thin and thick human tissues using PARS microscopy. Adjacent H&E stained sections were prepared and compared against the PARS images. These comparisons demonstrated good concordance between the two modalities. In particular, the non-contact label-free reflection-mode imaging of FFPE tissue blocks represents a vital step towards an *in-situ* histology microscope. This work resulted in four key contributions toward our overarching goal.

The first contribution, described in Chapter 3, is a rapid gross assessment method was developed to scan arbitrarily sized samples. This technique was based on assembling mosaics by capturing tightly sampled patches by optical scanning. A set of mechanical stages permits the capture of these patches in a grid-like pattern. These individual frames are then assembled into a mosaic to yield wide field of views. The acquisition of mosaics results in a method that can scan arbitrarily sized specimens but maintain the high spatial sampling required for high-resolution imaging. Multiple results demonstrated the speed, tight spatial sampling, and FOV capabilities of the technique. The largest mosaic captured consisted of 400 patches and covered an area of 3 x 3 mm^2. The optical scanning resulted in an average step size of 570 nm. Mosaics of human breast tissue were also captured to demonstrate the technique's efficacy. This mosaic consisted of 100 frames and covered an area of 1 x 1 mm^2. In terms of speed, this method reported twice as fast acquisition rates over similar previous approaches. Since this technique minimizes the stage movement, it potentially allows for the scanning optics to be mounted on top of the stages. This would allow the scanning optics to be moved rather than the sample. Such a configuration may prove advantageous for *in-situ* imaging as the mechanical stages can move the scanning optics over a diseased region and capture high-resolution mosaics over arbitrary sized FOV.

Similarly, the system can also be programmed to image only over the cancer margins rather than the whole tumor to save valuable time during surgery. This would result in a mosaic with several blank frames, but the cancer margins would be clearly visualized *in-situ*.

The second contribution, discussed in section 4.1.3, came in the form of a real-time imaging system. The central development in this study was the implementation of a lightweight image reconstruction method. Recognizing that positional information signals were relatively noisy and did not provide 64-bit floating precision, the proposed method rounded off the signals to 16-bit integers. The rounding off effectively binned nearby points and were subsequently averaged together. This interpolation provided a live display with a 1.2 µm resolution and 62 dB peak SNR. The 1.2 µm resolution is, as far as the author is aware, the highest reported resolution for a real-time photoacoustic imaging system. This technique demonstrated frame rates as high as 2.5 Hz at a repetition rate of 600 kHz. At this repetition rate, the fast optical axis frequency was 960 Hz, close to their maximum rating of 1 kHz. Achieving higher frame rates will, therefore, require a set of faster scanning optics, such as MEMS mirrors or polygon mirrors. Real-time *in-vivo* imaging of microvasculature structures on mouse-ear demonstrated the method's efficacy. This method worked in 2D. By incorporating a motorized depth stage, multiple 2D slices were captured along the depth of the sample. These 2D were then used to form 3D volumes *in-vivo*. These results represent the first 3D volumes with PARS.

Chapter 5 describes the third contribution of this study, the development of a PARS system to image histology samples. This system used a 266 nm excitation laser to target the ultraviolet optical absorption peak of DNA. Through this, the sample nuclear morphology was recovered. A variety of human tissue samples were imaged, including human breast, gastrointestinal, and skin. The study investigated imaging unstained tissue slides as well as thick FFPE tissue blocks. These images were compared qualitatively against H&E stained adjacent sections demonstrated good agreement of the nuclear morphology. Further, a quantitative comparison between PARS and H&E images measured various diagnostic metrics and showed good agreement between the two modalities.

The final contribution was of a multi-wavelength PARS system to selectively image chromophores. The optical system is described in section 3.2.1 and histology-like results are demonstrated in section 6.2. The motivation was to approach the diagnostic potential of H&E staining, which stains collagen, hemoglobin, and cytochrome in addition to the cell nuclei. A 532 nm laser was incorporated to target hemoglobin contrast and enabled the imaging of red blood cells, previously not visualized with the 266 nm excitation. This system thus produced multicolor micrographs and visualized nuclear morphology and hemoglobin contrast. The system imaged unstained human pancreas and tonsil tissue, which were compared with H&E stained counterparts for validation of contrast. This

method was the first multi-wavelength PARS microscope.

These steps represent a significant step towards an *in-situ* imaging technique. Though not part of this thesis, PARS has already demonstrated H&E-like imaging by targeting the 420 nm optical absorption peak of cytoplasm. These new images are much closer to H&E in contrast and provide similar diagnostic information. Furthermore, circumventing the histologic tissue processing entirely, PARS has demonstrated H&E-like contrast directly on unprocessed thick tissues from mice. This positions PARS as a powerful tool for intraoperative morphological assessment. We summarize the imaging capabilities and key metrics of PARS and other modalities in Table 7.1.

7.1 Future work

Nevertheless, considerable work remains to be done. Video-like frame rates can be achieved by using a significantly faster laser, scanning optics, and by implementing the presently CPU-bound interpolation onto a GPU. Additionally, the present work of imaging fresh tissues must be extended to human fresh tissues. *In-vivo* imaging of tissue morphology, specially of tumors, would also lay the essential groundwork towards a human in-situ microscope. Moving forward, clinical sensitivity studies would be vital for understand the technique's diagnostic potential. Finally, similar to the inclusion of hemoglobin contrast, PARS can be extended to include lipid contrast, pushing it beyond what the gold standard H&E provides in terms of diagnostic information. These advancements, combined with the non-contact label-free reflection-mode architecture of PARS, may one day yield a microscope capable of revealing cancer *in-situ*. Such a tool would be a powerful addition to modern medicine's arsenal of imaging technologies.

Method	Contrast	Resolution (nm)	Imaging Depth	Non Contact	Label Free	Histology-like Specificity	FFPE Section	FFPE Block	Fresh Tissue (thick)	*in-situ* capability
MUSE	Fluorescence	~ 1000 [20]	< 0.05 mm [20]	Yes	No	Yes	Yes[19]	No[1]	Yes [19]	No
LSM	Fluorescence	$2000 - 3000$ [21]	< 0.2 mm [147]	Yes	No	Yes	No	No[1]	Yes [21]	No
SRS	Molecular Vibration	< 500 [23]	< 0.1 mm [42]	Yes	Yes	Yes	Yes [23]	No	No [2]	No
OCT	Optical Scattering	~ 10000 [66, 148]	2–3 mm [149]	Yes	Yes	No	Yes	Yes	Yes	Yes
UV-PAM	Optical Absorption	$700 - 1200$ [25]	< 1.0 mm [150]	No	Yes	Yes	Yes[26][3]	Yes[151][3]	Yes [25][3]	No
PARS	Optical Absorption	$400 - 700$ [152]	< 1.2 mm [10]	Yes	Yes	Yes	Yes[153]	Yes[153]	Yes[4]	Yes

[1] Requires the deparaffinization of FFPE Tissue Block to apply fluorescence stains. This process destroys the tissue block.
[2] Requires tissue to be squeezed into a thin specimen, typically 120 μm in thickness.
[3] Requires samples to be submerged in water.
[4] Demonstrated in "Reflection-mode virtual histology using photoacoustic remote sensing microscopy". This study has been submitted to a journal but not published as of this writing.

Table 7.1: Comparison of key parameters of various modalities

References

[1] Canadian Cancer Society and Statistics Canada. Canadian Cancer Statistics 2019. *Health promotion and chronic disease prevention in Canada: research, policy and practice*, 39, 2019.

[2] Statistics Canada. Leading causes of death, total population, by age group and ex, Canada. CANSIM (database), 2014.

[3] Shah Paras H., Moreira Daniel M., Okhunov Zhamshid, Patel Vinay R., Chopra Sameer, Razmaria Aria A., Alom Manaf, George Arvin K., Yaskiv Oksana, Schwartz Michael J., Desai Mihir, Vira Manish A., Richstone Lee, Landman Jaime, Shalhav Arieh L., Gill Inderbir, and Kavoussi Louis R. Positive Surgical Margins Increase Risk of Recurrence after Partial Nephrectomy for High Risk Renal Tumors. *Journal of Urology*, 196(2):327–334, August 2016.

[4] Funda Meric, Nadeem Q. Mirza, Georges Vlastos, Thomas A. Buchholz, Henry M. Kuerer, Gildy V. Babiera, S. Eva Singletary, Merrick I. Ross, Frederick C. Ames, Barry W. Feig, Savitri Krishnamurthy, George H. Perkins, Marsha D. McNeese, Eric A. Strom, Vicente Valero, and Kelly K. Hunt. Positive surgical margins and ipsilateral breast tumor recurrence predict disease-specific survival after breast-conserving therapy. *Cancer*, 97(4):926–933, 2003.

[5] Naruto Taira, Daisuke Takabatake, Kenjiro Aogi, Shozo Ohsumi, Shigemitsu Takashima, Rieko Nishimura, and Norihiro Teramoto. Phyllodes Tumor of the Breast: Stromal Overgrowth and Histological Classification are Useful Prognosis-predictive Factors for Local Recurrence in Patients with a Positive Surgical Margin. *Japanese Journal of Clinical Oncology*, 37(10):730–736, October 2007.

[6] Timothy M. Pawlik, Charles R. Scoggins, Daria Zorzi, Eddie K. Abdalla, Axel Andres, Cathy Eng, Steven A. Curley, Evelyne M. Loyer, Andrea Muratore, Gilles

Mentha, Lorenzo Capussotti, and Jean-Nicolas Vauthey. Effect of Surgical Margin Status on Survival and Site of Recurrence After Hepatic Resection for Colorectal Metastases. *Annals of Surgery*, 241(5):715–724, May 2005.

[7] Keith E. Volmar, Michael O. Idowu, Rhona J. Souers, Donald S. Karcher, and Raouf E. Nakhleh. Turnaround Time for Large or Complex Specimens in Surgical Pathology: A College of American Pathologists Q-Probes Study of 56 Institutions. *Archives of Pathology & Laboratory Medicine*, 139(2):171–177, February 2015.

[8] Shan-Rong Shi, Cheng Liu, Llana Pootrakul, Laurie Tang, Andrew Young, Ryan Chen, Richard J. Cote, and Clive R. Taylor. Evaluation of the Value of Frozen Tissue Section Used as "Gold Standard" for Immunohistochemistry. *American Journal of Clinical Pathology*, 129(3):358–366, March 2008.

[9] Parsin Hajireza, Wei Shi, Kevan Bell, Robert J. Paproski, and Roger J. Zemp. Non-interferometric photoacoustic remote sensing microscopy. *Light: Science & Applications*, 6(6):e16278–e16278, June 2017.

[10] Parsin Haji Reza, Kevan Bell, Wei Shi, James Shapiro, and Roger J. Zemp. Deep non-contact photoacoustic initial pressure imaging. *Optica*, 5(7):814–820, July 2018.

[11] Kevan L. Bell, Parsin Hajireza, Wei Shi, and Roger J. Zemp. Temporal evolution of low-coherence reflectometry signals in photoacoustic remote sensing microscopy. *Applied Optics*, 56(18):5172–5181, June 2017.

[12] Kevan Bell, Parsin Hajireza, and Roger Zemp. Scattering cross-sectional modulation in photoacoustic remote sensing microscopy. *Optics Letters*, 43(1):146–149, January 2018.

[13] Gufeng Wang and Ning Fang. Chapter four - Detecting and Tracking Nonfluorescent Nanoparticle Probes in Live Cells. In P. Michael conn, editor, *Methods in Enzymology*, volume 504 of *Imaging and Spectroscopic Analysis of Living Cells*, pages 83–108. Academic Press, January 2012.

[14] Douglas B. Murphy. *Fundamentals of Light Microscopy and Electronic Imaging*. Wiley-Liss, New York, 2001.

[15] Michael H. Ross and Wojciech Pawlina. *Histology*. Lippincott Williams & Wilkins, 2006.

[16] Saeed Alshieban and Khaled Al-Surimi. Reducing turnaround time of surgical pathology reports in pathology and laboratory medicine departments. *BMJ quality improvement reports*, 4(1), 2015.

[17] Christina E. Day, editor. *Histopathology: Methods and Protocols.* Methods in Molecular Biology. Humana Press, 2014.

[18] Jordan Atkins, Fatema Al Mushawah, Catherine M. Appleton, Amy E. Cyr, William E. Gillanders, Rebecca L. Aft, Timothy J. Eberlein, Feng Gao, and Julie A. Margenthaler. Positive Margins Rates Following Breast-Conserving Surgery for Stage I–III Breast Cancer: Palpable versus Non-Palpable Tumors. *The Journal of surgical research*, 177(1):109–115, September 2012.

[19] Farzad Fereidouni, Zachary T. Harmany, Miao Tian, Austin Todd, John A. Kintner, John D. McPherson, Alexander D. Borowsky, John Bishop, Mirna Lechpammer, Stavros G. Demos, and Richard Levenson. Microscopy with ultraviolet surface excitation for rapid slide-free histology. *Nature Biomedical Engineering*, 1(12):957–966, December 2017.

[20] Weisi Xie, Ye Chen, Yu Wang, Linpeng Wei, Chengbo Yin, Adam K. Glaser, Mark E. Fauver, Eric J. Seibel, Suzanne M. Dintzis, Joshua C. Vaughan, Nicholas P. Reder, and Jonathan T. C. Liu. Microscopy with ultraviolet surface excitation for wide-area pathology of breast surgical margins. *Journal of Biomedical Optics*, 24(2):026501, February 2019.

[21] Adam K. Glaser, Nicholas P. Reder, Ye Chen, Erin F. McCarty, Chengbo Yin, Linpeng Wei, Yu Wang, Lawrence D. True, and Jonathan T. C. Liu. Light-sheet microscopy for slide-free non-destructive pathology of large clinical specimens. *Nature Biomedical Engineering*, 1(7):1–10, June 2017.

[22] Ye Chen, Weisi Xie, Adam K. Glaser, Nicholas P. Reder, Chenyi Mao, Suzanne M. Dintzis, Joshua C. Vaughan, and Jonathan T. C. Liu. Rapid pathology of lumpectomy margins with open-top light-sheet (OTLS) microscopy. *Biomedical Optics Express*, 10(3):1257–1272, March 2019.

[23] Daniel A. Orringer, Balaji Pandian, Yashar S. Niknafs, Todd C. Hollon, Julianne Boyle, Spencer Lewis, Mia Garrard, Shawn L. Hervey-Jumper, Hugh J. L. Garton, Cormac O. Maher, Jason A. Heth, Oren Sagher, D. Andrew Wilkinson, Matija Snuderl, Sriram Venneti, Shakti H. Ramkissoon, Kathryn A. McFadden, Amanda Fisher-Hubbard, Andrew P. Lieberman, Timothy D. Johnson, X. Sunney Xie, Jay K.

Trautman, Christian W. Freudiger, and Sandra Camelo-Piragua. Rapid intraoperative histology of unprocessed surgical specimens via fibre-laser-based stimulated Raman scattering microscopy. *Nature Biomedical Engineering*, 1(2):1–13, February 2017.

[24] Barbara Sarri, Flora Poizat, Sandro Heuke, Julien Wojak, Florence Franchi, Fabrice Caillol, Marc Giovannini, and Herve Rigneault. Stimulated Raman histology: One to one comparison with standard hematoxylin and eosin staining. *Biomedical Optics Express*, 10(10):5378–5384, September 2019.

[25] Da-Kang Yao, Konstantin Maslov, Kirk K. Shung, Qifa Zhou, and Lihong V. Wang. In vivo label-free photoacoustic microscopy of cell nuclei by excitation of DNA and RNA. *Optics Letters*, 35(24):4139–4141, December 2010.

[26] Terence T. W. Wong, Ruiying Zhang, Pengfei Hai, Chi Zhang, Miguel A. Pleitez, Rebecca L. Aft, Deborah V. Novack, and Lihong V. Wang. Fast label-free multi-layered histology-like imaging of human breast cancer by photoacoustic microscopy. *Science Advances*, 3(5):e1602168, May 2017.

[27] Chi Zhang, Yu Shrike Zhang, Da-Kang Yao, Younan Xia, and Lihong V. Wang. Label-free photoacoustic microscopy of cytochromes. *Journal of Biomedical Optics*, 18(2):020504, January 2013.

[28] A. H. Voie, D. H. Burns, and F. A. Spelman. Orthogonal-plane fluorescence optical sectioning: Three-dimensional imaging of macroscopic biological specimens. *Journal of Microscopy*, 170(3):229–236, 1993.

[29] A. K. Glaser, Y. Wang, and J. T. C. Liu. Assessing the imaging performance of light sheet microscopies in highly scattering tissues. *Biomedical Optics Express*, 7(2):454–466, February 2016.

[30] Peter G. Pitrone, Johannes Schindelin, Luke Stuyvenberg, Stephan Preibisch, Michael Weber, Kevin W. Eliceiri, Jan Huisken, and Pavel Tomancak. OpenSPIM: An open-access light-sheet microscopy platform. *Nature Methods*, 10(7):598–599, July 2013.

[31] Philipp J. Keller, Annette D. Schmidt, Joachim Wittbrodt, and Ernst H. K. Stelzer. Reconstruction of Zebrafish Early Embryonic Development by Scanned Light Sheet Microscopy. *Science*, 322(5904):1065–1069, November 2008.

[32] Jörg Gerhard Ritter, Roman Veith, Andreas Veenendaal, Jan Peter Siebrasse, and Ulrich Kubitscheck. Light Sheet Microscopy for Single Molecule Tracking in Living Tissue. *PLOS ONE*, 5(7):e11639, July 2010.

[33] Thomas A. Planchon, Liang Gao, Daniel E. Milkie, Michael W. Davidson, James A. Galbraith, Catherine G. Galbraith, and Eric Betzig. Rapid three-dimensional isotropic imaging of living cells using Bessel beam plane illumination. *Nature Methods*, 8(5):417–423, May 2011.

[34] Misha B. Ahrens, Michael B. Orger, Drew N. Robson, Jennifer M. Li, and Philipp J. Keller. Whole-brain functional imaging at cellular resolution using light-sheet microscopy. *Nature Methods*, 10(5):413–420, May 2013.

[35] Béatrice Berthet and Alexis Maizel. Light sheet microscopy and live imaging of plants. *Journal of Microscopy*, 263(2):158–164, August 2016.

[36] Michael Weber and Jan Huisken. Light sheet microscopy for real-time developmental biology. *Current Opinion in Genetics & Development*, 21(5):566–572, October 2011.

[37] Elisabete C. Costa, Daniel N. Silva, André F. Moreira, and Ilídio J. Correia. Optical clearing methods: An overview of the techniques used for the imaging of 3D spheroids. *Biotechnology and Bioengineering*, 116(10):2742–2763, October 2019.

[38] E. Ploetz, S. Laimgruber, S. Berner, W. Zinth, and P. Gilch. Femtosecond stimulated Raman microscopy. *Applied Physics B*, 87(3):389–393, May 2007.

[39] Christian W. Freudiger, Wei Min, Brian G. Saar, Sijia Lu, Gary R. Holtom, Chengwei He, Jason C. Tsai, Jing X. Kang, and X. Sunney Xie. Label-Free Biomedical Imaging with High Sensitivity by Stimulated Raman Scattering Microscopy. *Science*, 322(5909):1857–1861, December 2008.

[40] P. Nandakumar, A. Kovalev, and A. Volkmer. Vibrational imaging based on stimulated Raman scattering microscopy. *New Journal of Physics*, 11(3):033026, March 2009.

[41] Yasuyuki Ozeki, Fumihiro Dake, Shin'ichiro Kajiyama, Kiichi Fukui, and Kazuyoshi Itoh. Analysis and experimental assessment of the sensitivity of stimulated Raman scattering microscopy. *Optics Express*, 17(5):3651–3658, March 2009.

[42] Miriam J. B. Moester, Liron Zada, Bart Fokker, Freek Ariese, and Johannes F. de Boer. Stimulated Raman scattering microscopy with long wavelengths for improved imaging depth. *Journal of Raman Spectroscopy*, 50(9):1321–1328, 2019.

[43] Brian G. Saar, Christian W. Freudiger, Jay Reichman, C. Michael Stanley, Gary R. Holtom, and X. Sunney Xie. Video-Rate Molecular Imaging in Vivo with Stimulated Raman Scattering. *Science*, 330(6009):1368–1370, December 2010.

[44] D. Huang, E. A. Swanson, C. P. Lin, J. S. Schuman, W. G. Stinson, W. Chang, M. R. Hee, T. Flotte, K. Gregory, C. A. Puliafito, and Al Et. Optical coherence tomography. *Science*, 254(5035):1178–1181, November 1991.

[45] A. F. Fercher, W. Drexler, C. K. Hitzenberger, and T. Lasser. Optical coherence tomography - principles and applications. *Reports on Progress in Physics*, 66(2):239–303, January 2003.

[46] Adolf Friedrich Fercher. Optical coherence tomography. *Journal of Biomedical Optics*, 1(2):157–173, April 1996.

[47] S. R. Chinn, E. A. Swanson, and J. G. Fujimoto. Optical coherence tomography using a frequency-tunable optical source. *Optics Letters*, 22(5):340–342, March 1997.

[48] Arnaud Dubois, Kate Grieve, Gael Moneron, Romain Lecaque, Laurent Vabre, and Claude Boccara. Ultrahigh-resolution full-field optical coherence tomography. *Applied Optics*, 43(14):2874–2883, May 2004.

[49] S. H. Yun, G. J. Tearney, B. E. Bouma, B. H. Park, and J. F. de Boer. High-speed spectral-domain optical coherence tomography at 1.3 Mm wavelength. *Optics Express*, 11(26):3598–3604, December 2003.

[50] A. F. Fercher, C. K. Hitzenberger, G. Kamp, and S. Y. El-Zaiat. Measurement of intraocular distances by backscattering spectral interferometry. *Optics Communications*, 117(1):43–48, May 1995.

[51] Maciej Wojtkowski, Rainer Leitgeb, Andrzej Kowalczyk, Tomasz Bajraszewski, and Adolf Friedrich Fercher. In vivo human retinal imaging by Fourier domain optical coherence tomography. *Journal of Biomedical Optics*, 7(3):457–463, July 2002.

[52] N. A. Nassif, B. Cense, B. H. Park, M. C. Pierce, S. H. Yun, B. E. Bouma, G. J. Tearney, T. C. Chen, and J. F. de Boer. In vivo high-resolution video-rate spectral-domain optical coherence tomography of the human retina and optic nerve. *Optics Express*, 12(3):367–376, February 2004.

[53] Michael A. Choma, Marinko V. Sarunic, Changhuei Yang, and Joseph A. Izatt. Sensitivity advantage of swept source and Fourier domain optical coherence tomography. *Optics Express*, 11(18):2183–2189, September 2003.

[54] Michalina Gora, Karol Karnowski, Maciej Szkulmowski, Bartlomiej J. Kaluzny, Robert Huber, Andrzej Kowalczyk, and Maciej Wojtkowski. Ultra high-speed swept source OCT imaging of the anterior segment of human eye at 200 kHz with adjustable imaging range. *Optics Express*, 17(17):14880–14894, August 2009.

[55] J.M. Schmitt. Optical coherence tomography (OCT): A review. *IEEE Journal of Selected Topics in Quantum Electronics*, 5(4):1205–1215, July 1999.

[56] R. Leitgeb, C. K. Hitzenberger, and A. F. Fercher. Performance of fourier domain vs. time domain optical coherence tomography. *Optics Express*, 11(8):889–894, April 2003.

[57] Johannes F. de Boer, Barry Cense, B. Hyle Park, Mark C. Pierce, Guillermo J. Tearney, and Brett E. Bouma. Improved signal-to-noise ratio in spectral-domain compared with time-domain optical coherence tomography. *Optics Letters*, 28(21):2067–2069, November 2003.

[58] H. J. Böhringer, D. Boller, J. Leppert, U. Knopp, E. Lankenau, E. Reusche, G. Hüttmann, and A. Giese. Time-domain and spectral-domain optical coherence tomography in the analysis of brain tumor tissue. *Lasers in Surgery and Medicine*, 38(6):588–597, 2006.

[59] Osnath Assayag, Martine Antoine, Brigitte Sigal-Zafrani, Michael Riben, Fabrice Harms, Adriano Burcheri, Kate Grieve, Eugénie Dalimier, Bertrand Le Conte de Poly, and Claude Boccara. Large Field, High Resolution Full-Field Optical Coherence Tomography: A Pre-Clinical Study of Human Breast Tissue and Cancer Assessment. *Technology in Cancer Research & Treatment*, 13(5):455–468, October 2014.

[60] Chao Zhou, David W. Cohen, Yihong Wang, Hsiang-Chieh Lee, Amy E. Mondelblatt, Tsung-Han Tsai, Aaron D. Aguirre, James G. Fujimoto, and James L. Connolly. Integrated Optical Coherence Tomography and Microscopy for Ex Vivo Multiscale Evaluation of Human Breast Tissues. *Cancer Research*, 70(24):10071–10079, December 2010.

[61] Kostadinka K. Bizheva, Angelika Unterhuber, Boris M. Hermann, Boris Považay, Harald Sattmann, Wolfgang Drexler, Andreas Stingl, Tuan M. Le, Michael Mei, Ronald Holzwarth, Herbert Reitsammer, John E. Morgan, and Alan Cowey. Imaging ex vivo and in vitro brain morphology in animal models with ultrahigh resolution optical coherence tomography. *Journal of Biomedical Optics*, 9(4):719–724, July 2004.

[62] Freddy T. Nguyen, Adam M. Zysk, Eric J. Chaney, Jan G. Kotynek, Uretz J. Oliphant, Frank J. Bellafiore, Kendrith M. Rowland, Patricia A. Johnson, and Stephen A. Boppart. Intraoperative Evaluation of Breast Tumor Margins with Optical Coherence Tomography. *Cancer Research*, 69(22):8790–8796, November 2009.

[63] Jeffrey L. Fine, Larry Kagemann, Gadi Wollstein, Hiroshi Ishikawa, and Joel S. Schuman. Direct scanning of pathology specimens using spectral domain optical coherence tomography: A pilot study. *Ophthalmic Surgery, Lasers & Imaging: The Official Journal of the International Society for Imaging in the Eye*, 41 Suppl:S58–64, 2010 Nov-Dec.

[64] Woonggyu Jung and Stephen A. Boppart. Optical coherence tomography for rapid tissue screening and directed histological sectioning. *Analytical Cellular Pathology (Amsterdam)*, 35(3):129, 2012.

[65] Lida P. Hariri, Mari Mino-Kenudson, Michael Lanuti, Alyssa J. Miller, Eugene J. Mark, and Melissa J. Suter. Diagnosing Lung Carcinomas with Optical Coherence Tomography. *Annals of the American Thoracic Society*, 12(2):193–201, January 2015.

[66] Ryan M. Nolan, Steven G. Adie, Marina Marjanovic, Eric J. Chaney, Fredrick A. South, Guillermo L. Monroy, Nathan D. Shemonski, Sarah J. Erickson-Bhatt, Ryan L. Shelton, Andrew J. Bower, Douglas G. Simpson, Kimberly A. Cradock, Z. George Liu, Partha S. Ray, and Stephen A. Boppart. Intraoperative optical coherence tomography for assessing human lymph nodes for metastatic cancer. *BMC Cancer*, 16(1):144, February 2016.

[67] Ying Fan, Andreas Mandelis, Gloria Spirou, and I. Alex Vitkin. Development of a laser photothermoacoustic frequency-swept system for subsurface imaging: Theory and experiment. *The Journal of the Acoustical Society of America*, 116(6):3523–3533, December 2004.

[68] Konstantin Maslov, Hao F. Zhang, Song Hu, and Lihong V. Wang. Optical-resolution photoacoustic microscopy for *in vivo* imaging of single capillaries. *Optics Letters*, 33(9):929–931, May 2008.

[69] Song Hu, Konstantin Maslov, and Lihong V. Wang. Second-generation optical-resolution photoacoustic microscopy with improved sensitivity and speed. *Optics Letters*, 36(7):1134–1136, April 2011.

[70] Paul Beard. Biomedical photoacoustic imaging. *Interface Focus*, 1(4):602–631, August 2011.

[71] Alexander Graham Bell. On the Production and Reproduction of Sound by Light. *American Association for the Advancement of Science*, August 1880.

[72] Allan Rosencwaig. Thermal-Wave Imaging. *Science*, 218(4569):223–228, October 1982.

[73] Irio G. Calasso, Walter Craig, and Gerald J. Diebold. Photoacoustic Point Source. *Physical Review Letters*, 86(16):3550–3553, April 2001.

[74] V.G. Andreev, A.A. Karabutov, and A.A. Oraevsky. Detection of ultrawide-band ultrasound pulses in optoacoustic tomography. *IEEE Transactions on Ultrasonics, Ferroelectrics, and Frequency Control*, 50(10):1383–1390, October 2003.

[75] Junjie Yao and Lihong V. Wang. Photoacoustic microscopy. *Laser & Photonics Reviews*, 7(5):758–778, 2013.

[76] Chi Zhang, Konstantin Maslov, and Lihong V. Wang. Subwavelength-resolution label-free photoacoustic microscopy of optical absorption *in vivo*. *Optics Letters*, 35(19):3195–3197, October 2010.

[77] Junjie Yao, Konstantin I. Maslov, Yu Zhang, Younan Xia, and Lihong V. Wang. Label-free oxygen-metabolic photoacoustic microscopy in vivo. *Journal of Biomedical Optics*, 16(7):076003, July 2011.

[78] Hao F. Zhang, Konstantin Maslov, George Stoica, and Lihong V. Wang. Functional photoacoustic microscopy for high-resolution and noninvasive in vivo imaging. *Nature Biotechnology*, 24(7):848–851, July 2006.

[79] Jacob Staley, Patrick Grogan, Abbas K. Samadi, Huizhong Cui, Mark S. Cohen, and Xinmai Yang. Growth of melanoma brain tumors monitored by photoacoustic microscopy. *Journal of Biomedical Optics*, 15(4):040510, July 2010.

[80] Han-Wei Wang, Ning Chai, Pu Wang, Song Hu, Wei Dou, David Umulis, Lihong V. Wang, Michael Sturek, Robert Lucht, and Ji-Xin Cheng. Label-Free Bond-Selective Imaging by Listening to Vibrationally Excited Molecules. *Physical Review Letters*, 106(23):238106, June 2011.

[81] Vladislav V. Yakovlev, Hao F. Zhang, Gary D. Noojin, Michael L. Denton, Robert J. Thomas, and Marlan O. Scully. Stimulated Raman photoacoustic imaging. *Proceedings of the National Academy of Sciences*, 107(47):20335–20339, November 2010.

[82] Hugh A. MacKenzie, Helen S. Ashton, Stephen Spiers, Yaochun Shen, Scott S. Freeborn, John Hannigan, John Lindberg, and Peter Rae. Advances in Photoacoustic Noninvasive Glucose Testing. *Clinical Chemistry*, 45(9):1587–1595, September 1999.

[83] Armin Hochreiner, Johannes Bauer-Marschallinger, Peter Burgholzer, Bernhard Jakoby, and Thomas Berer. Non-contact photoacoustic imaging using a fiber based interferometer with optical amplification. *Biomedical Optics Express*, 4(11):2322–2331, November 2013.

[84] Guy Rousseau, Alain Blouin, and Jean-Pierre Monchalin. Non-contact photoacoustic tomography and ultrasonography for tissue imaging. *Biomedical Optics Express*, 3(1):16–25, January 2012.

[85] Guy Rousseau, Bruno Gauthier, Alain Blouin, and Jean-Pierre Monchalin. Non-contact biomedical photoacoustic and ultrasound imaging. *Journal of Biomedical Optics*, 17(6):061217, May 2012.

[86] Yi Wang, Chunhui Li, and Ruikang K. Wang. Noncontact photoacoustic imaging achieved by using a low-coherence interferometer as the acoustic detector. *Optics Letters*, 36(20):3975–3977, October 2011.

[87] Thomas Berer, Armin Hochreiner, Saeid Zamiri, and Peter Burgholzer. Remote photoacoustic imaging on solid material using a two-wave mixing interferometer. *Optics Letters*, 35(24):4151–4153, December 2010.

[88] Robert Nuster, Paul Slezak, and Guenther Paltauf. High resolution three-dimensional photoacoustic tomography with CCD-camera based ultrasound detection. *Biomedical Optics Express*, 5(8):2635–2647, August 2014.

[89] Susan H. Jack, David B. Hann, and Clive A. Greated. Influence of the acousto-optic effect on laser Doppler anemometry signals. *Review of Scientific Instruments*, 69(12):4074–4081, December 1998.

[90] Kevan L. Bell, Parsin Haji Reza, and Roger J. Zemp. Real-time functional photoacoustic remote sensing microscopy. *Optics Letters*, 44(14):3466–3469, July 2019.

[91] Peter Neil Temple Wells. *Biomedical Ultrasonics*. Academic Pr, 1977.

[92] Matthew T. Martell, Cory Rewcastle, and Roger J. Zemp. Combined spectral-domain optical coherence tomography and photoacoustic remote sensing microscopy* (Conference Presentation). In *Photons Plus Ultrasound: Imaging and Sensing 2020*, volume 11240, page 112401V. International Society for Optics and Photonics, March 2020.

[93] Julio A. Ibarra. The Value of Combined Large Format Histopathology Technique to Assess the Surgically Removed Breast Tissue following Neoadjuvant Chemotherapy: A Single Institution Study of 40 Cases. *International Journal of Breast Cancer*, 2012, 2012.

[94] Philip Bryant, Neil Haine, Jeremy Johnston, and Peter Ntiamoah. Application of large format tissue processing in the histology laboratory. *Journal of Histotechnology*, 42(3):150–162, July 2019.

[95] Benjamin W. Maloney, David M. McClatchy Iii, Brian W. Pogue, Keith D. Paulsen, Wendy A. Wells M.d, and Richard J. Barth M.d. Review of methods for intraoperative margin detection for breast conserving surgery. *Journal of Biomedical Optics*, 23(10):100901, October 2018.

[96] S. K. Chow, H. Hakozaki, D. L. Price, N. a. B. Maclean, T. J. Deerinck, J. C. Bouwer, M. E. Martone, S. T. Peltier, and M. H. Ellisman. Automated microscopy system for mosaic acquisition and processing. *Journal of Microscopy*, 222(2):76–84, 2006.

[97] Eric Chandler, Erich Hoover, Jeff Field, Kraig Sheetz, Wafa Amir, Ramon Carriles, Shi-you Ding, and Jeff Squier. High-resolution mosaic imaging with multifocal, multiphoton photon-counting microscopy. *Applied Optics*, 48(11):2067–2077, April 2009.

[98] Peng Shao, Wei Shi, Ryan K. Chee, and Roger J. Zemp. Mosaic acquisition and processing for optical-resolution photoacoustic microscopy. *Journal of Biomedical Optics*, 17(8):080503, July 2012.

[99] Jin Woo Baik, Jin Young Kim, Seonghee Cho, Seongwook Choi, Jongbeom Kim, and Chulhong Kim. Super Wide-Field Photoacoustic Microscopy of Animals and Humans In Vivo. *IEEE Transactions on Medical Imaging*, 39(4):975–984, April 2020.

[100] Saad Abbasi, Martin Le, Bazil Sonier, Kevan Bell, Deepak Dinakaran, Gilbert Bigras, John R. Mackey, and Parsin Haji Reza. Chromophore selective multi-wavelength photoacoustic remote sensing of unstained human tissues. *Biomedical Optics Express*, 10(11):5461–5469, November 2019.

[101] Huabei Jiang. *Photoacoustic Tomography*. CRC Press, December 2014.

[102] Joon-Mo Yang, Konstantin Maslov, Hao-Chung Yang, Qifa Zhou, and Lihong V. Wang. Endoscopic photoacoustic microscopy. In *Proc.SPIE*, volume 7177, February 2009.

[103] Michel G. Arsenault, Michael C. Kolios, and William M. Whelan. Optoacoustic detection of thermal lesions. In *Proc.SPIE*, volume 7177, February 2009.

[104] George J. Tserevelakis, Dominik Soliman, Murad Omar, and Vasilis Ntziachristos. Hybrid multiphoton and optoacoustic microscope. *Optics Letters*, 39(7):1819–1822, April 2014.

[105] Siyang Zuo, Michael Hughes, and Guang-Zhong Yang. Novel Balloon Surface Scanning Device for Intraoperative Breast Endomicroscopy. *Annals of Biomedical Engineering*, 44(7):2313–2326, July 2016.

[106] Brendon S. Restall, Nathaniel J. M. Haven, Pradyumna Kedarisetti, and Roger J. Zemp. Multispectral photoacoustic remote sensing microscopy using 532nm and 266nm excitation wavelengths. In *Proc.SPIE*, volume 11240, February 2020.

[107] Isaac Amidror. Scattered data interpolation methods for electronic imaging systems: A survey. *Journal of Electronic Imaging*, 11(2):157, April 2002.

[108] Mark de Berg, Marc van Kreveld, Mark Overmars, and Otfried Schwarzkopf. Computational Geometry. In Mark de Berg, Marc van Kreveld, Mark Overmars, and Otfried Schwarzkopf, editors, *Computational Geometry: Algorithms and Applications*, pages 1–17. Springer, Berlin, Heidelberg, 1997.

[109] H. Weimer and J. Warren. Fast approximating triangulation of large scattered datasets. *Advances in Engineering Software*, 30(6):389–400, June 1999.

[110] Stephan Preibisch, Stephan Saalfeld, and Pavel Tomancak. Globally optimal stitching of tiled 3D microscopic image acquisitions. *Bioinformatics*, 25(11):1463–1465, June 2009.

[111] Konstantin Maslov, Hao F. Zhang, Song Hu, and Lihong V. Wang. Optical-resolution photoacoustic microscopy for *in vivo* imaging of single capillaries. *Optics Letters*, 33(9):929–931, May 2008.

[112] Zhixing Xie, Shuliang Jiao, Hao F. Zhang, and Carmen A. Puliafito. Laser-scanning optical-resolution photoacoustic microscopy. *Optics Letters*, 34(12):1771–1773, June 2009.

[113] Bin Rao, Li Li, Konstantin Maslov, and Lihong Wang. Hybrid-scanning optical-resolution photoacoustic microscopy for in vivo vasculature imaging. *Optics Letters*, 35(10):1521–1523, May 2010.

[114] Junjie Yao, Lidai Wang, Joon-Mo Yang, Liang S. Gao, Konstantin I. Maslov, Lihong V. Wang, Chih-Hsien Huang, and Jun Zou. Wide-field fast-scanning photoacoustic microscopy based on a water-immersible MEMS scanning mirror. *Journal of Biomedical Optics*, 17(8):080505, August 2012.

[115] Liang Song, Konstantin Maslov, and Lihong V. Wang. Section-illumination photoacoustic microscopy for dynamic 3D imaging of microcirculation *in vivo*. *Optics Letters*, 35(9):1482–1484, May 2010.

[116] Liang Song, Konstantin Maslov, and Lihong V. Wang. Multi-focal optical-resolution photoacoustic microscopy in vivo. *Optics letters*, 36(7):1236–1238, April 2011.

[117] Jin Young Kim, Changho Lee, Kyungjin Park, Geunbae Lim, and Chulhong Kim. Fast optical-resolution photoacoustic microscopy using a 2-axis water-proofing MEMS scanner. *Scientific Reports*, 5(1):7932, January 2015.

[118] Bangxin Lan, Wei Liu, Ya-chao Wang, Junhui Shi, Yang Li, Song Xu, Huaxin Sheng, Qifa Zhou, Jun Zou, Ulrike Hoffmann, Wei Yang, and Junjie Yao. High-speed wide-field photoacoustic microscopy of small-animal hemodynamics. *Biomedical Optics Express*, 9(10):4689–4701, September 2018.

[119] P. Kner, J. W. Sedat, D. A. Agard, and Z. Kam. High-resolution wide-field microscopy with adaptive optics for spherical aberration correction and motionless focusing. *Journal of Microscopy*, 237(2):136–147, 2010.

[120] Nadine Barrie Smith and Andrew Webb. *Introduction to Medical Imaging: Physics, Engineering and Clinical Applications*. Cambridge University Press, November 2010.

[121] J. A. Gomes. *Signal Averaged Electrocardiography: Concepts, Methods and Applications*. Springer Science & Business Media, December 2012.

[122] Loic A. Royer, Martin Weigert, Ulrik Günther, Nicola Maghelli, Florian Jug, Ivo F. Sbalzarini, and Eugene W. Myers. ClearVolume: Open-source live 3D visualization for light-sheet microscopy. *Nature Methods*, 12(6):480–481, June 2015.

[123] Kurt Rossmann. Point Spread-Function, Line Spread-Function, and Modulation Transfer Function. *Radiology*, August 1969.

[124] Glenn D. Boreman. *Modulation Transfer Function in Optical and Electro-Optical Systems*. SPIE Press, 2001.

[125] Michael Harold Freeman. *Optics*. Elsevier Health Sciences, 1990.

[126] Steven Smith. *Digital Signal Processing: A Practical Guide for Engineers and Scientists*. Elsevier, October 2013.

[127] F. S. Pavone, P. T. C. So, and P. M. W. French. *Microscopy Applied to Biophotonics*. IOS Press, July 2014.

[128] Laser Institute of America . ANSI Z136.1-2007 American National Standard for Safe Use of Lasers. *ANSI*, 2007.

[129] M. Frigo and S.G. Johnson. The Design and Implementation of FFTW3. *Proceedings of the IEEE*, 93(2):216–231, February 2005.

[130] Kevan L. Bell, Parsin Hajireza, and Roger J. Zemp. Coherence-gated photoacoustic remote sensing microscopy. *Optics Express*, 26(18):23689–23704, September 2018.

[131] Dimitris Papadias, Yufei Tao, Kyriakos Mouratidis, and Chun Kit Hui. Aggregate nearest neighbor queries in spatial databases. *ACM Transactions on Database Systems*, 30(2):529–576, June 2005.

[132] Vincent Garcia, Eric Debreuve, and Michel Barlaud. Fast k nearest neighbor search using GPU. In *2008 IEEE Computer Society Conference on Computer Vision and Pattern Recognition Workshops*, pages 1–6, June 2008.

[133] Jerome H. Friedman, Jon Louis Bentley, and Raphael Ari Finkel. An Algorithm for Finding Best Matches in Logarithmic Expected Time. *ACM Transactions on Mathematical Software*, 3(3):209–226, September 1977.

[134] Michael Sipser. *Introduction to the Theory of Computation*. Thomson Course Technology, 2006.

[135] Soheil Soltani, Ashkan Ojaghi, and Francisco E. Robles. Deep UV dispersion and absorption spectroscopy of biomolecules. *Biomedical Optics Express*, 10(2):487–499, February 2019.

[136] Takashi Buma, Nicole C. Conley, and Sang Won Choi. Multispectral photoacoustic microscopy of lipids using a pulsed supercontinuum laser. *Biomedical Optics Express*, 9(1):276–288, January 2018.

[137] Logan Snider, Kevan Bell, Parsin Hajireza, and Roger J. Zemp. Toward wide-field high-speed photoacoustic remote sensing microscopy. In *Photons Plus Ultrasound: Imaging and Sensing 2018*, volume 10494, page 1049423. International Society for Optics and Photonics, February 2018.

[138] J. McHowat, J. H. Jones, and M. H. Creer. Quantitation of individual phospholipid molecular species by UV absorption measurements. *Journal of Lipid Research*, 37(11):2450–2460, November 1996.

[139] Mirjam Schürmann, Jana Scholze, Paul Müller, Jochen Guck, and Chii J. Chan. Cell nuclei have lower refractive index and mass density than cytoplasm. *Journal of Biophotonics*, 9(10):1068–1076, 2016.

[140] Gilbert Smithson Adair and Muriel Elaine Robinson. The specific refraction increments of serum-albumin and serum-globulin. *Biochemical Journal*, 24(4):993–1011, January 1930.

[141] Janos Vörös. The Density and Refractive Index of Adsorbing Protein Layers. *Biophysical Journal*, 87(1):553–561, July 2004.

[142] D. J. Goldstein. *Understanding the Light Microscope: A Computer-Aided Introduction*. Academic Press, September 1999.

[143] Jeremy Sanderson. *Understanding Light Microscopy*. John Wiley & Sons, March 2019.

[144] Mary Louise Turgeon. *Clinical Hematology: Theory and Procedures*. Lippincott Williams & Wilkins, 2005.

[145] Bruce Alberts, Alexander Johnson, Julian Lewis, Martin Raff, Keith Roberts, and Peter Walter. *Molecular Biology of the Cell*. Garland Science, fourth edition, 2002.

[146] Rui Li, Mikhail N. Slipchenko, Pu Wang, and Ji-Xin Cheng. Compact high power barium nitrite crystal-based Raman laser at 1197 nm for photoacoustic imaging of fat. *Journal of Biomedical Optics*, 18(4):040502, March 2013.

[147] Jan Huisken, Jim Swoger, Filippo Del Bene, Joachim Wittbrodt, and Ernst H. K. Stelzer. Optical Sectioning Deep Inside Live Embryos by Selective Plane Illumination Microscopy. *Science*, 305(5686):1007–1009, August 2004.

[148] Freddy T. Nguyen, Adam M. Zysk, Eric J. Chaney, Steven G. Adie, Jan G. Kotynek, Uretz J. Oliphant, Frank J. Bellafiore, Kendrith M. Rowland, Patricia A. Johnson, and Stephen A. Boppart. Optical Coherence Tomography: The Intraoperative Assessment of Lymph Nodes in Breast Cancer. *IEEE Engineering in Medicine and Biology Magazine*, 29(2):63–70, March 2010.

[149] J. M. Schmitt, A. Knuttel, M. Yadlowsky, and M. A. Eckhaus. Optical-coherence tomography of a dense tissue: Statistics of attenuation and backscattering. *Physics in Medicine and Biology*, 39(10):1705–1720, October 1994.

[150] Mohesh Moothanchery, Renzhe Bi, Jin Young Kim, Seungwan Jeon, Chulhong Kim, and Malini Olivo. Optical resolution photoacoustic microscopy based on multimode fibers. *Biomedical Optics Express*, 9(3):1190–1197, February 2018.

[151] Terence T. W. Wong, Ruiying Zhang, Chi Zhang, Hsun-Chia Hsu, Konstantin I. Maslov, Lidai Wang, Junhui Shi, Ruimin Chen, K. Kirk Shung, Qifa Zhou, and Lihong V. Wang. Label-free automated three-dimensional imaging of whole organs by microtomy-assisted photoacoustic microscopy. *Nature Communications*, 8(1):1386, November 2017.

[152] Nathaniel J. M. Haven, Pradyumna Kedarisetti, Brendon S. Restall, and Roger J. Zemp. Reflective objective-based ultraviolet photoacoustic remote sensing virtual histopathology. *Optics Letters*, 45(2):535–538, January 2020.

[153] Saad Abbasi, Martin Le, Bazil Sonier, Deepak Dinakaran, Gilbert Bigras, Kevan Bell, John R. Mackey, and Parsin Haji Reza. All-optical Reflection-mode Microscopic Histology of Unstained Human Tissues. *Scientific Reports*, 9(1):13392, September 2019.